Development of 3D multicellular liver organoids derived from human induced pluripotent stem cells to model antiretroviral therapy induced liver injury.

Submitted by

Mr Setjie Welcome Maepa

MPXSET001

Thesis submitted to the University of Cape Town in fulfilment of the requirements for the degree of Doctor of Philosophy in Medical Biochemistry

Division of Chemical and Systems Biology

Department of Integrative Biomedical Sciences

Faculty of Health Sciences

University of Cape Town

Supervisor: Associate Professor Hlumani Ndlovu

2025

Declaration

I, Setjie Welcome Maepa, hereby declare that the work on which this dissertation/thesis is based is my original work (except where acknowledgements indicate otherwise) and that neither the whole work nor any part of it has been, is being, or is to be submitted for another degree in this or any other university. I empower the university to reproduce for the purpose of research either the whole or any portion of the contents in any manner whatsoever.

Signature: Signed by candidate

Date: …24/01/2025……

Table of Contents

List of Figures

List of tables

Acknowledgements

"For I know the plans I have for you; declares the Lord, plans to prosper you and not to harm you, plans to give you a hope and a future" – Jeremiah 29:11, thus "let us unswervingly to the hope we profess, for he who promised is fail" - Hebrews 10:23. Trust in the lord with all your heart, lean not on your own understanding, in all your ways acknowledge him, and he will direct your path"- Proverbs 3:5-6. "Do not be anxious about anything, but in everything, by prayer and petition, with thanksgiving, present your request to God" - Phillipians 4:6. I presented my request to the almighty God to give me understanding; clear the way for me to complete this course, and with trust and hard work, God has made it possible.

This thesis is the output of the effort of collaborative work of several people whom I am profusely indebted in them and so grateful. I wish to extend my deepest and humble gratitude to my supervisor Associate Professor Hlumani Ndlovu for giving me the opportunity to conduct my research project in his laboratory. A special thank you to you and Associate Professor Mohlopheni Jackson Marakalala for granting me an unwavering support, inputs and mentoring throughout the course of the study and for ensuring that this research project is completed. Your continued support, the words of encouragement in both merry and pessimistic moments meant a lot to me. I have absorbed so many attributes and skills under your wings. We have encountered a lot of uncertainties with this research project, but you stood firm by my side and showed leadership. Those were indeed defining moments, I will forever be genuinely grateful, and it's been an absolute pleasure working with you. Interestingly, in you I have gained a supervisor, colleague, brother I never had and a friend.

I am profusely grateful for the hard work of my colleagues and teammates, both former and current. Stephanie Ncube, thanks for being so supportive when I first joined the group and for being there to teach me tissue culture and western blotting. I learnt a lot from you, your work ethic and passion for science has inspired me. To Dr Janine Scholefield, thank you for gifting us with the iPSCs to kickstart the research project, you really saved me from adding another 2 years of not being proactively working on my PhD research project. Dr Robea Ballo and Ms Thuli Matakoza, thank you so much for having faith in me when I first began to work with iPSCs. Your unwavering guidance and support instilled hope and courage in me to work tirelessly and aim to succeed.

A special thanks to my family. My late sisters: Maepa Makoma Promise, Maepa Matheku Salphy (Jeniffer) and late grandmother: Maepa Matheku Phathina, you have all left us soon, I hope you are all proud of the man I've become, thank you all for the sacrifices you have made, none of this would have been possible without them. My mother and a heroine: Maepa Lekgala Enicca, thank you for always believing in me and always wishing and wanting the best for me and my brother and nieces. Your support and love carried me through, and you have never let me down. To my ride or die, the mother of my pride and joy: Ratau Hlakodi Kholo, my biggest cheerleader, you have always been so supportive towards my academic journey and, thank you for the long non-ending calls, messages, and WhatsApp chats, and video calls, speaking with humility, pouring words of encouragement, affirmation, wisdom, and peace.

Always lending me your ear, talking about school, life challenges, future goals and most importantly instilling each other's faith meant the world to me. Thank you for cheering me on my friend, lover, and a sister, when I was at my lowest, you kept me going. You are a special kind and lastly thank you for bearing me a beautiful, smart, and humble daughter; Trudy wa rena (smiling). To my brother; Maepa Mokaoke Lehlogonolo and my nieces; Maepa Boitumelo and Maepa Tebogo, your smiles and kind hearts made the journey much more bearable, thank you and to my nieces and my daughter, I hope this serves as a motivation and constant reminder that anything is possible. I love you all so much, and ke leboga go menagane bana beshu.

This PhD journey would not have been possible without the financial support that I got from NRF under NRF Grant-Holder scholarship, UCT Doctoral Research Scholarship, VC Research Doctor scholarship, NRF Postgraduate scholarship and Oppenheimer memorial trust (OMT) scholarship.

Dedication

This work is fully dedicated to my lovely daughter; Trudy Ngwanatheku Ratau, my late grandmother; Phathina Matheku Maepa and last sisters; Promise Makoma Maepa and Salphy (Jeniffer) Matheku Maepa.

List of publications

Maepa, S.W. and Ndlovu, H., 2020. Advances in generating liver cells from pluripotent stem cells as a tool for modeling liver diseases. *Stem Cells*, *38*(5), pp.606-612.

In addition to the work presented in this thesis, author has made significant contribution in following publications.

Hadebe, S., Savulescu, A.F., Khumalo, J., Jones, K., Mangali, S., Mthembu, N., Musaigwa, F., **Maepa, W**., Ndlovu, H., Ngomti, A. and Scibiorek, M., 2023. Immunoglobulin M regulates airway hyperresponsiveness independent of T helper 2 allergic inflammation. *bioRxiv*, pp.2023-08.

Maepa, S.W, Marakalala, M.J, and Ndlovu H., 2023. Generation of multicellular 3D liver organoids from induced pluripotent stem cells as a Tool for Modelling Liver Diseases. Bio Protoco. 2024 Aug 5;14(15):e5042. Doi:10.21769/BioProtoc.5042.

Conferences & presentation

Human Biology, Integrative Biomedical Sciences and Pathology (HIP) Research Day 2023.

Oral presentation: “Generation of multicellular 3D liver organoids from induced pluripotent stem cells as a tool for modelling liver diseases”.

International Congress of Immunological Sciences (IUIS) 2023

Poster presentation: “Generation of multicellular 3D liver organoids from induced pluripotent stem cells as a tool for modelling liver diseases”.

Awards

NRF Grant-Holder Scholar Scholarship.

UCT Doctoral Research Scholarship.

VC Research Scholarship.

NRF Postgraduate Scholarship.

Oppenheimer Memorial Trust Scholarship.

HIP Research Day 2023: First place oral presentations, PhD.

List of abbreviations

ADRs:	Adverse drug reactions
AFP:	Alpha fetoprotein
AIDS:	Acquired Immunodeficiency Syndrome
ALCAM:	Activated leucocytes adhesion molecule
ALF:	Acute liver failure
ALP:	Alkaline Phosphatase
ALT:	Alanine Transaminase
APAP:	Acetaminophen
ART:	Antiretroviral therapy
ARV:	Antiretroviral
A+TB:	Antiretroviral therapy + antituberculosis
BCA:	Bicinchoninic assay
BSA:	Bovine serum albumin
BEC:	Biliary epithelial cells
BMP4:	Bone morphogenetic protein 4
BP:	Biological Process
BSEP:	Bile salt export transport
CC:	Cellular component
cDNA:	Complementary deoxynucleic acid
CFTR:	Cystic fibrosis transmembrane conductance regulator
CLEC-4F:	C-type lectin family member 4
CLS:	Cholangiocytes like cells
CYP3A4:	Cytochrome P450 3A4
CXCR4:	Chemokine X receptor 4

DAVID:	Database for annotation, visualization and integrated discovery
DPBS:	Dulbecco’s phosphate buffered saline
DE:	Definitive endoderm
DILI:	Drug induced liver injury
DMEs:	Drug metabolizing enzymes
DMEM:	Dulbecco modified eagle medium
DMSO:	Dimethyl sulphate
ECM:	Extracellular matrix
ELISA:	Enzyme immunosorbent assay
EDTA:	Ethylenediaminetetraacetic acid
EFV:	Efavirenz
EpCAM:	Epithelial cell adhesion molecule
FACS:	Fluorescence activated cell sorting
FC□R2B:	Fc-gamma receptor 2B
FDR:	False-discovery rate
FGF2:	Fibroblast growth factor 2
FGF-4:	Fibroblast growth factor 4
FGS:	Foregut spheroid
GAPDH:	Glyceraldehyde 3-phosphate dehydrogenase
GO:	Gene ontology
GWAS:	Genome wide association studies
HAART:	Highly active antiretroviral therapy
HBV:	Hepatitis B virus

HCM:	Hepatocyte culture medium
HCV:	Hepatitis C virus
HGF:	Hepatocyte growth factor
HLO:	Human liver organoids
HLA:	Human leukocyte antigen
HLCs:	Hepatocyte-like cells
HUVECs:	Human umbilical cord vein endothelial cells
HSC:	Hepatic stellate cells
iPSCs:	Induced pluripotent stem cells
KCs:	Kupffer cells
KEGG:	Kyoto Encyclopaedia of Genes and Genomes
KSR:	Knockout serum replacer
LC-MS:	Liquid chromatography mass spectrometry
LDH:	Lactate dehydrogenase
LDL:	Low density lipoprotein
LFQ:	Label free quantification
LSECs:	Liver sinusoid endothelial cells
MF:	Molecular function
NAFLD:	Non-alcoholic fatty liver diseases
NASH:	Non-alcoholic steatohepatitis
NPCs:	Non-parenchymal cells
OSM:	Oncostatin M
PBS:	Phosphate buffered saline
PCA:	Principal component analysis

PGECs:	Posterior gut endothelial cells
PHHs:	Parenchymal human hepatocytes
PPI:	Protein-protein interactions
PSC:	Pluripotent stem cells
RA:	Retinoic acid
SDS-PAGE:	Sodium dodecyl sulphate – polyacrylamide gel electrophoresis
SEA:	*Schistosome* egg antigen
SSA:	Sub-Saharan Africa
STR:	Secretin receptor
TEN:	Toxic epidermal necrosis
TNFα:	Tumour necrosis factor alpha
ULN:	Upper limit of the normal
VEGF:	Vascular endothelial growth factor
VTN:	Vitronectin
WHO:	World Health Organization

Abstract

Introduction: The liver is an essential organ in the body that perform key functions in the synthesis of serum proteins, biotransformation, and detoxification of xenobiotic drugs. Liver diseases and drug cytotoxicity studies have been conducted using cancer-derived cell lines which are inferior. Hence, in the present study, we aimed to develop a robust and tractable 3D multicellular human liver organoid model suitable for studying liver diseases.

Methods: We first developed a reproducible method to generate human liver organoids (HLOs) from induced pluripotent stem cells (iPSCs). We performed quantitative reverse transcriptase-polymerase chain reaction (RT-qPCR) to confirm stage specific gene markers and validated the presence of multiple cell lineages using flow cytometry. We assessed the functionality of organoids by stimulating HLOs with anti-retroviral therapy (ART) or a combination of ART and antituberculosis drugs (A+TB) or *Schistosoma mansoni soluble egg antigen* (SEA) or Troglitazone (TGZ). We performed enzyme-linked immunosorbent assay (ELISA) to quantitatively determine pro-inflammatory and anti-inflammatory cytokines levels in ART/SEA/TGZ treated HLOs. A mass spectrometry-based proteomics approach was applied to decipher protein dynamics and molecular mechanisms of drug-induced liver injury in treated HLOs.

Results: HLO exhibited robust mature hepatic gene markers (*CYP3A4*, *ATA1, ALB* and *HNF4-α*), reduction in pluripotency (*OCT-4, Nanog, and Sox2*) and the definitive endoderm (*SOX17* and *GSC*) markers. Flow cytometry using EpCAM, CD166 and CD68 antibodies indicated that HLOs comprised of 60,4% EpCAM+ cells*,* 11,2% EpCAM-/CD166+ cells and 5% EpCAM-/CD68+ cells, respectively. HLOs exhibited high *CYP3A4* enzyme activity compared to HepaRG 3D model. Proinflammatory (*IL6, IL-1β and TNF-α*) and anti-inflammatory (*IL-4* and *IL-10*) cytokines were elevated in both models. *IL-4* was more pronounced in *SEA*-treated HLOs only. Discovery mass spectrometry quantified number of proteins in ART-treated HLOs, A+TB-treated HLOs and TGZ-treated HLOs compared to untreated HLOs. Our quantitative proteomic analysis identified 65 significantly differentially expressed proteins (DEPs) in ARTHLOs (11 upregulated and 54 downregulated), 19 DEPs in A+TB-HLOs (8 upregulated and 11 downregulated) and 52 DEPs in TGZ-HLO (11 upregulated and

41 downregulated). Functional enrichment of these DEPs in ART-HLO, A+TB-HLO and TGZ groups based on Gene ontology (GO), and KEGG pathway revealed proteins that were associated with immunity and inflammation, oxidative stress, cell proliferation, protein synthesis, neutrophil extracellular traps (NETs) formation, ATP dependent chromatin remodelling and necroptosis. We found that MGST1 protein was commonly upregulated protein among ART, A+TB and TGZ groups. Some of these DEPs have been correlated with drug induced liver injury, while others may represent novel proteins involved in drug induced liver injury.

Conclusion: We successfully generated multicellular 3D liver organoids consisting of hepatocytes, Kupffer cells and hepatic stellate cells. Proteomic data revealed that ART, A+TB and TGZ alters the expression of proteins mostly involved immunity and inflammation and mitochondrial functions, augmented oxidative stress, and necroptosis.

Chapter 1: Introduction and literature review

1.1 General background

The liver is a vital organ that is involved in metabolism, synthesis of serum proteins and detoxification of xenobiotic compounds and alcohol [1]. These vital functions can be impaired by drug induced liver injury (DILI), hepatitis B and C virus (HBV and HCV), non-alcoholic fatty liver diseases (NAFLD) and hepatocellular carcinoma (HCC) [2]. The large burden of liver diseases along with the management difficulties encountered have provided the impetus to pursue use of representative *in vitro* models with capacity to recapitulate liver functions [3]. Earlier liver models relied heavily on cancer-derived cell lines which have been proven to be inferior due to the suboptimal activity of drug metabolizing enzymes [4,5]. Isolated primary human hepatocytes (PHH) are considered the "gold standard" for drug metabolism and toxicity screening [6,7]. However, these cells display a rapid decline in the phenotypic function when cultured in traditional two-dimensional (2D) monolayer cultures and there is also a scarcity of donors [7].

To overcome these limitations of using primary human hepatocytes (PHH), researchers have developed various approaches including genetic modification of the cells, three-dimensional (3D) cultures combined with tissue engineering and media compositions [1,8,9]. Additionally, advances in the cell culture systems offer a great opportunity to generate patient specific hepatocytes using 2D cell-based [4] and the 3D organoid platforms [1,10]. Pluripotent stem cells (PSCs), particularly induced PSCs (iPSCs) have emerged as an alternative source for liver cells which can be obtained by direct differentiation of iPSCs into hepatic cells [9,10]. The 3D cultured cells display better physiologic and metabolic features of the native liver tissue in comparison to 2D cell-based cultures [1,11]. However, vast majority of the reported methods predominantly differentiate cells into hepatic epithelial lineage only; thus, lacking essential supportive cellular lineages such as profibrotic hepatic stellate cells (HSCs) and inflammatory cells (Kupffer cells; KCs). Hence, they lack the capacity to model inflammatory diseases [1,12].

Others developed co-culture cell models based on mixing both the epithelial cells and supportive lineages from iPSCs [13,14]. However, these methods suffer the artefactual inflammation and fibrosis resulting from difficulty in choosing optimum cell culture

medium and extracellular matrix (ECM), in which multiple cell lineages can be co-maintained [15,16]. Hence, establishment of a relevant and physiologically robust hepatic *in vitro* culture models comprised of parenchymal and supportive (stromal) cell lineages will be the most invaluable platforms to facilitate modelling of complex metabolic and inflammatory liver diseases and drug screening.

1.2 Preclinical hepatic models for assessment of drug induced liver injury

There are plenty of models that can be used for toxicity and preclinical screening of drug-induced liver injury (DILI). However, selection of a certain model is dependent on its abilities to detect specific mechanism of liver toxicity associated with DILI over the other models [17]. Therefore, prior to conducting an *in vitro* assay, limitations of the model need to be evaluated to ensure that a preclinical question can be answered based on the physiology of the model. For instance, earlier toxicity and drug screening studies relied on using animal models. However, several studies revealed that many animal models do not faithfully recapitulate the physiological functions of the human liver due to interspecies variability [18]. Animals may show increased sensitivity towards toxicity of a drug at doses considered normal in humans [19]. In parallel, a retrospective data analysis showed that concordance rates were poor between the animals and humans, with a true positive human toxicity concordance rate of 63% and 43% for the rodents and non-rodent models [20]. Consequently, these limit the use of the animal models to predict drug toxicity and metabolism. In 2007, the U.S National Academy of Science released a consensus report regarding toxicity testing. The report urged a paradigm shift from extensive usage of the current testing system, which is primarily based on animal models to utilization of *in vitro* systems employing human primary cells or immortalized cell lines to obtain increased efficacy and better mechanistic understanding of human adverse drug reactions (ADRs) upon xenobiotic exposure [21].

1.2.1 Primary human hepatocytes

Primary human hepatocytes (PHH) isolated from human tissue biopsies are considered the “gold standard” for evaluating hepatic metabolism and toxicology testing [7]. Functional PHH show phase I and phase II metabolic cytochrome P450 (CYP) enzyme activities, albumin (ALB) production and urea formation, glucose

metabolism and glycogen storage as well as other vital liver functions when cultured appropriately [22]. Studies have shown that cultivation of PHH in 3D system provided by ECM results in continuous differentiation of the cells and gene expression patterns of drug metabolizing enzymes (DMEs) are well maintained similarly to those observed in the native organ [22,23]. When cultivated in 2D, PHH cells barely survive due to rapid dedifferentiation and sudden loss of cell polarity [8,24]. In contrast, plating on rigid substratum induces abnormal cell morphology and functional alterations [6]. Cells flatten, lack of cell-cell contact, and loss of polarity hampers the formation of biliary canicular networks, thus leading to reduced expression of DMEs and decline in metabolic activities [6,7]. Finally, the scarcity of liver donors limits the availability of PHH for routine laboratory studies.

To address the limitations of PHH for use in *in vitro* cultures, researchers have sought for an alternative source of liver cells, and they opted for immortalized or cancer-derived liver cell lines such as HepG2 or HepaRG cells.

1.2.2 Immortalized cancer-derived cell lines

1.2.2.1 HepG2 cells

HepG2 cells are the widely used hepatic cell lines for toxicology studies due to their stable phenotype, ease of handling, availability and high proliferative capacity [24]. HepG2 cells are tumorigenic in nature and analysis of supernatant fluid revealed that a high number of characteristic proteins of PHH were conserved in the HepG2 cells [5,24]. These conserved liver proteins were albumin, hepatocytes nuclear factor and conjugating enzymes [5]. However, HepG2 cells exhibit relatively very low expression of certain DMEs and drug transporters compared to PHHs [25]. Consequently, their relevance for predicting DILI has been questioned.

1.2.2.2 HepaRG cells

The hepatoma derived HepaRG cells were first obtained from a differentiated liver tumour of a female hepatocarcinomatous patient who was suffering from chronic hepatitis C [26]. These cells were lauded as promising alternative for predicting DILI due to their ability to express functional hepatocytes markers such as cytochrome P450 enzymes and drug transporters [27,28]. HepaRG cells are unique in that they are immortalised, bipotent, and progenitor cells that can differentiate into hepatocytes

and primitive biliary-like cells [28]. A study by Yokoyama and colleagues tested the feasibility of using HepaRG cells as a model for testing toxicity of selected hepatotoxic compounds [5]. Differentiated HepaRG cells exhibited similar enzyme activities as PHH and they relatively expressed higher enzyme activities compared to HepG2 cells [5]. Nonetheless, both HepaRG and HepG2 cell lines represent single clones and lacks genetic variability. Overall, these potentially limit the utility of these 2D models as a robust and tractable tool for drug screening and toxicology testing. Also, these findings highlight the need for a reputable alternative and sustainable source for liver cells that could recapitulate functions of the native organ.

1.2.3 Alternative cell sources

Researchers invested considerable resources to develop protocols to generate *in vitro* liver models that would faithfully recapitulate at least some of the functions of the native organ. All these commitments are aimed to study liver development, metabolism, and to evaluate hepatotoxicity of xenobiotic drugs and model liver diseases. Induced pluripotent stem cells (iPSCs) are a promising alternative source for the generation of liver cells because of their unlimited proliferation and differentiation capacity [13]. These cells have the potential to differentiate into parenchymal and non-parenchymal (NPC) liver cells [13,29]. iPSCs can be easily derived from human skin fibroblasts (Figure 1), and interestingly, they maintain the genetic background of their donor [30–32].

Protocols for differentiating iPSCs to hepatocytes-like cells (HLCs) follow key steps in the ontogenic liver development using inductive and repressive signals, starting with the differentiation of iPSCs to definitive endoderm (DE), followed by hepatic endoderm (HE) specification and maturation of HE into hepatocyte-like cells (HLCs) [10,33].

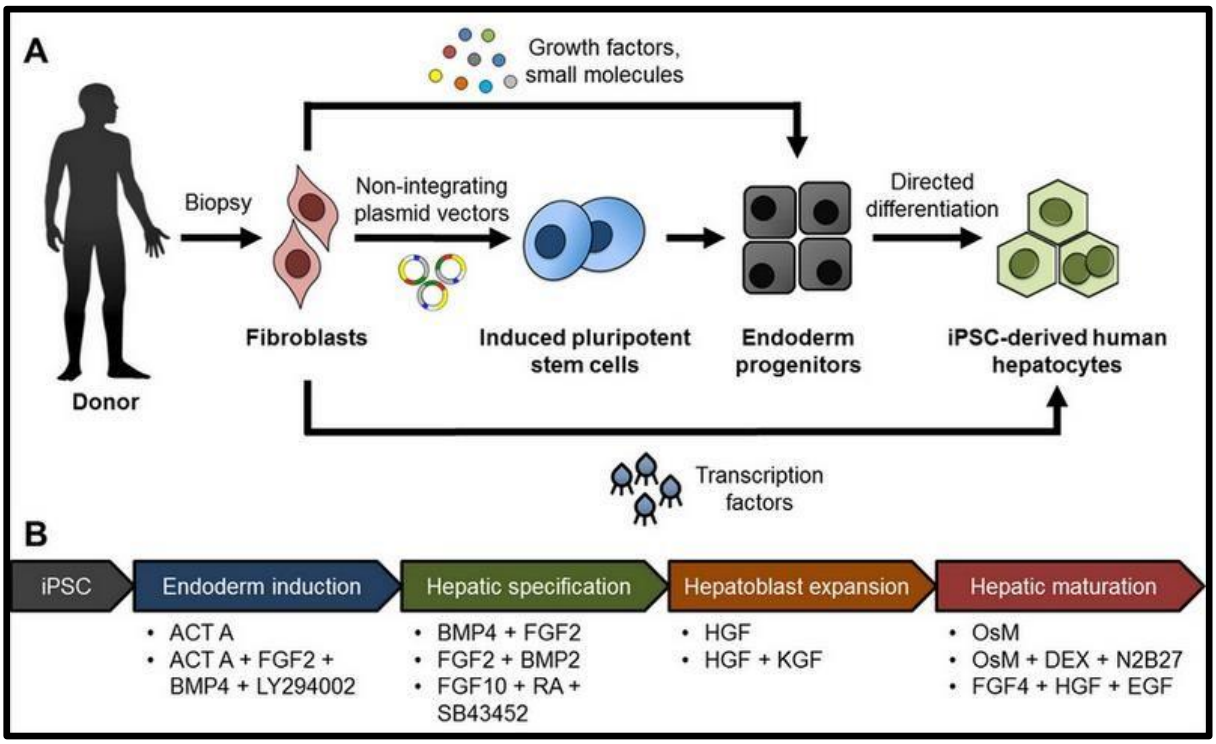

Figure 1. Generation of hepatocytes from induced pluripotent stem cells (iPSCs).

(A)depicts a flow diagram for conversion of human tissue biopsies using growth factors and small molecules into hepatic endoderm progenitors (top series) and finally direct differentiation into the iPSCs-derived human hepatocytes. Additionally, conversion of skin fibroblasts to iPSCs using Yamanaka transcription factors, followed by their differentiation into hepatocytes using inductive and repressive signals induced by transcription factors (middle series) and the bottom series, fibroblasts are converted directly into hepatocytes using transcription factors. (B) depicts a typical protocol for differentiation of iPSCs into hepatocytes-like cells through following ontogenic liver developmental steps with representative niche growth factors used by different groups [9,10,34]. *Adopted from* [35].

Definitive endoderm (DE) formation is a very crucial intermediate stage in ontogenic hepatic development and is achieved through culturing iPSCs in Activin A rich medium with bone morphogenetic protein 4 (BMP4) and fibroblast growth factor 2 (FGF-2) [10,30,33]. The resulting DE cells expresses SRY-box transcription factor 17 (SOX17), Forkhead box protein A2 (FOXA2), and the C-X-C Chemokine receptor 4 (CXCR4) [36]. Differentiation of DE cells to HE cells is achieved by adding FGF2 and BMP4 while simultaneously repressing the TGF-β signalling by removing Activin A [30,33].

Furthermore, the differentiation of HE cells into matured HLCs is achieved by culturing HE cells in hepatocyte maturation culture medium (HCM) supplemented with hepatocyte growth factor (HGF), dexamethasone (Dex) and Oncostatin M (OSM) [10,33]. The resulting HLCs express key functional markers such as albumin, CYP enzyme subfamily 3A4 (*CYP3A4*), transcription factors including hepatocyte nuclear factor 4-alpha (HNF4α). HLCs have been shown to perform essential functions of the mature hepatocytes such as ALB secretion, low density lipoprotein (LDL) uptake, urea metabolism, and glycogen storage, similarly to PHH [33,37,38]. However, persistent expression of foetal markers such as alfa-fetoprotein (AFP) and *CYP3A7* suggest the immature state of HLCs [33,39].

The foetal phenotype of the HLCs triggered several studies to improve the maturation and functionality of these cells [31]. These included the introduction of small molecules and chemicals to increase efficacy and reproducibility of hepatocyte differentiation protocols to avoid use of recombinant growth factors which are costly [9]. Despite these efforts, HLCs still exhibited foetal phenotype; thus, necessitating refinement of current protocols to produce HLCs exhibiting adult hepatocytes profile markers. Ang and colleagues argued that the three-step protocol for differentiation of PSCs to hepatocytes does not fully recapitulate ontogenic liver development *in vivo* [40]. Consequently, they defined a roadmap for differentiation of iPSCs to HLCs involving a transition through six consecutive lineages and thus identifying inductive and repressive signals at each juncture. Importantly, they discovered a temporarily dynamic action of signals to specify one fate at early stages of culture and later repressing its formation; thus, cautioning against the current differentiation protocols that heavily relied on providing the same signalling cues for a prolonged period [40]. The roadmap involved exploiting retinoic acid (RA) to upregulate the BMP and FGF pathways, while downregulating transforming growth factor beta (TGF-β) signalling within the first 24 hr of culture, and subsequently liver bud specification by activation of TGF-β, BMP and protein A kinase (PAK) pathways while repressing Wnt signalling. Finally, HLCs specification was achieved through addition of Notch inhibitor (DAPT), TGF-β inhibitor (A83-01), ascorbic acid phosphate 2 (AA2) and forskolin (FSK). However, the resulting HLCs still expressed suboptimal CYP3A4 activity compared to PHH, which remained the main concern.

1.3 Generation of non-parenchymal cells from iPSCs

1.3.1 Cholangiocytes

Like hepatocytes, cholangiocytes are derived from hepatoblast (Figure 4), a common progenitor found in the liver bud during the early stages of liver organogenesis [31,41,42].

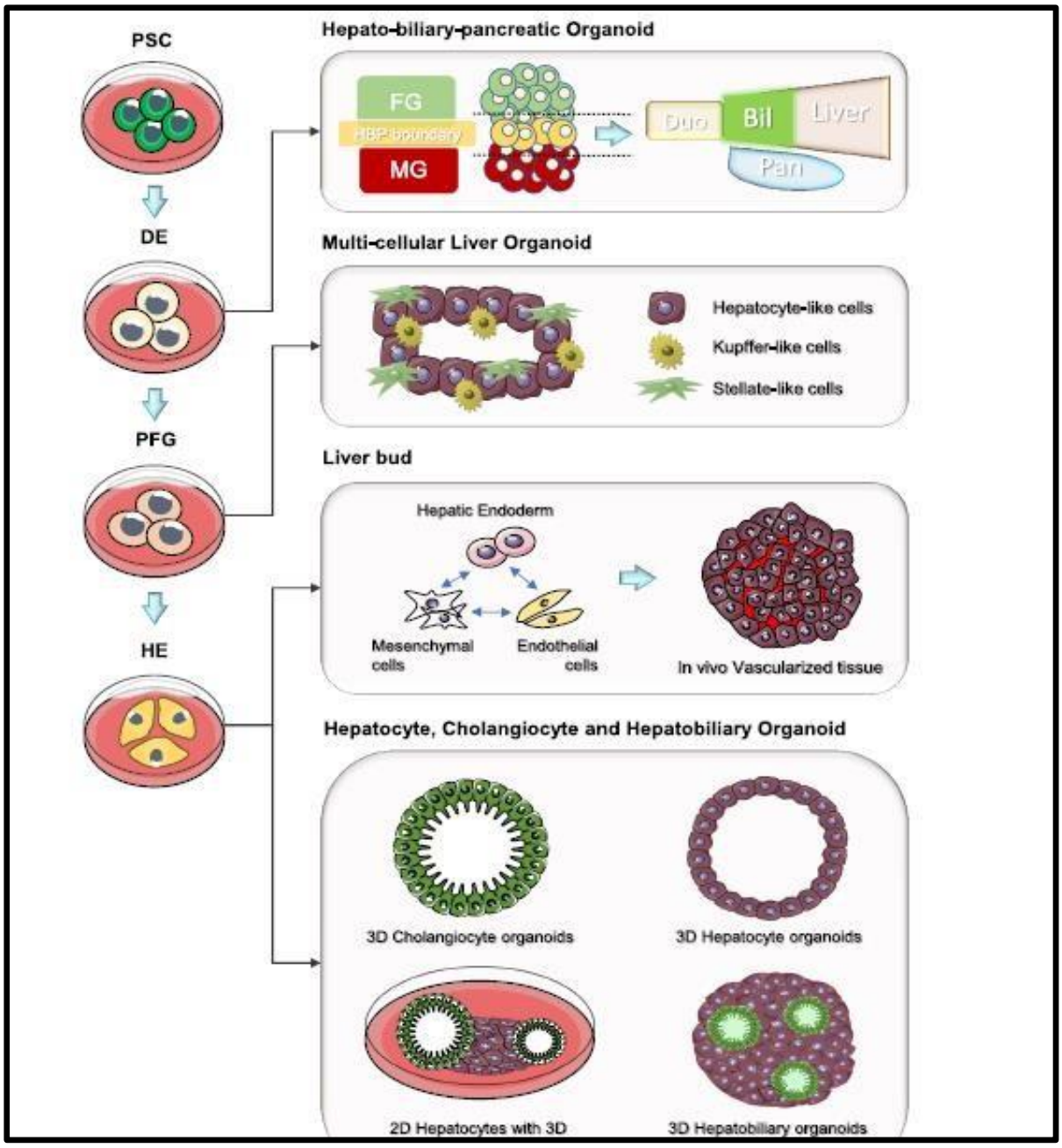

Figure 2. iPSCs-derived liver organoids.

iPSCs are provided with inductive and repressive signalling cues to differentiate along the endoderm lineage into cells resembling the DE, posterior foregut (PFG) and HE. These intermediate endoderm lineage progenitors are utilized to generate various liver

organoids. The DE can be used to generate the midgut (MG) and foregut (FG) spheroids. Furthermore, MG and FG co-culture induces hepato-biliary-pancreatic (HBP) organogenesis at the boundary to generate the HBP organoids containing cells and structures resembling the duodenum (Duo), pancreas (Pan) and liver that are interconnected by the biliary structures. PFG can be employed to generate multicellular liver organoids containing both parenchymal (hepatocytes) and nonparenchymal (HSCs and Kupffer cells) cells. The HE can be co-culture with mesenchymal stem cells and HUVEC to produce liver buds that further mature into vascularized tissues when transplanted in mice. Multiple groups have also further differentiated the HE to generate liver organoids that contain only cholangiocytes or hepatocytes, or hepatobiliary organoids containing both liver parenchymal cell types in different configurations. Adopted from [43].

A study from Dianat's group successfully generated cholangiocytes-like cells (CLCs) from hepatoblasts generated from hESCs and HepaRG cells that were cultured in defined media supplemented with growth hormones, epithelial growth factor (EGF), interleukin 6 (IL-6), and sodium taurocholate hydrate in the presence of ECM provided by collagen [41]. The resultant CLCs expressed mature cholangiocytes markers including cytokeratin 18 (CK18), CK19, osteopontin (OPN), Secretin Receptor (SCTR), cystic fibrosis transmembrane conductance regulator (CFTR), apical sodium-dependent bile acid transporter (ASBT), G-protein-coupled bile acid receptor (TGR5), and VEGF receptor 2 [41]. Additionally, lineage transcription factors such as Sox9, HNF6, and HNF1β were also expressed. The cells also formed functional cysts and bile ducts with apicobasal polarity.

1.3.2 Hepatic stellate cells (HSCs)

Hepatic stellate cells (HSCs) are liver-specific mesenchymal cells that play a critical role in the physiology and pathophysiology of the liver [44]. Under physiological conditions, HSCs remain in quiescent state in which their function is to store and transport vitamin A and lipid droplets [44]. Following damage of the tissue due to toxins or viral infections, HSCs become metabolically active and promote secretion of ECM involved in liver injury repair [29]. HSCs exhibit limited proliferation capacity in 2D models, fail to maintain quiescent phenotype and spontaneously lose key functional features *in vitro* [16]. Koui and colleagues demonstrated that iPSC-derived HSCs

progenitors could be expanded and matured *in vitro* and acquire lineage-specific characteristics [29]. These findings encouraged researchers to explore induction of iPSCs derived HSCs.

A recent study by Coll and colleagues established an efficient protocol for generating HSCs from iPSCs [16]. Briefly, iPSCs were differentiated into mesoderm progenitors in the presence of BMP4. To induce HSCs, mesothelial cells were subjected to retinol and palmitic acid and after 12 days of culture, the resulting HSCs exhibited similar morphology, transcriptome profile and functional attributes as human primary HSCs [16]. Additionally, when cultivated in 3D co-culture with HepaRG cells, HSCs stored vitamin A and upon exposure to acetaminophen (APAP), they switched from quiescent state to activated state as shown by increased expression of fibrogenesis markers and pro-collagen [16]. In conclusion, this method provided a proof-of-concept that mature, and functionally active non-parenchymal liver cells can be generated from iPSCs.

1.3.3 Liver sinusoidal endothelial cells (LSECs)

Liver sinusoidal endothelial cells (LSECs) are the highly specialized endothelial cells representing the interface between blood cells on the one side and hepatocytes and HSCs on the other side [45]. These cells are also specific-mesoderm derived cells that contribute to the liver physiology and pathophysiology [45]. In a healthy liver, hepatocytes, and HSCs function together to maintain homeostasis of LSECs through the release of VEGF. Hence, to model a liver, it is crucial that different cell types are present. A study by Koui and colleagues adapted the protocol for differentiation of embryonic stem cells (ESCs) into mesodermal cells (MSCs) that were positive for the endothelial marker, CD34 [29]. These cells resembled the morphology of endothelial cells and could be expanded in cultures for many passages while maintaining high expression levels of LSEC progenitor markers FLK1, CD34, CD31, CDH5, stabilin-1 (STAB1) and LYVE1 [29]. To induce maturation, progenitor cells were cultured in the presence of TGF-β inhibitor and hypoxic conditions that promoted the acquisition of mature endothelial morphology and expression of factor 8 (FVIII), stabilin-2 (STAB2) and Fc gamma receptor IIb (FC□RIIB) [29].

1.3.4 Kupffer cells (KCs)

Kupffer cells (KCs) are hepatic resident macrophages of monocytic origin located in the inner side of the hepatic sinusoids. These cells are specialized in scavenging and phagocytic functions, play a role in maintaining liver homeostasis and contribute to the pathophysiology of the liver. Tasnim and colleagues described a protocol for generation of mature induced KCs (iKCs) from human IMR90 fibroblast-derived iPSCs [46]. They differentiated iPSCs into pre-macrophages using a modified protocol from Wilgenburg and colleagues [47]. They generated embryoid bodies (EBs) expressing macrophage markers such as CD14, CD68, CD163, CD11 and CD32. EBs were further cultured in X-VIVO^{TM} media supplemented with monocyte-colony stimulating factor (M-CSF), interleukin-3 (IL-3) and β-mercaptoethanol to form pre-macrophages.

The formed pre-macrophages were cultured in a mix of conditioned primary hepatocytes media and advanced DMEM to generate induced Kupffer cells (iKCs) that expressed specific markers including C-type lectin family member 4 (CLEC-4F), inhibitor of differentiation 1 (ID1) and ID3. The iKCs exhibited similar morphology as the primary human macrophages. Moreover, microarray and qRT-PCR showed that iKCs had similar gene expression profile as the primary macrophages. Interestingly, iKCs phagocytosed and secreted interleukin 6 (IL-6) and tumour necrosis factor alpha (TNF-α) upon stimulation at levels like primary KCs but different to non-liver macrophages [46]. Therefore, these results suggested that patient's specific iKCs and hepatocytes can be used to model inflammatory diseases.

1.4 Liver organoids and extracellular matrix (ECM)

The fetal profile of HLCs and CLCs prompted researchers to develop alternative approaches to enhance the cells maturation to match the functional liver (*Table 1*). These led to unveiling of the culture and physiological conditions required for organoid formation by mimicking a series of events that occur during the liver morphogenesis [48]. Huch et al. demonstrated that long-term expansion of 3D organoids can be fully achieved through culturing cells in the presence of ECM provided by Matrigel drops [49]. 3D architecture enabled the cell-cell and cell-ECM interactions compared to monolayer cultures. Importantly, bile duct tissue-derived organoids differentiated into functional hepatocytes using specific defined differentiation medium (DM) in *in vitro* cultures and *in vivo* upon transplantation into mice [1].

In contrast to tissue-derived organoids, iPSCs-derived organoids generally consist of many cell types that self-organize to form complex structures (*Figure 4*). During the liver development, liver cells mature from same developmental progeny that is the liver bud. Takebe and colleagues generated 3D vascularized liver bud resembling adult liver tissue by co-culturing iPSC-derived hepatic endoderm cells with human umbilical cord veins MSCs in Matrigel-coated plates [13]. Transplantation of liver bud organoids rescued recipient mice from DILI. Subsequently, Takebe and colleagues overlaid a scalable liver bud production platform entirely from iPSCs [15]. This was achieved through conducting reverse experiments to identify three progenitor (hepatic endoderm, endothelium, and septum mesenchyme) populations that can effectively generate liver bud in a highly reproducible manner. They further developed an omniwell array culture platform for mass producing homogenous and miniatured liver buds on a clinically relevant scale [15]. Moreover, the liver buds rescued mice against acute liver failure (ALF) upon transplantation [15]. Although the initial method [13] has a great potential for regenerative medicine, the immature state still limits its application as human cell culture model. Additionally, resultant liver bud organoids favour differentiation rather than proliferation [50].

Zhang and colleagues developed a protocol to generate posterior gut endoderm cells (PGECs) from iPSC by exploiting FGF, TGF-β and Wnt signalling pathways [51]. They generated PGECs expressing CDX2 by culturing stem cells in the presence of EGF, VEGF, CHIR99021 and A83-01 [51]. Importantly, CDX2 positive PGECs maintained chromosomal stability and were successfully transplanted into immunocompromised mice without inducing teratomas [51]. The CDX2 positive cells, HUVECs and MSCs co-culture generated functional liver bud organoids that rescued mice from ALF [51]. This model hold potential for regenerative medicine and cell therapy.

In parallel, Mun and colleagues differentiated iPSCs into HLCs following steps of liver development using inductive and repressive signals specific for hepatocytes cell fate [10]. Organoids were generated in both the cell suspension or embedded in Matrigel, expanded for a very long time in culture and these cells were found to maintain normal karyotypes. Moreover, organoids differentiated under EM exhibited high expression of mature hepatocytes markers including ALB, antitrypsin alpha 1 (AT1A), multidrug resistance-associated protein 2 (MRP2), CYP3A4 and the ductal markers such as

cytokeratin 19 (CK19) compared to PHHs [10]. Expression of mature hepatocytes markers was strongly enhanced in DM, whereas expression of CK19, SOX9 and LGR5 was decreased in EM. Interestingly, these organoids preserved and exhibited all major liver functions including serum protein production, drug metabolism and detoxification of xenobiotic compounds. Also, they exhibited intact mitochondrial bioenergetics, regenerative capacity, and the inflammatory responses. These findings highlight the importance of utilizing ECM in liver organoids formation. Moreover, they suggested the need to grow 3D organoids in an environment that replicate the tissue niche as *in vivo.*

Both HLCs and CLCs organoids capture at least some functions of the liver. However, they are still lacking NPCs that are crucial for homeostasis and tissue response during disease and injury. More recently, Ouchi and colleague described a protocol for creating iPSCs-derived liver organoids that are comprised of HLCs, HSCs and KCs for modelling steatohepatitis [11]. The functional assays have demonstrated that HLO exhibited CYP3A4 activity after exposure to rifampicin that was comparable to that of PHH [11]. Treatment of these multicellular organoids with fatty acids (FA) for 5 days was adequate to induce inflammatory and fibrotic responses. Importantly, the authors also generated Wolman disease patient iPSC-derived organoids and showed that the HLO phenocopied the clinical features of disease [11]. Finally, they demonstrated that treating patient derived HLO with FGF19 improved survival of HLO in culture, reduced lipid accumulation, reduced ROS production, and reduced stiffening of HLO [11].

Table 1. Major pluripotent stem cells (ES & iPSCs) and progenitor cells or adult stem cells derived liver organoid platforms studies

Study author (s)	Type of organoid	Approach	Unique features and model applications
Huch et al. 2013, 2015	Biliary stem cell organoid	- Isolation and expansion of EPCAM+ biliary cells from liver biopsy - 3D Matrigel embedded culture	- Stable expansion of patient-specific adult liver biliary stem cells - Bipotent biliary stem cells can generate functional hepatocytes and cholangiocytes in culture and form functional hepatocytes when engrafted in mice (low efficacy)
Takebe et al. 2013 - Cells co-culture in 2D on Matrigel - Engrafted liver bud rescues genetic liver failure in mice	Liver bud	- Co-culture of iPSC-derived hepatic cells, HUVECs and MSCs forms 3D liver bud	- Self-organization of multiple cell types in vitro into a immature liver bud (lacks liver function) - Liver bud develops into functional and vascularized liver tissue when engrafted into immuno-deficient mice
Ogawa et al. 2015	Cholangiocyte-like cell (CLC) organoids	- Step wise differentiation of hiPSCs through bipotent hepatoblast - 3D Matrigel embedded culture	- Cholangiocytes exhibit mature biliary markers and structures such as apical sodium-dependent bile acid transporter, secretin receptor, cilia, and cystic fibrosis transmembrane conductance

			regulator (CFTR) - In vitro modelling of cystic fibrosis with patient derived iPSC
Sampaziotis et al (2015, 2017)	CLC organoids	- Step wise differentiation of hiPSCs through bipotent hepatoblast - 3D Matrigel embedded culture	- CLC is highly functional and utilized for validating polycystic drugs - Organoids were used to model cystic fibrosis - Engrafted CLC enable treatment of common bile duct (CBD) disorders

Study author (s)	**Type of organoid**	**Approach**	**Unique features and model applications**
Takebe et al. 2017	Liver buds	- Co-culture of single donor iPSC-derived hepatic endoderm, endothelial and mesenchymal cells - Engineered platform for large scale production	- Single donor iPSC-derived hepatic, endothelial and mesenchymal cells to generate patient specific liver buds - Mechanized engineering platform for robust large-scale production of liver bud - Liver rescue experiments achieved in over 100 mice to demonstrate potential for regenerative therapy
Nie et al. 2018	Liver buds	- Isolation of endothelial and mesenchymal cells from a single	- Reduced liver bud size and maturation *in vitro*
- Differentiated liver bud consisted mainly of			

		umbilical cord donor for liver bud organoid formation	hepatocytes and was used for modelling HBV infection
Ouchi et al. 2019	Multi-cellular organoid	- Stepwise differentiation of iPSC into liver organoid using an intermediate foregut spheroid progenitor - Cells were embedded in Matrigel	- Single cell analysis shows that organoid comprise both parenchymal and nonparenchymal cell types of the liver - Liver organoid treated with free fatty acid exhibited inflammatory response, underwent fibrogenesis which resulted in increased stiffness of the organoids
Mun et al. 2019; Akbari et al. 2019	Biliary stem cell organoid	Isolation and expansion of EPCAM+ bipotent progenitor from pluripotent stem cells - Cells were embedded in Matrigel - Bipotent Progenitor cells derived from PSC are like the biliary stem cell organoid platform reported by Huch et al. 2015 - Bipotent progenitor differentiated to hepatocyte in 3D, exhibited liver functions and demonstrated regenerative and inflammatory responses.	- iPSCs platform enabled modelling of genetic disease with patient derived fibroblast

1.5 Antiretroviral therapy-induced liver injury

Antiretroviral therapy (ART) induced liver injury is one of the most serious and relevant adverse effects of antiretroviral (ARV) drugs in patients infected with HIV/AIDS [52]. Approximately, 9-30% of patients taking ART develop ART-induced liver injury due to the toxicity of antiretroviral (ARV) drugs [52]. These drugs are classified into several groups based on the mechanism of action [53], each targeting a different vital part of the viral life cycle, including cell recognition and entry, DNA transcription, DNA integration, and cleavage of essential viral proteins (*Figure 3*). Entry/fusion inhibitors prevent the virus from fusing with the host cell membrane, either acting as a CCR5 antagonist, or by targeting CXCR4 co-receptors [54]. Maraviroc is a CCR5 antagonist that blocks gp120 from associating with the receptor [55]. Additionally, Enfuvirtide is a synthetic peptide that mimics part of the viral membrane protein gp41 and inhibits fusion with the host cell membrane [54].

Other groups are some of the nucleoside reverse transcriptase inhibitors (NRTIs) which were the first class of ARV drugs to be developed. NRTIs are phosphorylated intracellularly and are incorporated into the lengthening viral DNA strand. This class of ARV drugs either lacks a 3'-OH group or contains a modified group that prevents subsequent addition of nucleotides to the strand; thus, preventing all downstream viral action [56]. NRTIs are widely used in treatment cocktails, as they are effective and generally well tolerated [57]. Some of the most common NRTIs used regularly to treat HIV are tenofovir (TFV), emtricitabine (FTC), zidovudine (ZDV) and abacavir (ABC).

Non-nucleoside reverse transcriptase inhibitors (NNRTIs) are the third class of ARV drugs. These drugs inhibit viral reverse transcriptase by specifically binding to a non-substrate binding site of the enzyme, allosterically inhibiting DNA polymerization site [53,56]. Commonly used NNRTIs include efavirenz (EFV) and nevirapine (NVP).

Integrase inhibitors such as Raltegravir and dolutegravir are the most recent class of ARV drugs [55]. These drugs bind to the enzyme and mimic the DNA substrate/integrase interaction [55]. Integrase inhibitors are attractive ARV drugs as there are no equivalent enzymes found in the host cell; thus, limiting possible side effects [58].

Protease inhibitors block the viral enzyme by acting as competitive peptidomic inhibitors; thus, mimicking the transition state of the protease catalysis, and blocking the binding of viral proteins [59,60]. This class consists of drugs including saquinavir (SQV), ritonavir (RTV), and lopinavir (LPV).

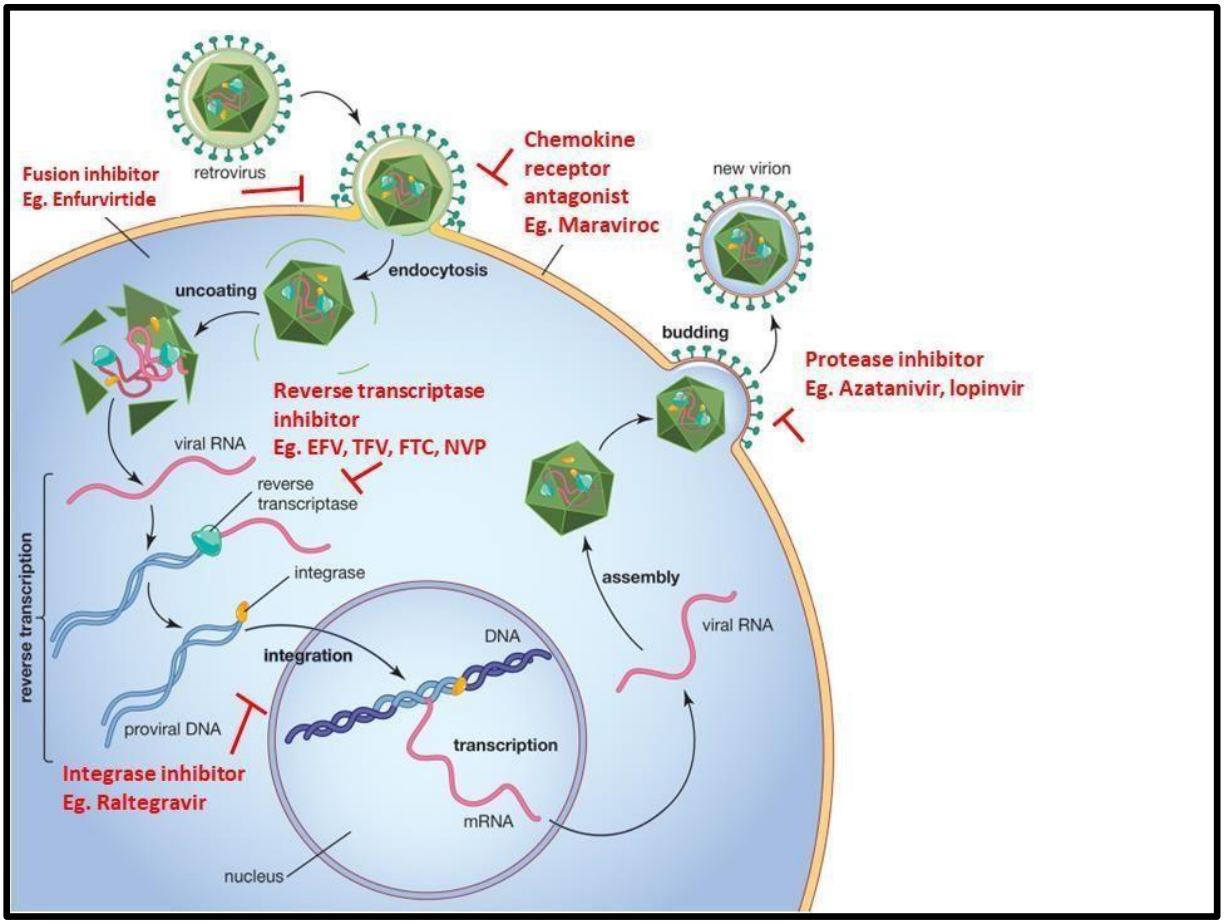

Figure 3. Schematic representation displaying key points in the HIV life cycle and mechanism of action of the main drug classes.

Drug classes interfere with HIV viral infection and replication. Inhibitory points are indicated by the red lines. Each drug exhibits its function based on its properties and inhibit HIV viral entry, infection, and replication.

ART is basically administered as a combination of two or more ARV drugs [57]. The first-line regimen includes EFV-based regimen which is composed TDF, lamivudine (3TC) and EFV or the NVP-based regimen consisting of NVP, TDF and 3TC [57]. Currently, WHO recommends the use of the integrase inhibitor DTG with TDF and 3TC in patience initiating ART and those currently on first-line ART if they present with viral load measurement <1000 copies/mL [57]. Moreover, DTG is recommended as the

second-line regimen consisting of ZDV and 3TC. All ART classes have been associated with hepatotoxicity and most commonly NNRTIs [57].

1.5.1 Epidemiology of antiretroviral therapy-induced liver injury

The incidence rate of DILI in HIV-infected patients taking ART ranges between 2-18% and up to 30% of these patients may require a change of the regimen or even discontinuation of therapy [32,61–63]. NNRTIs, NVP and EFV are the common ARVs associated with hepatic injury [61]. In fact, data suggests that NVP is associated with higher risk of developing liver injury with incidence rate of 28.6% [64]. Most cases of NVP-induced liver injury occur within the first three months of starting therapy. Moreover, it was previously reported that NVP use was associated with higher incidence of toxicity than EFV [65]. Although, EFV is recognized as an infrequent cause of ART-induced liver injury, accumulating evidence indicated that EFV causes hepatotoxicity characterized by sub-massive hepatocytes necrosis [66,67]. EFV hepatotoxicity is associated with a higher mortality rate of 11% [66,67].

NRTIs such as stavudine (d4T), which is a thymidine analogue, have also been reported to induce hepatoxicity in up to 50% of patients by transiently elevating the liver enzyme markers [68]. Another study observed a high incidence of hepatotoxicity in patients receiving either d4T/3TC [69]. PIs have also been shown to cause ART-induced liver injury with incidence rates of 1-9.5% and a few patients presented with liver related outcomes [70]. There is great variation in the incidence of hepatotoxicity among the reported studies and this could be attributed to ethnicity, concurrent use of medications, the prevalence of chronic viral hepatitis, grade of severity and follow-up duration. For instance, a retrospective study reported that a high incidence rate of NVP-based ART-associated hepatotoxicity (25.5%) was linked to the concurrent use of trimethoprim (TTP) or sulfamethoxazole (SMZ) in a Taiwanese cohort [71]. EFV associated hepatotoxicity has been reported in up to 8% of patients receiving EFV-based regimen and most of the cases were clinically asymptomatic [70].

A study showed that the median delay between ART initiation and hepatotoxicity occurrence ranged from 1-11 months [72], and 5 weeks in another study [73]. Interestingly, other studies have reported that patients discontinued the NVP-based ART due to hepatotoxicity before 3 months and after a mean of 9 months in another

study [74]. In contrast, a study by Van Griensven and colleagues observed occurrence of NVP hepatotoxicity in 27.6% of 29 cases within 6 months of initiating treatment [73]. Furthermore, ART-associated hepatotoxicity/DILI are the major cause of prolonged hospitalization and life-threatening events such as ALF in patients with HIV/AIDS [32,61,63,75]. These require probing and documentation of asymptomatic patients that are taking ART to screen and detect such cases to prevent the progression of ART-induced liver injury to liver failure.

1.5.2 Classification of ART-induced liver injury

Classically, DILI has been categorized into either having an underlying intrinsic or idiosyncratic mechanism of hepatotoxicity, but there is a newly emerged mechanism of hepatotoxicity termed indirect injury [76]. DILI is considered intrinsic when the toxicity of an insulting drug is dose-dependent and occurs in a predictable and reproducible manner. On the other hand, idiosyncratic DILI is often delayed in onset and is the result of idiosyncrasy of the drug receiver such as genetic and metabolic factors [77]. Indirect DILI is induced by the action of a drug rather than its direct toxicity or idiosyncratic properties [76]. Additionally, indirect DILI may represent an induction of a new liver disease or an exacerbation of pre-existing condition such as induction of immune-mediated hepatitis B or C virus [76].

Acetaminophen (APAP) is the most common cause of intrinsic DILI in the US and accounts for approximately 50% of ALF cases [78]. Moreover, studies have shown that 29% of patients with ALF secondary to APAP toxicity undergo liver transplant and these cases have mortality rate of 28% and ~10% of ALF cases linked to APAP toxicity occur at recommended doses [79–81]. The disparities in these findings could be attributed to genetic variation in DMEs responsible for metabolizing APAP in the liver. The unpredictable or idiosyncratic reactions account for most cases of DILI and these hypersensitivity reactions occur mostly independent of dose, and for each drug and they ultimately induce hepatocellular damage and cholestasis [52]. ART and antituberculosis (anti-TB) drugs are the most common cause of idiosyncratic DILI in patients with HIV and those co-infected with TB [52]. Additionally, intrinsic and idiosyncratic DILI may coincide together, where relatively elevated inflammatory stress may sensitize certain individuals to intrinsic hepatotoxins; thus, resulting in idiosyncratic liver injury [78,82]. This has been observed in patients hospitalized for

acute viral hepatitis, who developed liver injury following treatment with clinically safe doses of APAP [83].

1.5.3 Clinical presentation and diagnosis

Numerous studies define DILI as elevations of the liver enzymes mainly alanine transferase (ALT) and aspartate aminotransferase (AST) two-times upper limit of the normal (ULN) [84], although others use absolute threshold of liver enzymes regardless of the baseline levels [85]. These disparities in the criteria used in clinical studies to define DILI and its extent of severity has led to the implementation of a consensus report to define and grade DILI [85,86]. Based on the report, the clinical presentation of DILI has been classified biochemically and clinically into three main groups based on the *R* value ([ALT value/ALT UNL]/ [ALP value/ ALP ULN]). Moreover, DILI is categorized as hepatocellular when *R* value is greater than 5 (*R*>5), cholestatic when *R* value is less than 2 (*R*<2) and mixed when *R* is more than 2 but less than 5 (2<*R*<5) [84,87,88]. Furthermore, the DILI Expert Working Group and AIDS Clinical Trial Group have graded DILI severity into four grades based on baseline ALT or alkaline phosphatase (ALP) below the ULN [87,88]. Grade 1 (mild) is defined by 1.25-2.5 □ ULN ALT or ALP; Grade 2 (moderate) is characterized by 2.6-5.0 x ULN ALT or ALP; Grade 3 (severe) defined by 5.1-10 □ ULN ALT or ALP; and Grade 4 (severe) is defined by greater than 10 □ ULN ALT or ALP), and/or death, or transplantation due to DILI [87,88]. Incidences of DILI as well as the associated side effects vary between individuals due to their genetic profile and whether they are consuming other drugs.

1.6 Mechanisms of ART-induced liver injury

1.6.1 Host polymorphisms-mediate liver injury

Antiretrovirals drugs induce direct liver toxicity like any other drugs. Cytochrome P450 (CYP) enzymes play an essential role in drug metabolism [89]. EFV is metabolized primarily by CYP2B6 [90] and the non-synonymous single nucleotide polymorphism (SNPs), CYP2B6 c.516G>T (rs3745274) causes abnormal splicing, decreased expression and activity of the CYP2B6*6 [91]. Moreover, the presence of CYP2B6 c.516G>T variant promote a reduction of ~75% in EFV clearance and has been associated with increased EFV and NVP plasma levels [92,93]. Additionally, high plasma levels of these two drugs may lead to adverse effects such as central nervous

system and liver toxicity [92,94]. In addition to CYP2B6 C.516G>T, other studies have reported association between CYP2B6 c.983T>C variant and increased EFV plasma levels in different population groups including black South Africans and black African Americans [92,95,96]. Polymorphisms in CYP2A6 and CYP3A5 have also been reported to affect the pharmacokinetics of EFV [90], although the results are inconsistent.

Other CYP enzymes activities which may predispose patients to toxicity of drugs include CYP2E1 and CYP3A4. Evidence showed that an increased activity of CYP2E1 was associated with an increased risk of APAP-induced hepatic injury [97]. Cytochrome P450 enzyme activities including CYP2E1 and CYP3A4 can be induced by various factors such high fat diet and alcohol [97]. In addition, drug transporters also play a role in the uptake and efflux of endogenous compounds and certain drugs in and out of cells [98]. For instance, transporters like canicular MRP2 and 3 are involved in secretion of drugs and their metabolites into bile [99]. Altered expression of these transporters have been reported in patients with DILI [99]. Moreover, another study reported that SNPs of the drug uptake transporter from the blood to the liver, organic anion transporting polypeptide 1B1 (OATP1B1), predisposes patients to rifampicin-mediated liver injury [100].

1.6.2 Mitochondrial toxicities

The mitochondrion is an important organelle that plays a major role in energy production through glucose and fat metabolism, but also is the main source of reactive oxygen species (ROS), which may also lead to cellular demise [101,102]. Mitochondrial toxicity has been observed in HIV-positive patients treated with NRTIs [61]. This drug class selectively inhibits mitochondrial DNA (*Figure 4*), which leads to mitochondrial dysfunction [101,103]. Consequently, this leads to reduced oxidative phosphorylation and intracellular ATP levels [101]. Moreover, it leads to increased generation of ROS which may further cause cellular injury [103]. Studies using HepB3 and primary human hepatocytes revealed that EFV inhibited complex I of the electron transport chain (ETC), which led to reduced oxygen (O_2) consumption, decreased mitochondrial membrane potential (MMP), bioenergetic changes and elevated generation of ROS [104–106]. Furthermore, another study reported that EFV triggered endoplasmic reticulum (ER) stress and activated unfolded protein response (UPR)

observed as altered ER morphology and increased expression of several UPR genes [107].

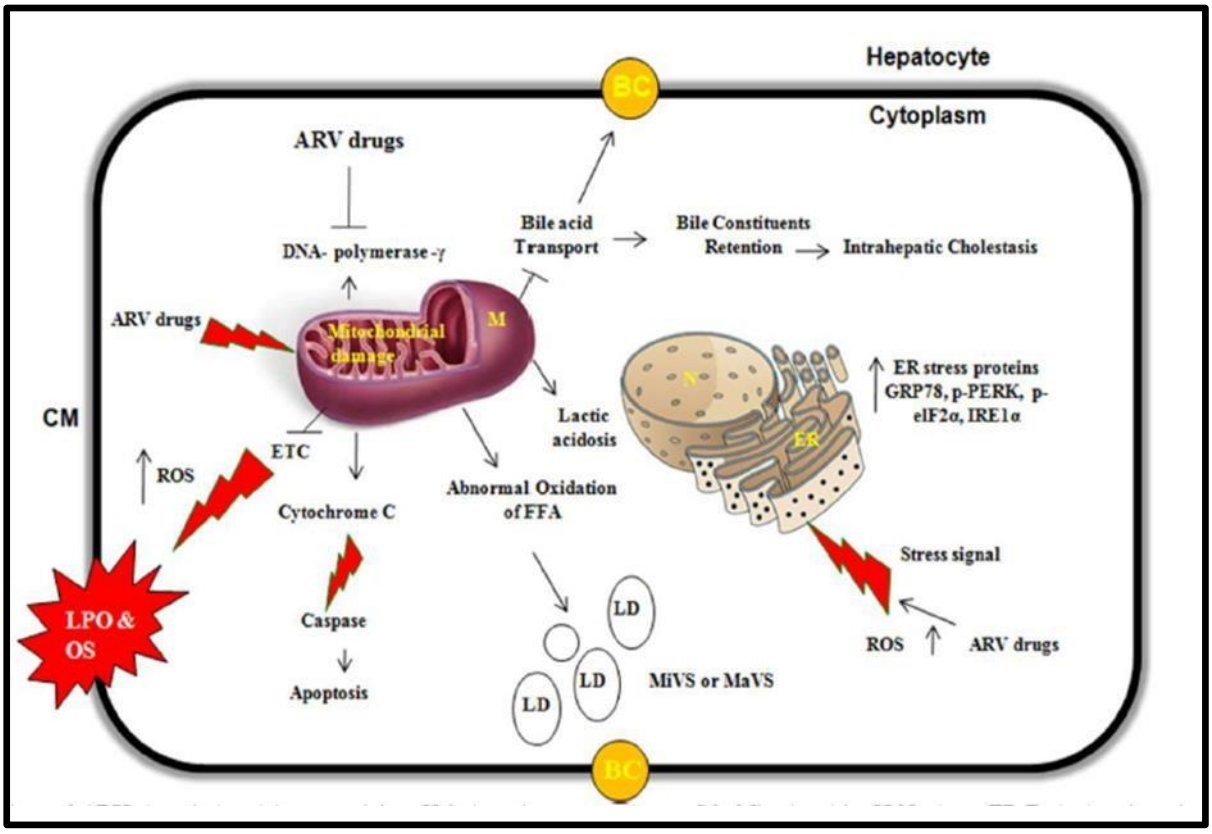

Figure 4. Mechanism of ARV induced mitochondrial toxicities liver.

Cumulative exposure to ARV drugs class NRTIs toxicities induces mitochondrial damage. These leads to induction of the death receptor pathway apoptosis, impaired electron transport chain (ETC) for ATP production thus ultimately increasing lipid peroxidation (LPO) and oxidative stress. Increased LPO and oxidative stress generates reactive oxygen species (ROS) which causes tissue damage. Mitochondrial damage leads to abnormal oxidation of free fatty acid thus enabling accumulation of lipid droplet inducing micro-vesicular or macro-vesicular steatosis (MiVs/MaVs). ARV drugs class NNRTIs impairs bile transport and increases bile retention thus inducing intrahepatic cholestasis. Also, ARV drugs induced stress signal my cause upregulation of endoplasmic reticulum stress proteins. Adopted from [68].

1.6.3 Immune-mediated mechanism or hypersensitivity

Allergic reactions are mostly idiosyncratic to the host and have an intermediate latency period ranging from days to weeks and are not dose related [101]. Hypersensitivity is

an extreme form of adaptive immune response induced when immune system reacts inappropriately to certain antigens; thus, leading to inflammatory reactions and tissue damage [108]. Abacavir-induced hypersensitivity reactions affect up to 5-8% of HIV positive patients and can be observed within the first 6 weeks of initiating ART [109]. Abacavir is thought to induce hypersensitivity through altering the repertoire of self-peptides presented on T cells, resulting in an immune reaction [108]. Symptoms include rash, fever, malaise, respiratory and gastrointestinal symptoms. Severe forms of skin rash associated with Abacavir may lead to Steven Johnson's Syndrome (SJS), toxic epidermal necrosis (TEN) and systemic lupus erythematous (SLE) [109]. Additionally, skin rash has been observed in 4% of patients initiating NVP-based regimens [68]. The NVP associated hypersensitivity is thought to be immune-mediated due to delayed onset of the reaction [102].

Human leukocyte antigen (HLA) alleles are implicated in Abacavir- and NVP-induced hypersensitivity [110,111]. Tangamomsuksan and colleagues conducted a meta-analysis study and reported a strong correlation between HLA-B*57:01 and Abacavir induced hypersensitivity [112]. However, several studies have demonstrated that other HLA alleles may be associated with a risk of ART-induced hypersensitivity [108,109,112]. A more recent meta-analysis study reported that patients carrying HLAA*24, HLA-B*18, *35, *39, *51, *81, and HLA-C*04 were associated with a higher risk of hypersensitivity [111]. Conversely, subjects carrying HLA-B *15, HLA-C *02, *03, *07 and HLA-DRB1 *05, *15 were associated with reduced risk of hypersensitivity [111].

1.6.4 Immune reconstitution

Liver damage is mediated by cytotoxic immune responses in immunocompetent individuals. In HIV/HBV co-infected patients with advanced immunosuppression, HBV replication generally increased due to weak cytotoxic immune responses and HBV related inflammation lessened and transaminase levels remained normal [113]. Improved cellular immunity upon initiation of highly active antiretroviral therapy (HAART) can lead to flares in liver enzymes and seroconversion, even in the absence of anti-HBV active drug [113,114]. In agreement, a study by Matthew and colleagues reported high incidence of hepatic flares and high rate of HBeAg seroconversion among HBeAg-positive early cases [114]. HBV flares are seen in 20-25% of patients

after initiation of HAART, and an estimated 1-5% of these patients develop clinical hepatitis [115].

Chapter 2: Research problem statement

2.1 Rational of the study

Chronic liver disease remains the major cause of health problems affecting thousands of people worldwide. Currently, the whole allograft transplantation is the only viable treatment option for end stage liver disease [116]. However, a lack of suitable donors, high costs, and surgical complications [7,116] and the management difficulties encountered provided the impetus to pursue representative *in vitro* liver models with the capacity to fully recapitulate liver functions [3]. Notably, traditional 2D *in vitro* models widely used in drug toxicity analysis studies and prediction of hepatotoxic compounds were using either PHH cells which are considered the “gold standard” for evaluation of hepatic drug metabolism [6] or immortalized cell lines mainly HepG2 or the HepaRG cells [4,5]. However, the PHH cells are limited to acute drug exposure studies since they cannot survive for a period longer than 72 hours in culture. Prolonged PHHs cultures result in rapid dedifferentiation of cells leading to the loss of normal hepatocyte cell morphology, structure and functions such as impaired DMEs activities [7]. Immortalized cell lines have proved to be inferior due to lack of expression of drug transporters and suboptimal DMEs activities compared to PHH cells [5]. Furthermore, 2D models lack cellular microenvironment such as cell-cell contact and cell-ECM interaction as in *in vivo* [11].

Advances in stem cell technology offers a great opportunity to generate patient specific HLCs derived from iPSCs using 3D organoid platforms [10]. Importantly, 3D organoids confer advantages for differentiation of iPSCs into hepatocytes with optimum metabolic functions [10,11]. However, most organoid models comprise of HLCs only; thus, lack the supportive cellular components such as profibrotic, sinusoidal endothelial and inflammatory cell lineages, which are important to maintain tissue functions and homeostasis [1,12]. Godoy et al demonstrated limited abilities of mono-hepatocytes in reproducing the hepatotoxic effects as observed *in vivo* [6]. Importantly, toxicity responses *in vivo* are mediated by the integrated complex interplay between different cells; therefore, the predictive role of hepatocytes or HLCs alone is limited.

Interestingly, Ouchi and colleagues developed a protocol for generating multicellular human liver organoids composed of HLCs, HSCs and KCs to model steatohepatitis (NASH) [11]. This is the suitable model to utilize to understand the interplay between

different cell lineages involved in tissue injury and homeostasis. Hence, the aim of the work presented in this thesis was to generate and develop 3D multicellular human liver organoids (HLO) from iPSCs to model complex liver diseases. Strikingly, earlier studies evaluating the hepatotoxicity of ARV drugs relied heavily on using 2D human or mouse PHH models, which have limitations to mimic drug toxicities observed *in vivo*. Also, there are currently no studies that have been performed to determine the mechanisms of hepatotoxicity induced by a combination of ARV drugs given to patients. In fact, the few mechanistic studies that have been performed thus far, investigated toxicity of a single ARV drug, mostly EFV or NVP [64,67,117,118]. Hence, it is very critical to understand the molecular mechanism of ART-induced liver injury. Therefore, the final aim of the research study presented in this thesis was to investigate and elucidate the molecular mechanism of ART-induced liver injury in HLO using a mass spectrometry approach.

2.2 Research hypothesis

Since 3D organoids recapitulate tissue structure and functionality of the native organ, and that HLO comprise HLCs, HSCs and KCs, which are important for maintaining tissue injury and homeostasis, we hypothesise that HLO treated with ART will recapitulate events that occur in the liver of patients taking ART and thus allow us to determine the molecular drivers of ART injury.

2.3 Objectives

We had the following objectives:

- To generate 3D multicellular liver organoids (HLO) derived from induced pluripotent stem cells (iPSCs).
- To validate specific stage representative gene markers and to determine the presence of epithelial, pre-fibrotic and inflammatory cell lineages in HLO.
- To determine the proteome of 3D HLO treated with ART, A+TB and TGZ compared to Untreated HLO (UN) using mass spectrometry approach.

Chapter 3: Materials and Methods

3.1 Chemicals & materials

All the chemicals, analytical reagents and cell culture mediums used were purchased from reputable vendors and distributors including Sigma-Aldrich, Gibco, Invitrogen, Lonza, Qiagen, Stem Cell Technologies, Life Technologies, R&D Systems, Anatech, Bio-Rad Laboratories, Corning, Biocom Africa, integrated DNA Technology (IDT), BD Sciences, Bioscience, Whitehead Scientific (Pty) Ltd, Promega and ThermoFisher Scientific. Items not purchased from the above companies are indicated where required. All cell culture medium, enzymes, and buffers were stored at 4°C and reconstituted growth factors and drugs were stored at –20°C or –80°C as per manufacturer's recommendations.

3.1.1 Growth factors and supplements

3.1.1.1 CST vitronectin (VTN)

Vitronectin (VTN-1ml, catalogue # A27940) was purchased from Life Technologies and stored at –80°C. VTN stock solution (60 µL) was aliquoted into Eppendorf tubes and stored at –80°C until needed for experiments. A working solution of 0.5 µg/cm^2 per well of a 6-well plate was achieved by diluting 60 µL of stock VTN in Dulbecco phosphate buffered saline (DBPS; catalogue #: 14190-094, Gibco)

3.1.1.2 Rho kinase protein (ROCK) inhibitor (Y-27632)

Y-27632 (5 mg, catalogue # Y0503) was purchased from Sigma-Aldrich and stored at 4°C. A stock (10 mM) solution of Y-27632 was achieved by reconstituting 5 mg of the Y-27632 in 1 mL DMSO. A 10 µM working solution was achieved by aliquoting the stock solution and stored at –20°C until needed for experiments.

3.1.1.3 Activin A

Activin A (10 µg, catalogue # 338-AC) was purchased from R&D Systems and stored at –20°C. A stock (100 µg/mL) solution of Activin A was achieved by reconstituting 10 µg of Activin A with 100 µL of 4 mM HCl. A 1000 ng/mL of Activin A working solution was achieved by diluting Activin A stock solution in RPMI-1640 + GlutaMAX™ (catalogue #: 61870-036, Gibco) and stored at –20°C until needed for experiments.

3.1.1.4 Bone morphogenetic protein 4 (BMP-4)

Bone morphogenetic protein 4 (BMP-4, 10 µg, catalogue # 314-BP) was purchased from R&D Systems and stored at –20°C. A stock (100 µg/mL) solution of BMP-4 was achieved by reconstituting 10 µg of BMP-4 with 100 µL of 4 mM HCl containing 0.1% bovine serum albumin (BSA, catalogue # A8531, Sigma-Aldrich). A 1000 ng/mL working solution was achieved by diluting BMP-4 stock solution in RPMI-1640 + GlutaMAX and stored at –20°C until needed for experiments.

3.1.1.5 Knockout serum replacer (KSR)

A 500 mL bottle of KSR (catalogue #: 10828028, Gibco) was purchased from ThermoFisher Scientific and stored at –20°C. A stock solution of KSR was prepared by aliquoting KSR into 15 mL tubes and stored at –20°C until needed for experiments.

3.1.1.6 Fibroblast growth factor 4 (FGF-4)

Fibroblast growth factor (FGF-4, 25 µg, catalogue # 235-4F) was purchased from R&D Systems and stored at –20°C. A stock (100 µg/mL) solution of FGF-4 was achieved by reconstituting 25 µg of FGF-4 in 250 µL in sterile phosphate buffered saline (PBS; catalogue # BE17-517Q, Lonza) containing 0.1% BSA. A 1000 ng/mL working solution was achieved by diluting FGF-4 stock solution in Advanced DMEM/F12 (catalogue # 12634-010, Gibco^{TM}) and stored at –20°C until needed for experiments.

3.1.1.7 CHIR99021

(CHIR99021, 5 mg, catalogue # SML1046) was purchased from Sigma-Aldrich and stored at –20°C. A stock (10 mM) solution of CHIR99021 was achieved by reconstituting 50 mg of CHIR99021 in 1 mL dimethyl sulfoxide (DMSO; catalogue # D2650, Sigma-Aldrich). A 1 mM working solution was achieved by aliquoting the CHIR99021 stock solution in Advanced DMEM/F12 and stored at –20°C until needed for experiments.

3.1.1.8 Retinoic acid (RA)

Retinoic acid (RA, 50 mg, catalogue # R2625) was purchased from Sigma-Aldrich and stored at –20°C. A 10 mM stock solution was prepared by reconstituting 25 mg RA in 1 mL DMSO. A 1000 µM working solution was achieved by aliquoting the RA stock solution in Advanced DMEM/F12 and stored at –20°C until needed for experiments.

3.1.1.9 Hepatocyte growth factor (HGF)

Hepatocyte growth factor (HGF, 5 µg, catalogue # H9661) was purchased from Sigma-Aldrich and stored at –20°C. A stock (5 µg/mL) solution of HGF was achieved by reconstituting 5 ug of HGF in 1 mL of sterile PBS containing 0.1% BSA. A 1000 ng/mL HGF working solution was achieved by diluting the HGF stock solution in hepatocyte culture medium (HCM, catalogue #: CC-3198, Lonza) and stored at –20°C until needed for experiments.

3.1.1.10 Dexamethasone (Dex)

Dexamethasone (Dex, 5 mg, catalogue # D4902) was purchased from Sigma-Aldrich and stored at –20°C. A 10 mM stock solution was prepared by reconstituting 5 mg Dex in 1 mL DMSO (Sigma-Aldrich). A 1 mM working solution was achieved by diluting Dex stock solution in HCM and stored at –20°C until needed for experiments.

3.1.1.11 Oncostatin M (OSM)

Oncostatin M (OSM,10 µg, catalogue # 295-OM) was purchased from R&D Systems and stored at –20°C. A stock (100 µg/mL) solution of OSM was achieved by reconstituting 10 µg of OSM with 100 µL sterile PBS containing 0.1% BSA. A 1000 ng/mL working solution was achieved by diluting OSM stock solution in HCM and stored at –20°C until needed for experiments.

3.1.1.12 Fibroblast growth factor 10 (FGF-10)

Fibroblast growth factor 10 (FGF-10, 25 µg, catalogue # F8924) was purchased from Sigma-Aldrich and stored at –20°C. A stock (100 µg/ml) solution was achieved by reconstituting 25 µg FGF-10 in sterile PBS containing 0.1% BSA. A 10 µg/mL working solution was achieved by diluting FGF-10 stock solution in Advanced DMEM/F12 and stored at –20°C until needed for experiments.

3.1.1.13 Epidermal growth factor (EGF)

Epidermal growth factor (EGF- 200 µg, catalogue # 236-EG) was purchased from R&D systems and stored at –20°C. A stock (500 µg/mL) solution was achieved by reconstituting 200 µg EGF in sterile PBS. A 10 µg/mL working solution was achieved by diluting EGF stock solution in Advanced DMEM/F12 and stored at –20°C until needed for experiments.

3.1.1.14 Vascular endothelial growth factor (VEGF)

Vascular endothelial growth factor (VEGF, 10 µg, catalogue # 293-VE) was purchased from R&D Systems and store at –20°C. A stock (100 µg/mL) solution was achieved by reconstituting 10 µg VEGF in sterile PBS containing 0.1% BSA. A 10 µg/mL working solution was achieved by diluting VEGF stock solution in Advanced DMEM/F12 and stored at –20°C until needed for experiments.

3.1.1.15 A83-01

A83-01 (10 mg, catalogue # 2939) was purchased from R&D Systems and stored at –20°C. A stock (10 mM) working solution was achieved by reconstituting 10 mg A8301 in 1 mL DMSO. A 1 mM working solution was achieved by diluting Dex stock solution in HCM and stored at –20°C until needed for experiments.

3.1.2 ART drug preparations

3.1.2.1 Efavirenz (EFV)

Efavirenz (EFV, catalogue # 025M4780) was purchased from Sigma Aldrich and stored at –20°C. A 10 mM stock solution of EFV was prepared. EFV was diluted in 500 µL dimethyl sulfoxide (DMSO) (Sigma Aldrich) and 500 µL media (either $DMEM^{++}$ or Full Williams E) and stored at –20°C. A 100 µM working solution was further diluted in media (either $DMEM^{++}$ or Full Williams E) and stored at –20°C until needed for experiments.

3.1.2.2 Tenofovir (TDF)

Tenofovir (TDF, catalogue # SML1795) was purchased from Sigma Aldrich and stored at –20°C. A 10 mM stock solution of TDF was prepared. 2.87 mg was diluted in 1 mL of ddH_2O and stored at –20°C. A 100 µM working solution was further diluted in media (either $DMEM^{++}$ or Full Williams E) and stored at –20°C until needed for experiments.

3.1.2.3 Lamivudine (3TC)

Lamivudine (3TC, catalogue #: L1295) was purchased from Sigma Aldrich and stored at room temperature. A 10 mM stock solution of 3TC was prepared. 10 mg of 3TC was diluted in 4.36 mL of ddH_2O. A 100 µM working solution was further diluted in Media (either $DMEM^{++}$ or Full Williams E) and stored at –20°C until needed for experiments.

3.1.3 Anti-TB drug preparation

3.1.3.1 Rifampicin (RIF)

Rifampicin (RIF, catalogue #: R3501) was purchased from Sigma Aldrich and stored at –20°C. A 10mM stock solution of RIF was prepared, 8.23 mg was diluted in 500 µL dimethyl sulfoxide (DMSO) (Sigma Aldrich) and 500 µL media (either $DMEM^{++}$ or Full Williams E) and stored at –20°C. A 100 µM working solution was further diluted in media (either $DMEM^{++}$ or Full Williams E) and stored at –20°C until use until needed for experiments.

3.1.3.2 Isoniazid (INH)

Isoniazid (INH, catalogue # MKCF2223) was purchased from Sigma Aldrich and stored at –20°C. A 10 mM stock solution of INH was prepared. INH was diluted in 1 mL of media (either $DMEM^{++}$ or Full Williams E) and stored at –20°C. A 100 µM working solution was further diluted in media (either $DMEM^{++}$ or Full Williams E) and stored at –20°C until needed for experiments.

3.1.4 Antigen preparation

Schistosome egg antigen (SEA; 1 mg/mL) was obtained as a gift from the laboratory of Prof Frank Brombacher at the University of Cape Town. The antigen was stored at –20°C until required for experiments.

3.2 Tissue culture

3.2.1 Human induced pluripotent stem cells (iPSCs)

Human pluripotent stem cells (iPSCs) cell line (*N-N*) used in this study was kindly provided as a gift by Dr Janine Scholefield from the Council for Scientific and Industrial research (CSIR) in South Africa.

3.2.2 Human induced pluripotent stem cells (iPSCs) maintenance

Briefly, undifferentiated iPSCs were cultured onto a CTS VTN-coated 6-well plates in Essential 8 medium (E8M, catalogue #: A1517001, Gibco) with 1% (v/v) penicillinstreptomycin (catalogue # 15140-122, Gibco). Cultures were maintained for approximately 5-6 days with 95% daily medium exchange and 80% confluent colonies were passaged for maintenance or differentiation at 1:6 and 1:3 ratios, respectively. For passaging, cells were dissociated into cell clusters from the culture plates using 0.5 M ultrapure EDTA solution (catalogue # 15575-020, Invitrogen) and incubated at

room temperature for 4-8 minutes. For differentiation, cells were dissociated into single cells using the Accutase solution (catalogue # A6964, Sigma-Aldrich) and incubated for 3 minutes in the incubator. Dissociation solutions were neutralized with equal volumes of growth medium to stop enzyme digestion. Cell suspensions were transferred to 15 mL falcon tubes containing 4 mL E8M + Y23762 solution and centrifuged at 1800 rpm for 3 minutes. Supernatant was discarded and remaining pellet was resuspended in 1 mL E8M + Y23762 solution. To do cell counting, 10 µL of cell suspension was mixed with 10 µL Trypan blue (0,4% and 0,55% NaCl) solution (catalogue # 15250061, Gibco). Cells suspended in Trypan blue were then ejected onto Countess cell counting chamber slide (catalogue # C10283, Invitrogen) and read with Countess II (catalogue #AMQAX1000, Invitrogen). Cells were seeded according to desired cell densities for differentiation. All cultures were maintained at 37°C in a 5% CO_2 in a water-jacket incubator.

3.2.3 Foregut induction

Human iPSCs were first differentiated into definitive endoderm (DE) and then foregut spheroids using a previously described protocol with slight modifications [119]. Briefly, 80% confluent human iPSCs were detached with Accutase and seeded onto CST VTN-coated plates in E8M at a density of 1.5 □ 10^6 cells/well for 24 hrs. After 24 hrs, E8M was exchanged with RPMI-1640 medium + GlutaMAX, 1% (v/v) Penicillin-streptomycin (10 000 U/mL, catalogue # 15140122, Gibco), supplemented with 100 ng/ml Activin A, 50 ng/ml BMP-4 at day 1, 100 ng/ml Activin A and 0.2% (v/v) KSR at day 2, and 100 ng/ml Activin A and 2% (v/v) KSR at day 3. On day 4-6, DE cells were further cultured in advanced DMEM/F12 with B27 (catalogue # 17504-044, Gibco), GlutaMAX (catalogue # 35050-038, Gibco) and N2 (catalogue #: 17502-048, Gibco) supplements, respectively, containing 500 ng/ml FGF4 and 3 µM CHIR99021. Cells were maintained at 37°C in a 5% CO_2 water-jacket incubator and media was exchanged daily.

3.2.4 Generation of human liver organoids (HLO)

At day 7, cells were detached from the plate with Accutase solution. Detached cells were transferred to a Falcon tube with medium and centrifuged at 1800 rpm for 3 min. Supernatant was discarded and the remaining pellet was resuspended in 1 mL of 100% Geltrex (catalogue # A1413302, Life Technologies). 40 µL of Geltrex-cell

suspension was cultured in 24-well Nunclon sphera multi-well plates (catalogue # 174930, ThermoFisher Scientific) and incubated for 15-20 minutes to allow Geltrex to solidify. Cells were exposed to Advanced DMEM/F12 with 1□ B27 and 1□ N2, supplemented with 2 μM RA for 4 days with a daily medium change. After treatment with RA, media was switched to HCM supplemented with 10 ng/ml HGF, 0.1 μM Dex and 20 ng/ml OSM. Cultures for HLO were maintained at 37°C in 5% CO_2 with 95% air, media was replaced every second day. HLO were scratched and pipetted to perform downstream applications and analysis from day 20-30.

3.2.5 HepaRG cells

HepaRG cells (terminally differentiated hepatic cells derived from a human hepatic progenitor cell line) were cultured in Williams E Media without L-glutamine and phenol red (catalogue # W1878, Sigma-Aldrich) supplemented with 10% FBS, penicillin-streptomycin (1% v/v), 5 μg/mL insulin (catalogue # 1243, Sigma-Aldrich), 2 mM L-glutamine (catalogue # BE17-605E) and $5x10^{-5}$ M hydrocortisone hemisuccinate (catalogue # H2882, Sigma-Aldrich). All cell cultures were incubated at 37°C in a 5% CO_2 water-jacket incubator.

3.2.6 Generation of 3D HepaRG cell cultures

1 □ 10^6 HepaRG cells were seeded in a 75 cm^2 flask and were incubated at 37 °C with 5% CO_2 and medium was changed every 2 days. After 14 days, cells were treated with trypsin prior to dissociation with a syringe to obtain a suspension of single cells. Then, cells were further seeded in Nunclon Sphera 96-well U bottom plates (catalogue # 174929, Thermo Scientific™) at a seeding density of 72 000 cells/well. Medium was changed after 7 days, and spheroids were used at Day 10.

3.3 Molecular biology assays

3.3.1 RNA extraction

Total ribonucleic acid (RNA) was extracted from plated cells using TRIzol reagent (ThermoFisher Scientific) following the manufacturer's instructions. The extracted RNA was quantified using ND-1000 Nanodrop spectrophotometer (ThermoFisher Scientific, USA) and stored at –80°C until needed for further experiments.

3.3.2 Complementary DNA (cDNA) synthesis

For first strand cDNA synthesis, total RNA was reverse-transcribed using ImProm-II

Reverse Transcriptase (catalogue # PRA800, Promega) following the manufacturer's instructions as indicated in (Table 2 and 3). 2 µg of template mRNA, 1 µL Oligo dT and ddH_2O were mixed to a final volume of 9 µL. This mixture was heated for 10 minutes at 70°C in a thermal block cycler with a heated lid to denature any secondary structures in the RNA and to minimize evaporation of solutions. The mixture was then chilled on ice for 5 minutes.

Table 2. First strand cDNA synthesis cocktail

2 µg mRNA	Oligo dT primer	ddH_2O	Total volume
X	1 µl	Y	9

16 µL of the second cocktail (Table 2) was added and mixed by pipetting, followed by centrifugation, and then annealed the Oligo dT primers to the template at 25°C for 5 minutes followed by 2 hours incubation at 42°C. Reverse transcriptase was inactivated by heating for 10 minutes at 70°C, followed by stopping the reaction by placing the tube on ice.

Table 3Table 3. cDNA synthesis master mix

Reagents	Volume (µL)
5X first synthesis strand buffer	5
dNTPs mix	1
RNase inhibitor	1
$MgCL_2$	2
Impromp II Reverse Transcriptase	1
ddH_2O	6
Total	16

3.3.3 Quantitative Reverse Transcriptase-Polymerase Chain Reaction (qRTPCR)

qRT-PCR was carried out in triplicates using a PowerUp™ SYBR™ Green Master Mix (catalogue # A25741, Applied Biosystems) and synthesized cDNA was amplified in a Thermal Cycler (QuantStudio 3 RT-PCR Systems, ThermoFisher Scientific) with heated lid. Relative mRNA gene expression was calculated using the $2^{-\Delta\Delta Ct}$ method,

with *GAPDH* as the normalization control. All primers (Table 3) were purchased from IDT.

Table 4. All primer pair sequences for quantitative RT-PCR.

Human stem cell markers		
Gene name	**Forward primer sequence (5'-3')**	**Reverse primer sequence (5'-3')**
Oct-4	*CAGGAGATATGCAAAGCAGAAAC*	*GGCACTGCAGGAACAAATT*
Nanog	*AGCCTAATCAGCGAGGTTTC*	*CAGAGCAAGACTCCGTTTCA*
Sox2	*GCTACAGCATGATGCAGGACCA*	*TCTGCGAGCTGGTCATGGAGTT*
Definitive endoderm (DE) markers		
Sox17	*CGCACGGAATTTGAACAGTA*	*GGATCAGGGACCTGTCACAC*
GSC	*GAGGAGAAAGTGGAGGTCTGGTT*	*CTCTGATGAGGACCGCTTCTG*
Foregut spheroid (FGS)		
HHEX	*GCCCTTTTACATCGAGGACA*	*AGGGCGAACATTGAGAGCTA*
Immature human liver organoids markers		
HNF4α	*CATGGCCAAGATTGACAACCT*	*TTCCCATATGTTCCTGCATCAG*
AFP	*ACCATGAAGTGGGTGGAATC*	*TGGTAGCCAGGTCAGTCAAA*
CYP3A7	*GAAACACAGATCCCCCTGAA*	*TCAGGCTCCACTTACGGTCT*
Mature human liver organoids markers		
ALB	*TTG GCA CAA TGA AGT GGG AAA GGC AAT CAA CAC CAA TA*	*GG*
A1AT	*CCACCGCCATCTTCTTCCTGCCTGA*	*GAGCTTCAGGGGTGCCTCCTCTGTG*
CYP3A4	*TGTGCCTGAGAACACCAGAG*	*GTGGTGGAAATAGTCCCGTG*
GAPDH	*CCATCTTCCAGGAGCGAG*	*GCAGGAGGCATTGCTGAT*

3.4 Flow cytometry

For flow cytometry, HLO were dissociated into single cells using Trypsin-EDTA for ~15 minutes. Samples were washed with 1□ PBS and stained with 100 µL antibody master mix (FACS buffer: 1% bovine serum albumin (BSA) in 1□ PBS) containing specific antibodies. Subsequently, samples were incubated for 30 minutes in the dark or covered with foil at room temperature. Cells were resuspended in FACS buffer and transferred into FACS tubes. The cells were acquired on a BD LSR Fortessa machine and data was analysed using FlowJo (version 10) software (Treestar, USA).

The human antibodies (HAb) targeting the following cell surface markers were used: EpCAM-BV412 (1:80; BioLegend), CD166-PE (1:160; eBioscience) and CD68-PECy7 (1:80; eBioscience).

3.5 Cytochrome activity determination

3.5.1 Plating strategy

To normalize HLO seeding for CYP3A4 activity, after harvesting cells with TrypLE™ and manual pipetting for disruption into single cells, HLOs were filtered through 250 µm filter and spun down in growth media. HLOs were washed twice with ice-cold 1□ PBS, and the pellet was then resuspended in 1 mL Geltrex. About 10 µL Geltrex-HLO drops were transferred to each well of 96-well plate and incubated for 15 minutes in the water-jacket incubator to solidify the Geltrex. Once solidified, HLOs were overlaid with 200 µL of HCM and placed back in the incubator for 24 hours.

3.5.2 CYP3A4 induction

CYP3A4 enzyme activity was determined by measuring the oxidation of Troglitazone (TGZ) and rifampicin after 24, 48 and 72 hours of treatment with solvent vehicle control (0.05% DMSO). After treatment, the HCM was removed from each well and HLOs were washed twice with ice-cold 1□ PBS. 50 µL of 50 µM P45-Glo™ CYP3A4 (5 mM luciferin-BE) dissolved in media (either Advanced DMEM/F12 or Full HCM) was added to each well (untreated, treated and media only controls). HLOs and luciferin (luciferinH and luciferin-BE) mixtures were incubated in 37°C in a 5% CO_2 water-jacket incubator for 4 hours. After incubation, supernatants (25 µL) were transferred to clean white walled clear bottom plates and mixed with 25 µL of luciferin detection reagent (reconstitution buffer with luciferase detection reagent). The plate containing HLOs

was used to perform cell viability assays (described in 2.2.1.3). The white clear walled plate was then incubated at 37°C in a 5% CO_2 water-jacket incubator for 30 minutes. Th plate was read using a GLOMAX™ 96 Microplate Luminometer (Promega).

3.6 Cell viability & cytotoxicity assays

3.6.1 Cell viability determination using CellTiter-GLO® 3D Cell Viability Assay

For seeding strategy, see 3.5.1. Briefly, HLOs were either left untreated, treated with DMSO (0.05%), treated with 1% Triton™ X-100, spontaneous control with H_2O and 1% lysis buffer or treated with ART (Table 6), RIF and Triton X-100 for 24 hours. 100 µL supernatant from each respective well was transferred to a new 96 well plate. A CellTiter-GLO® reagent (100 µL) was added to each well containing the HLOs and 100 µL HCM. Contents were mixed vigorously for 5 minutes at RT to induce lysis. The plate was incubated at RT for 25 minutes to stabilize the luminescent signal. Th plate was read using a GLOMAX™ 96 Microplate Luminometer (Promega).

Table 5. Drugs and pathogen treatment groups

Combination Groups	HLO (Media = HCM)
Control 1	Media
ART	7.39 µM EFV, 27.01 µM 3TC & 34.2 µM TDF
ART + ant-TB (A+TB)	7.39 µM EFV, 27.01 µM 3TC & 34.2 µM TDF + 28.42 µM RIF and 20.04 µM INH
SEA	20 µg/ml
TGZ	50 µM

*All drugs were added to cells from 10mM working stocks

3.7 Discovery mass spectrometry analysis

3.7.1 Plating

Briefly, HLO were isolated from a 24-well plate and resuspended in HCM with 10% Geltrex, left overnight in a new 24-well plate in the water-jacket incubator at 37°C. HLO were left untreated or treated with ART, ART + ATB and TGZ (Table 5) for 24 hours and 7 days respectively.

3.7.2 Protein extraction and quantification

Isolated drug treated and untreated HLOs were first incubated with TrypLE™ in water jacketed incubator (37ºC, 5% CO_2) for 3 min. Subsequently, TrypLE™ reaction was diluted with fresh HCM. HLO were spun down at 1800 rpm for 3 min at 4ºC. Supernatant was discarded and pellet retained. Pelleted cells were washed seven times with ice-cold 1□ PBS to remove Geltrex. Proteins were extracted by the addition of 4% sodium dodecyl sulphate (SDS; Sigma Aldrich; catalogue # 71736), 100 mM triethylammonium bicarbonate (TEAB; Sigma Aldrich; catalogue # T7408) and heating at 95˚C for 10 min. Quantification was conducted using the BCA assay (ThermoFisher Scientific; catalogue # 23225) according to the manufacturer's instructions.

3.7.3 HILIC on-bead digest

In preparation for the HILIC magnetic bead workflow, the HILIC beads (ReSyn Biosciences, HLC010) were aliquoted into a new tube and the shipping solution removed. Beads were then washed with 250 µL wash buffer (15% ACN, 100 mM ammonium acetate (Sigma 14267) pH 4.5) for one minute. This was repeated once for a total of two washes. The beads were then resuspended in loading buffer (30% ACN, 200 mM ammonium acetate, pH 4.5) to a concentration of 2.5 mg/mL. A total of 20 µg from each sample was transferred to a protein LoBind plate (Merck, 0030504.100). Protein was reduced and alkylated by addition of 20 mM dithiothreitol (DTT; Sigma D9779) and 30 mM iodoacetamide (IAA; Sigma I6125)) at an equal volume to that of the sample, followed by incubation at 95˚C for 10 minutes. HILIC magnetic beads were added at an equal volume to that of the sample and a ratio of 5:1 total protein. The plate was then incubated at room temperature on the shaker at 900 RPM for 30 minutes for binding of proteins to the beads. After binding, the beads were washed four times with 500 µL of 95% ACN for one minute. For digestion, Trypsin (Promega PRV5111), made up in 50 mM TEAB was added at a ratio of 1:20 total protein and LysC (Pierce 90307) was added at a ratio of 1:250 total protein. The plate was incubated at 45˚C on the shaker for two hours. After digestion, the supernatant containing peptides was removed and dried down. Samples were then resuspended in LC loading buffer: 0.1% FA, 2.5% ACN.

3.7.4 Liquid chromatography and mass spectrometry (LC-MS) proteomics analysis

Liquid chromatography and mass spectrometry (LC-MS analysis was conducted with a timsTOF Pro 2 mass spectrometer (Bruker, USA) integrating trapped ion mobility (IM) separations coupled online via a Captivespray electrospray source (Bruker) to an Evosep One LC system (Evosep Biosystems, Denmark). Peptides were separated on a PepSep C18 column (150µm × 8 cm, 1.5µm - Bruker, 1893470) maintained at 40°C. Separation was achieved using a pre-formed linear gradient of solvents A and B (A: 0.1% FA; B: 100% ACN/0.1% FA) over a 21-minute gradient (the standard 60SPD Evosep One method). The mass spectrometer was operated in positive ion mode. MS data was acquired using the standard “DIA PASEF- short gradient” DIA acquisition method (25 Da mass windows, 21 mass steps per cycle, 0.85 to 1.30 V-s/cm2 CCS window, 100 ms TIMS window) precursor scans ranged from m/z 100 to 1700 and 475 to 1000 for MS/MS. The method duty cycle is estimated to be 0.95s.

3.7.5 MS/MS data analysis

Data analysis was conducted using the directDIA™ (deep) analysis workflow in Spectronaut (version 18) software using a human canonical reference proteome database downloaded from UniprotKB (downloaded on 19/04/2021). All processing parameters were kept as standard unless otherwise stated. The enzymes for digest were set as trypsin/P and LysC/P. The variable modifications were set as acetylation of the N-terminus of the protein, deamidation of glutamine and asparagine and oxidation of methionine. A maximum number of 5 variable modifications were allowed. A fixed modification (carbamidomethyl) was added for alkylation of cysteine (C) by iodoacetamide (composition C (2)H(3) NO with a mass of 57.021464 Da.

3.7.8 Protein quantification and statistical analysis

Statistical testing and relative quantification of proteins were performed using Perseus software (version 2.0.11.0). Principal component analysis (PCA), volcano plots, and the hierarchical clustering were performed using Perseus software. The “All valid proteins” file produced by Spectronaut (version 18) software was further analyzed in Perseus. Protein analysis was performed based on a mixed linear effects model to calculate fold changes and *p*-values. Identified protein groups containing non-valid values were filtered out to obtain a protein data set present in all samples. Means and

standard deviations were calculated from remaining data and groups were annotated accordingly. Relative quantification of proteins was carried out and differential abundance was defined using student *t*-test measuring differences in the log2 fold change of protein expression between experimental group samples (ART-HLO, A+TB-HLO and TGZHLO) compared to control (UN-HLO) group. *P*-values were adjusted among all the proteins in the specific comparison using widely known approach by Benjamini and Hochberg (B-H) and a *p*-value of 0.05 was applied as cut off. The result of the latter *t*-test is shown in the volcano plots. Proteins identified with statistically different abundances between (ART-HLO, A+TB-HLO and TGZ-HLO) and control (UN-HLO) groups were taken further in Perseus for z-scoring of the LFQ intensities and hierarchical clustering, resulting in the heat maps presented.

3.8 Data Availability

The mass spectrometry proteomics data generated and analysed in the current study have been deposited to the ProteomeXchange consortium via the PRIDE partner repository with the dataset identifier PDX061061.

3.9 Statistical analysis

Statistical analyses were performed using GraphPad Prism 5 (GraphPad Software Inc. (San Diego, CA, USA). Data was presented as the mean +/- standard deviation (SD). Statistical significance was determined by Student's *t*-test or One-Way analysis of variance (ANOVA) with Dunnett's post-test where appropriate. A $p<0.05$ is represented by a single asterisk, $p<0.01$ is represented by a double asterisk, three asterisks indicate $p<0.001$, while four asterisks indicate p-value <0.0001.

Chapter 4: Generation and characterization of 3D multicellular human liver organoids (HLO) from iPSCs

4.1 Generation of 3D multicellular human liver organoids (HLO) from iPSCs

To develop and generate 3D multicellular human liver organoids (HLOs) from iPSCs, we first adopted a previously described protocol [11]. Briefly, iPSCs were cultured for 24 hours where we observed a rapid aggregation of iPSCs upon seeding, yielding aggregates with an average diameter of 100 ± 41 µm, which robustly expressed pluripotency markers *OCT-4, Nanog*, and *Sox2* (*Figure 5C*). To initiate the developmental programme, aggregates were differentiated into DE cells using RPMI1640 GlutaMAX medium supplemented with 100 ng/mL Activin A and 20 ng/mL BMP4 coupled with 0% KSR at day 1, 0,2% KSR at day 2 and 2% KSR at day 3 for a period of 3 days with daily media change, respectively (*Figure 5 A-D*). At day 3 of differentiation, DE cells exhibited high expression levels of DE marker *SOX17* (*Figure 5D*) and expression of pluripotency markers was significantly reduced (*Figure 5C*). We further observed a drastic change in cell morphology where iPSCs lost their bright compact colonies, with distinct cell borders and high nucleus (*Figure 5B*). These iPSCs conformed to highly proliferative cells with extensive cellular migration and took a typical-petal or cobbler cell morphology representative of DE cells (*Figure 5B*).

DE cells were challenged with a pulse of WNT signalling via CHIR99021 and FGF-4 to transition into foregut spheroid cells (FGS) for 3 days. On day 7, FGS cells were dissociated with Accutase solution and embedded in Geltrex matrix and resuspended in retinoic acid (RA) medium. RA is known to allow the specification of both parenchymal and non-parenchymal cells [11]. Subsequently, FGS cells were then further subjected to hepatocytes maturation medium supplemented with 10 ng/mL HGF, 20 ng/mL OSM and 0,1 µM Dex, which are known to improve hepatocyte differentiation and maturation until day 21 (*Figure 5 A-D*). Alternatively, FGS can be dissociated into single cells using Accutase solution following 3 min incubation at 37°C and then expanded in organoid formation medium composed of 5 growth factors, including 50 ng/mL VEGF, 20 ng/mL FGF-2, 3 µm CHIR99021 (Glycogen synthase kinase 3 inhibitor), 20 ng/mL EGF, and 5 µM A83-01 (Transforming growth factor-β inhibitor) before RA treatment and further cell differentiation.

4.2 Assessing presence of pro-fibrotic and inflammatory cell lineages in HLOs.

Alongside parenchymal cells, the human liver is comprised of non-parenchymal cell types including profibrotic stellate cells, tissue resident macrophages (Kupffer cells) and liver endothelial sinusoidal cells. To examine the presence of parenchymal and the non-parenchymal cells/supportive/stromal lineages, we performed flow cytometry analysis (*Figure 6*) with epithelial cells marker EpCAM, stellate cells marker CD166/ALCAM and liver tissue resident macrophages marker CD68. The frequency of EpCAM+ positive cells observed in HLO was 60,4% while EpCAM- negative cells was 39,5% (*Figure 6A*). The frequencies of supportive lineages observed for EpCAM/CD166/ALCAM+ and EpCAM-/CD68+ cells were 11% and 5%, respectively (*Figure 6B-C*). Together, these results proved that multiple cell types exist in HLOs, and their frequencies are consistent with those found in the native liver organ.

4.3 Functional hepatic profiling of multicellular HLOs derived from iPSCs.

The organoids exhibit mature hepatic transcriptional signature, and profiles as well as a liver cellular repertoire [10,120]. The liver has a myriad of functions including the ability to metabolize drugs via CYP450 enzymes family including CYP3A4, 1A2, 2A6, and 2E1 [121]. CYP450 undergoes a sequential upregulation of different isotypes during the process of liver maturation [120,121]. CYP1A2 represents the predominant subtype during organogenesis, followed by increased CYP2E1 levels during the second trimester foetal stage. In infants, CYP3A7 is the predominant subtype and CYP3A4 becomes the predominant subtype in adult liver [10,11,121]. Several *in vitro* studies investigating liver stem cells or organoid maturation utilize *CYP3A4 expression* as a proxy for liver differentiation and maturation. Thus, to profile the hepatic lineage in HLOs, we utilized RT-qPCR to examine the gene expression of stage-specific markers from iPSCs to HLO (*Figure 5 C-D*).

The mRNA expression levels of *HNF4α* and *CYP3A4* were significantly upregulated in FGS relative to iPSCs and DE cells, which indicated an early hepatic commitment. Furthermore, we observed a robust mRNA expression level of the specific mature hepatocyte's markers in ALB, HNF4α, ATA1, and CYP3A4 at day 21 of differentiation coinciding with decreased expression of pluripotency and DE markers (*Figure 5C-D*). (*Figure 5B*) The observed change in transcriptional signature shown by reduction of

DE genes from day 7-21 and notable reduction in pluripotency genes at day 3-21 was corroborated by change in the cell morphology (*Figure 5B*). Moreover, robust gene expression levels of specific mature hepatic markers genes such as ALB and ATA1 as well as those involved in metabolism of xenobiotic drugs such as cytochrome P450 *(CYP3A4)* at 21 suggested that HLOs contain mature hepatocytes (*Figure 5D*). Collectively, the differentiation process of HLOs resulted in increased expression of metabolic markers consistent with liver maturation.

To validate whether the HLOs can be used within *in vitro* trial setting and disease model, we first exposed established HLOs to doses of different drugs including ART, a combination of drugs given to HIV-positive patients; RIF, which is part of the first line anti-TB drug regimen; and Triton X-100, membrane permeabilizer for 24 hours (*Figure 7*) and cell viability assay was carried out using Cell-Titre 3D GLO cell viability assay [10]. Treatment with ART or Triton X-100 significantly altered HLOs integrity and morphology compared to the untreated (UN) counterparts (*Figure 7A*). In contrast, treatment with RIF did not alter HLOs morphology (*Figure 7A).* Furthermore, HLO's treated with ART or Triton X-10 exhibited a significant reduction in cell viability while RIF did not have any effect on cell viability (*Figure 7B*). Taken together, these findings showed the capacity of HLO's to respond to drugs and indicated that they can be used for further downstream assays.

To demonstrate the metabolic capacity and activity of HLOs, we incubated the HLOs with ART, A+TB and TGZ for 72 hours. The basal and inducible CYP3A4 activity of HLOs was benchmarked against differentiated HepaRG cells (*Figure 7),* which are a widely used cell line [27]. HepaRG cells are preferred over PHH due to their accessibility and ease to work [26]. Based on the luminescent readouts, HLOs showed significantly increased CYP3A4 activity for both basal and inducible metabolism posttreatment with ART and A+TB compared to 3D culture of differentiated HepaRG cells (*Figure 7C*). However, the CYP3A4 activity between TGZ-treated HLOs and the 3D HepaRG cells was comparable and insignificant relative to UN controls (*Figure 7C*). These findings showed high CYP3A4 induction in HLOs compared to HepaRG cells post-treatment with drugs. Collectively, these results showed high sensitivity, capacity and the superiority of HLOs in drug metabolism compared to 3D HepaRG model.

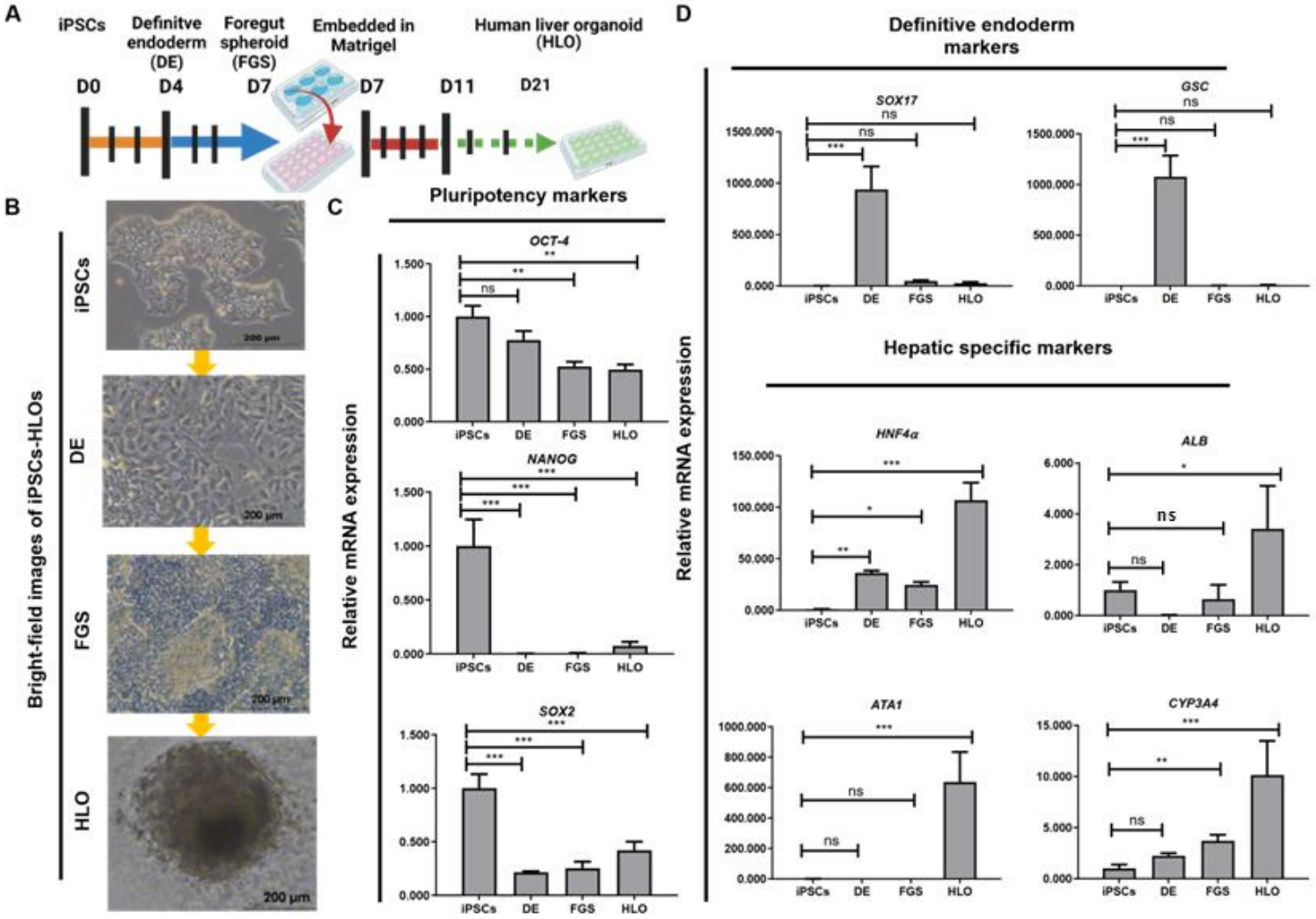
A
iPSCs
Definitve endoderm (DE)
Foregut spheroid (FGS)
Embedded in Matrigel
Human liver organoid (HLO)
D0
D4
D7
D7
D11
D21
B
Bright-field images of iPSCs-HLOs
iPSCs
DE
FGS
HLO
200 µm
C
Pluripotency markers
Relative mRNA expression
OCT-4
NANOG
SOX2
iPSCs
DE
FGS
HLO
D
Definitive endoderm markers
SOX17
GSC
Hepatic specific markers
HNF4α
ALB
ATA1
CYP3A4
Relative mRNA expression
ns

Figure 5. Generations of 3D multicellular human liver organoids derived from induced pluripotent stem cells.

(A) Schematic overview of the differentiation method for liver organoids.1.5X10^6 iPSCs were cultivated in 6-well plates, for 24 hours in E8M. After 24 hours, cultivated iPSCs were further differentiated into DE cells (day 1-3), FGS cells (day 4-6) and HLO (day 7-21). At day 7, FGS cells were rinsed with DPBS, followed by embedding them in 100% Geltrex matrix to form a 3D scaffold. From differentiation day 1-6, media change occurred every 24 hours, day 7-11 media change occurred every 48 hours while from day 11-21 media was changed every 72 hours. At each differentiation stage, iPSCs, DE, FGS, and HLO, cells were rinsed with DPBS, followed by RNA extraction for cDNA synthesis and qPCR to confirm specific stage gene markers for iPSCs (OCT-4, Nanog, and Sox2), DE (SOX17 and GSC), mature specific hepatic markers (HNF4α, ALB, ATA1 and CYP3A4). (B) Phase-contrast images of iPSCs-HLO depicting change in cell morphology 100 µm. (C) Reverse transcription qPCR analysis of represented genes related to pluripotency or undifferentiated state, (D) DE state and hepatic function, respectively. Undifferentiated iPSCs (iPSCs, n=3), DE (n=3), posterior foregut spheroid (foregut, n=3) and HLO (n=3). mRNA expression levels of our genes of interest were normalised to the house keeping gene GAPDH. Data sets are presented as mean +/- SEM (n=3) and analysed by Student t tests, and one-way analysis of variance (ANOVA) using Dunnett's multiple of comparison as a post-hoc test (Ns-non-significant, p<0.05, p<0.001**, and p<0.0001***).*

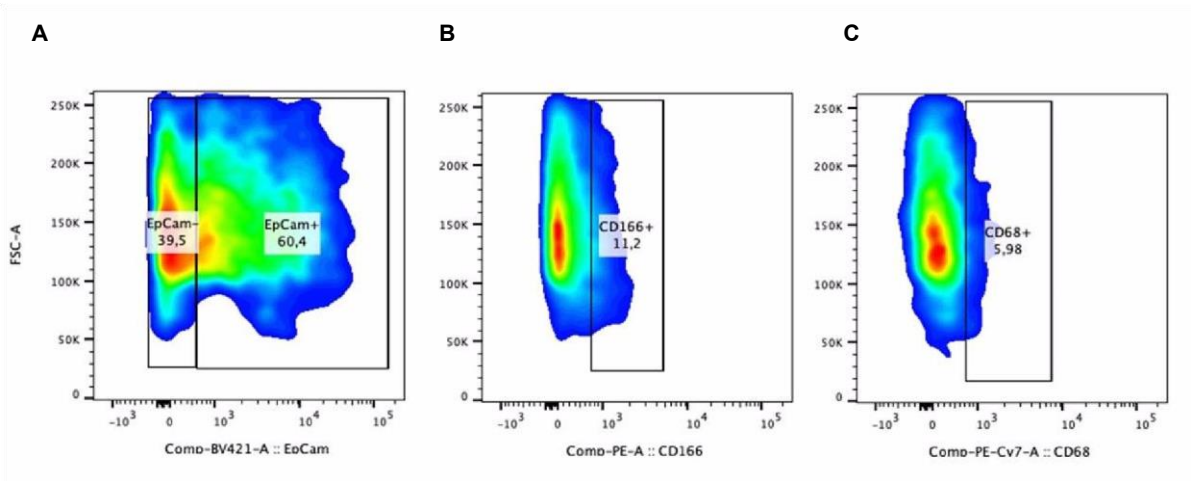

Figure 6. FACS analysis of the expression of surface proteins present on HLO differentiated from iPSCs.

HLO were examined for the co-expression of EpCAM+, CD166+ and CD68+ cells. Briefly, HLO were rinsed with DBPS, followed by dissociation into single organoids using the TrypLE express solution. Subsequently, dissociated HLO were incubated with FACS buffer solution containing EpCAM (1:80), CD166 (1:160) and CD68 (1:80) antibodies. The y-axis represents forward scatter (FSC-A), where an increased signal indicates the frequency of cells in HLO. The x-axis indicates the GFP Fluorescence. The black lines are included to guide the eye to distinguish the fluorescence frequencies between EpCAM- cells and EpCAM+, CD166+ and CD68+ stained cells present in our HLO. (A) Percentage of EpCAM+ stained cells, (B) Indicate percentage of CD166+ stained cells and (C) Shows CD68+ stained cells of the whole organoids cell population after 21 days of HLO culture. EpCAM+ cells (60,4%), CD166+ (11,2%) and CD68+ (5.98%), respectively.

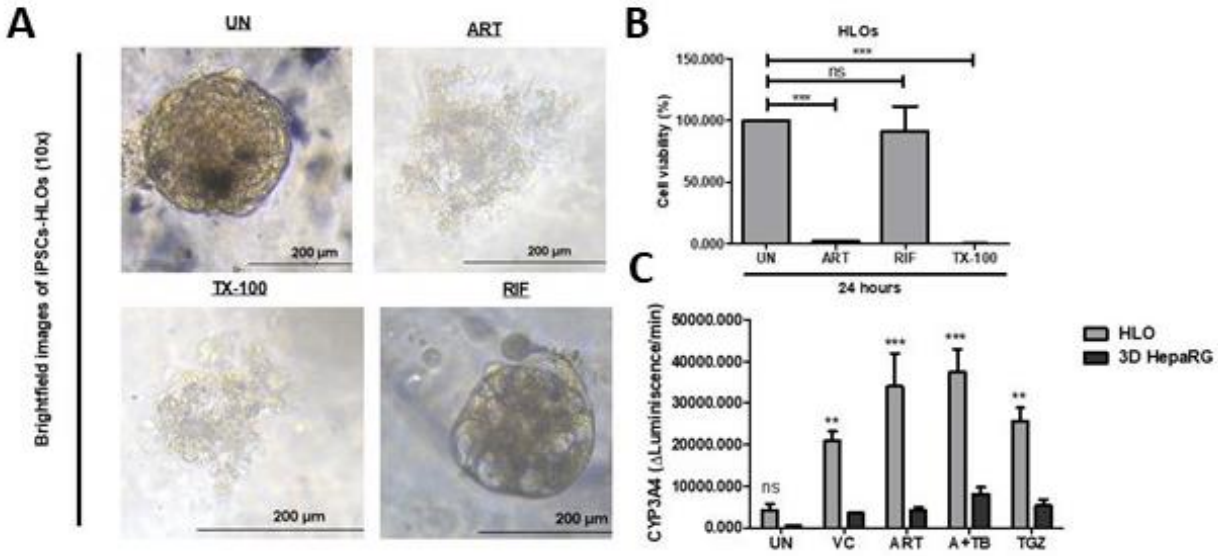

Figure 7. Cell viability of HLO & CYP3A4 enzyme activity.

HLO were rinsed with DBPS, followed by dissociation into single organoids using the TrypLE express solution. Subsequently, dissociated HLO were embedded in Geltrex and cultivated in 96 well sphere U bottom plates for 24 hours. HLO were further incubated with media only (UN), ART, Rifampicin (50 µM), and 1% Triton X-100 (TX100) to determine cell viability using 3D GLO cell viability assay and CYP3A4 activity using the CYP3A4 GLO assay. (A) HLO Phase contrast images of different treatment groups, Untreated (UN), ART, rifampicin (RIF), TX-100 (Triton x-100). (B) Cell viability percentages. (C) CYP3A4 enzyme activity in Untreated HLO, VC, ART and A+TB treated HLO and 3D HepaRG model post 72-hour treatment. Data are presented as mean +/- SEM (n=3) and were analysed by one-way analysis of variance (ANOVA) using Dunnett's multiple of comparison as a post-hoc test. Ns-non-significant, p<0.05, p<0.001**, and p<0.0001***.*

4.4 Assessing drugs and antigen-induced inflammatory profile in HLOs.

Excessive alcohol consumption, increased drug intake, high fat diet and disease-causing pathogens drive liver inflammation in humans [10]. To carefully examine the inflammatory response in HLOs post-treatment with ART and A+TB for 24 hours or *Schistosoma mansoni soluble egg antigen* (*SEA*) for 7 days (*Figure 8A*), we used ELISA to detect the levels of inflammatory mediators present in the supernatants of treated HLOs. IL-6 levels were significantly increased in ART, A+TB and SEA-treated HLOs (*Figure 8B*), while IL-1β was significantly increased in A+TB treated HLOs

(Figure 8C). Interestingly, the TNF-α levels were significantly increased in ART and A+TB treated-HLOs compared to UN HLOs (*Figure 8D*).

SEA modulate the immune response by promoting tolerogenic dendritic cells (DCs) and alternatively activated (M2) macrophages, which in turn induce regulatory B cells and T helper 2 cells mediated responses, while simultaneously inhibiting the proinflammatory response of Th1 and Th17 cells [122]. We observed significantly increased levels of IL-4 in SEA-treated HLO compared to UN HLOs (*Figure 8E*). Of note*,* anti-inflammatory mediator IL-10 levels were remarkedly elevated in ART and ART+TB treated-HLO and SEA treated-HLO compared to UN HLO (*Figure 8F*). There was no difference in the levels of IL-1β between ART and SEA-treated HLO and IL-4 levels between ART and A+TB treated HLO compared to HLO (*Figure 8C-F*). Therefore, these results demonstrate that HLOs could be used to fully understand the inflammatory responses exerted by drugs and pathogens during hepatic injury.

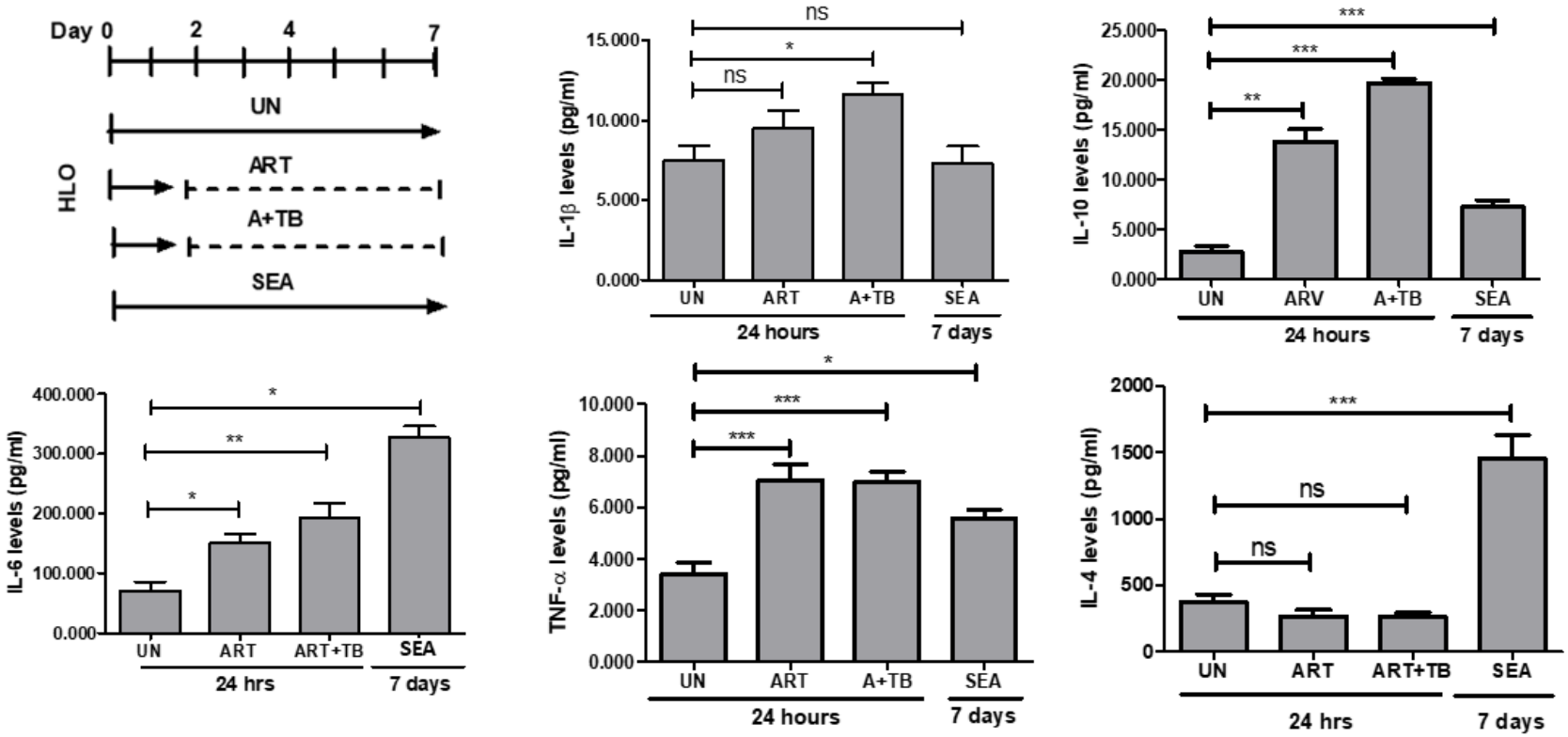

Figure 8. The levels of proinflammatory and anti-inflammatory response after drugs treatment and pathogen infection in HLO.

HLO were rinsed with DBPS, followed by dissociation into single organoids using the TrypLE express solution. Subsequently, dissociated HLO were embedded in Geltrex and cultivated in 96 well sphere U bottom plates for 24 hours. HLO were incubated with media only, ART & A+TB for 24 hours and SEA for 7 days. After each incubation time or treatment period, supernatants were aspirated and aliquoted onto the wells of a corresponding 96 well plate. Supernatants were used to carry out ELISA assay using BD Bioscience ELISA kit according manufacturer's protocol. (A) Schematic diagram showing treatment duration for ART, A+TB and SEA induced liver injury. (B) Indicate the levels proinflammatory mediators IL-6, (C) IL-1β, and (D) IL-4 in ART, A+TB post 24 hours and SEA post 7 days compared to UN counterpart. (D) Indicate the levels of the pathological mediator (E) TNF-α and (F) the anti-inflammatory mediator IL-10 compared to UN group, respectively. Data are presented as mean +/- SEM (n=7) and analysed by one-way analysis of variance (ANOVA) using Dunnett's multiple of comparison as a post-hoc test. $p>0.05^{ns}$, $p<0.05$, $p<0.001$**, and $p<0.0001$***.*

Chapter 5: Generation of HLO and validation discussion

The development of relevant *in vitro* hepatic models that recapitulate functional human liver characteristics have remained elusive. The advances in stem cell research and the discovery of iPSCs-derived hepatic organoids have opened new possibilities for their application as models for drug testing and disease modelling. Researchers have made efforts to produce large amounts of scalable human liver organoids, for example, Mun and colleagues generated expandable human iPSCs derived-liver organoids over a period of 22 days in culture [10], while others have generated organoids using LGR5+ adult stem cells [1,123]. These researchers produced organoids composed exclusively of hepatocytes for transplantation purposes and drug testing [10,30,51]. However, the lack of liver cell types such as stellate cells and hepatic residence macrophages, which are involved in maintaining hepatic tissue homeostasis [1,12], limits their utility for modelling inflammatory conditions. Hepatocytes and stellate cells co-cultures using the 3D organoid models to study fibrosis phenotypes post cytokine-mediated direct activation of stellate cells have been established [16,124]; although these models fail to faithfully recapitulate more context-dependent fibrotic phenotype such as NASH.

The primary aim of the present study was to develop a robust and tractable 3D human liver organoid model derived from iPSCs to model drug & pathogen induced liver injury. Herein this thesis, we presented a protocol adapted from Ouchi and colleagues to generate HLOs from iPSCs [11]. The protocol followed a liver-like developmental route, producing HLOs comprising a liver-like cellular repertoire including the parenchymal hepatocytes and non-parenchymal/stromal cell types such stellate cells and Kupffer cells. To confirm differentiation of iPSCs to HLOs, we observed a significant reduction in the pluripotency and DE markers. iPSCs subjected to HLO differentiation lost their cell morphology and became highly proliferative cells with extensive cellular migration, thus taking a typical-petal or cobbler cell morphology.

The liver is a very complex endocrine organ with specific architecture, organization, and functions “including lipids and ammonium metabolism, bile, and the coagulation production, and the detoxification of exogenous compounds”, which are correlated to the cell types that populate it [125]. Flow cytometry analysis after staining HLO with specific antibodies to surface cell markers revealed that HLO comprised of hepatocytes, profibrotic stellate cells, and resident macrophages. The observed frequency of these cellular populations in HLOs were corroborated by those reported in an earlier study [11]. Furthermore, based on functional assays, CYP3A4 activity was robustly increased in HLOs post 72-hour incubation with ART, A+TB and TGZ drugs compared to the 3D HepaRG model. Collectively, these observations highlighted that HLOs are sensitive and superior to 3D HepaRG model.

In the present study, we did not compare CYP3A4 activity of HLOs to that of the PHH, which serve as the gold standard for drug testing and hepatocyte functional assays [1,2,10,49]. Previous studies have shown that iPSCs-derived liver organoid exhibit less albumin production and CYP3A4 activity relative to PHH [10,120]. On the contrary, observations from a recent study showed that ALB secretion capacity of HLOs and PHH were not statistically different [120]. Even though ALB secretions levels in HLOs and PHH were comparable, gene expression of ALB in both were significantly different, owing to the difference in cell composition between HLOs and PHH [120]. Therefore, this calls for optimization of the current HLOs to incorporate more cells and improve differentiation cues that could induce mature transcriptional and proteomic signature like PHH.

The differential and functional characterization of HLOs was based solely on the expression of mature specific hepatocyte markers, *HNF4α, ALB, CYP3A4* and *ATA1*, and functional assays such as CYP3A4 activity. However, the functional characterization of HLOs can be improved by including assays specific to hepatocytes. These assays would include bile production [121], glycogen storage [10], visualization of the biliary tree/bile canaliculi network [120], as well as conversion of ammonia to urea. Moreover, hepatocyte zonation in HLO could also be assessed.

With respect to disease modelling and normal cellular processes, an area of research we are currently pursuing is the utility of HLOs to model DILI and pathogen-induced fibrosis/liver injury. We explored the capacity of HLOs in mimicking diverse phenotypes of DILI and pathogen-induced fibrosis by exposing them to (i) ART alone, (ii) A+TB and (iii) *SEA*. HLOs faithfully mimicked ART, A+TB and the pathogen-induced immune response as demonstrated by increased levels of pro-inflammatory cytokines (IL-6, IL-1β and IL-4), the pathological mediator TNF-α and IL-10 in drug treated HLO compared to untreated group. Therefore, HLOs may be amenable to model acute and chronic inflammatory disease.

Chapter 6: Quantitative proteomic analysis of differentially expressed proteins.

To quantitatively analyse differentially expressed proteins in HLO, day 23 HLO were harvested from 24-well plates and resuspended in HCM with 10% Geltrex matrix, were left overnight in a new 24-well plate in water jacketed incubator at 37°C. Subsequently, HLO were left untreated (UN-HLO) or treated with ART, A+TB and TGZ (Table 5) for 72 hours, respectively. Post 72 hours, drug treated and untreated HLO were pelleted and washed thoroughly with ice-cold PBS, pelleted and prepared for Mass Spectrometry acquisition (*Figure 9*) at D-CYPHR unit based at the University of Cape Town. Prior to mass spectrometry acquisition, HLO proteins were extracted by addition of 4% sodium dodecyl sulphate (SDS), 100 nM triethylammonium bicarbonate and heating at 95˚C for 10 min. BCA assay was used to quantify the protein concentrations. Discovery proteomics was conducted on 28 (7 UN-HLO, 7 ART-HLO, 7 A+TB-HLO and 7 TGZ-HLO) biological replicate samples.

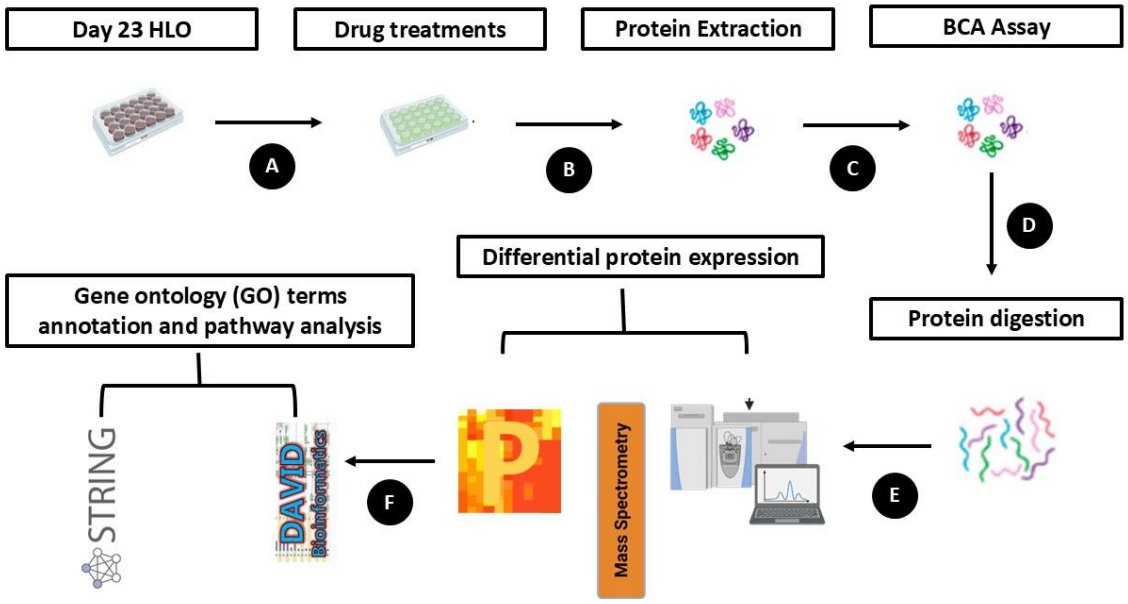

Figure 9. Proteomic experimental workflow and data analysis

Workflow chart from organoid harvesting at day 23, (A) drug treatments, (B) protein extraction, (C) protein quantification, (D), peptide formation, (E) mass spectrometry acquisition & proteomic analysis, (F) gene ontology terms annotation and pathway analysis.

6.1.1 Comparative proteomic analysis of drug treated HLO vs untreated HLO

A comparative proteomic analysis was carried out to identify differentially expressed proteins between drug treated-HLO vs untreated-HLO (*Figure 9*, *Table 5*). An output file from D-CYPHR consisting of 2006 identified and quantified proteins (*Table S1*) was utilized to perform downstream analysis using Perseus software. Proteins with 80% minimum valid values in at least one group were considered valid and were quantified by LFQ and log-transformed into relative expression data across all experimental groups resulting in expression profiles of 1964 proteins (Data sheet 1). We further performed Benjamin-Hochberg (B-H) multiple sample correction test to identify significantly differentially expressed proteins (DEPs). 112 identified proteins were significantly differentially expressed between the groups. 112 identified proteins were significantly differentially expressed. PCA plot displayed a distinct clustering among ART-HLO, A+TB-HLO and TGZ-HLO vs UN-HLO (Data sheet 1, *Figure 10A*). Interestingly, ART-HLO clustered with A+TB-HLO as depicted by the encircled protein groups on the PCA plot (*Figure 10A*).

To get an overview, we performed an unsupervised hierarchical clustering of DEPs across all treated-HLO and UN-HLO (*Figure 10B*). Global proteome revealed a clear separation of treated-HLO from UN-HLO based on proteomic profiles depicted by the unsupervised hierarchical clustering heatmap (ANOVA, FDR ≤ 0.05) in Perseus software. Overall, this data depicted a clear distinction in proteomic profile between treated-HLO's vs UN-HLO. Furthermore, it demonstrated that ART-HLO and A+TB-HLO share or have similar proteomes.

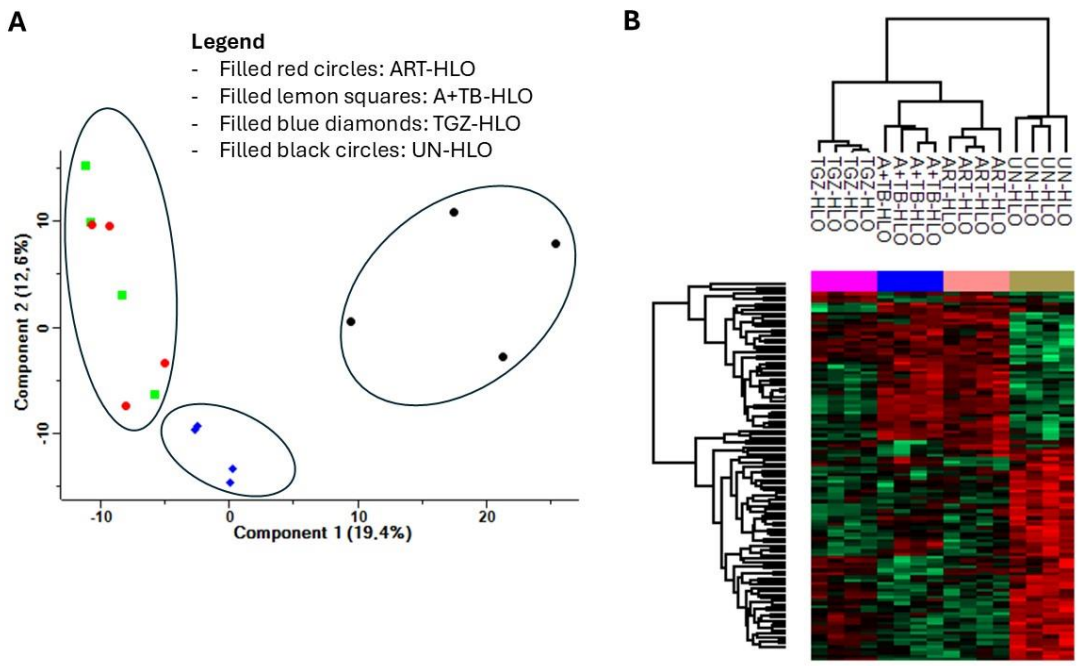

Figure 10. Comparative proteomic analysis of drug treated HLO vs untreated-HLO proteome.

(A) Principal Component Analysis (PCA) analysis of protein expression among ART-HLO, A+TB-HLO, TGZ-HLO vs UN-HLO. (B) Protein heatmap based on unsupervised hierarchical clustering of all 112 significantly differentially expressed proteins among ART-HLO (n=4), A+TB-HLO (n=4), TGZ-HLO (n=4) and UN-HLO (n=4) in Perseus version 2.0.11 software. The rows are normalized Z-scores (q = 0.05). High abundance proteins are represented in red colour and low abundance proteins are represented in green colour, respectively. Dark-black colour represents missing protein values within the heatmap.

6.1.2 Distinct clustering of ART-HLO compared to UN-HLO proteomes.

A comparative proteomics analysis was carried out between ART-HLO and UN-HLO to investigate molecular mechanisms of ART-induced liver injury. In the present study, a total of 2006 proteins were identified and quantified from D-CYPHR output file (*Table S1*). Proteins with 80% minimum valid values in at least one group were considered valid and were quantified by LFQ and log-transformed into relative expression between ART-HLO and UN-HLO groups resulting in expression profiles of 1851 proteins (*Data sheet 1*). Of these proteins 128 were significantly differentially expressed *(Figure 11B*). Principle component analysis (PCA) showed a clear distinction in clustering between ART-HLO and UN-HLO (*Figure 11A*). Among 128

differentially expressed proteins (DEPs), 65 proteins maintained statistical significance after applying multiple sample testing correction using Benjamin-Hochberg (FDR). Of the 65 proteins, 11 proteins were significantly having high abundance levels and 54 were having low abundance levels in ART-HLO compared with UN-HLO (Data sheet 2, *Figure 11C*).

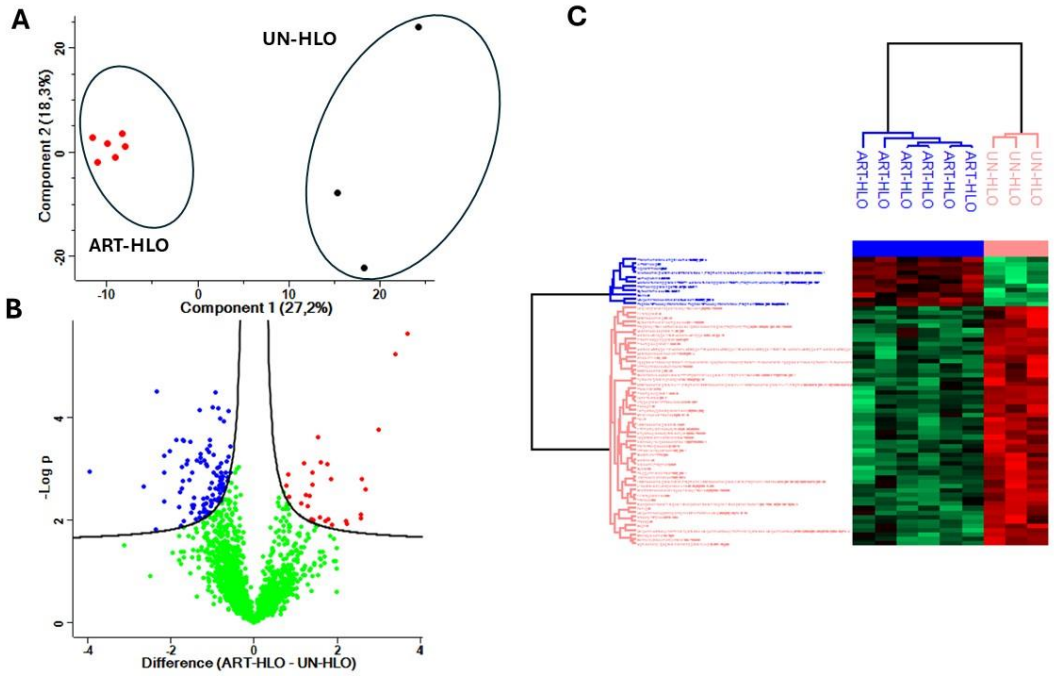

Figure 11. Identification of differentially expressed proteins in ART-HLO compared to UN-HLO controls.

(A) Principal Component Analysis (PCA) analysis of protein expression UN-HLO and ART-HLO. (B) Volcano plots showing significantly high- or low abundance proteins (adjusted p= 0.05) comparing differences in log2 fold changes among x-axis represent protein difference (log2-transformed fold changes) between ART-HLO and UN-HLO protein expression. Statistical significance (-log10 p-value) is indicated on the y-axis. Blue dots represent proteins with negative log2 fold change (higher expression in UNHLO sample groups) and red dots depicts those with positive log2 fold change (higher expression in ART-HLO sample groups). Lemon dots represent non-significant proteins as set by an FDR value of 0.05 and S0 value of 0.05 in Perseus software. (C) Protein heatmap based on unsupervised hierarchical clustering of all significantly differentially expressed proteins between ART-HLO (n=5) and UN-HLO (n= 3) in Perseus software. The rows are normalized Z-scores (q = 0.05). Upregulated proteins

are represented in red colour and downregulated proteins are represented in green colour, respectively. Dark-black colour represents missing protein values within the heatmap.

Top high abundance proteins (*Table 6*) in ART-HLO were involved in the following pathways: (1), innate immunity such as alpha 2 macroglobulin (A2M); (2), vesicular protein trafficking, early secretory pathway which include VIP36-like protein (LMAN2L); (3), regulation of innate immune response such as hemoglobin subunit beta (HBB); (4), proteins involved in oxidative phosphorylation (mitochondrial cytochrome c oxidase subunit 2); and (5), regulation of oxidative stress such as microsomal glutathione S-transferase 1 (MGST1). The top low abundance proteins (*Table 6*) identified were involved in the following pathways: (1), synthesis of proteins such as 40s ribosomal protein S4, X isoform (RPS4X); (2), pre-MRNA splicing including small nuclear ribonucleoprotein Sm D1 (SNRPD1); (3), actin polymerization, gene transcription and repair of damaged DNA such as actin-related protein 2 (ACTR2); (4), transfer of proteins which includes ubiquitin-conjugating enzyme E2 N like (UBE2N); (5), biogenesis of circular RNA such as Interleukin enhancer-binding factor 3 (ILF3); and (6), assembly of respiratory chain and induction of apoptotic cell death (apoptosis-inducing factor 1, mitochondrial [AIFM1]), respectively.

DEPs in ART-HLO compared to UN-HLO were visualized using unsupervised hierarchical clustering to generate a heatmap (ANOVA, FDR≤0.05) in Perseus software. Hierarchical clustering data revealed a clear separation between ART-HLO and UN-HLO (*Figure 10C*). Taken together, these data demonstrated that the ARTHLO's had a distinct proteome to UN-HLO. Finally, the top high abundance proteins in ART-HLOs were associated with immune responses while low abundance proteins were associated with protein synthesis and transport.

Table 6. Top high (A) and low (B) abundance proteins in ART-HLO vs UN-HLO

Protein ID	Description	Gene name	FC	-log (*p*-value)
(A) Upregulated proteins				
P01023	Alpha-2-macroglobulin	A2M	3,407	5,243

Q9H0V9	VIP36-like protein	LMAN2L	3,688	5,634
P10620	Microsomal glutathione S transferase 1	MGST1	2,985	3,759
P00403	Cytochrome c oxidase subunit 2	MT-CO2	2,602	2,795
P68871	Hemoglobin subunit beta	HBB	1,756	3,082
Q16576	Histone-binding protein RBBP7	RBBP7	1,407	2,926
(B) Downregulated proteins				
P62701	40S ribosomal protein S4, X isoform	RPS4X	-0,564	3,432
P62314	Small nuclear ribonucleoprotein Sm D1	SNRPD1	-2,024	3,334
P61088	Ubiquitin-conjugating enzyme E2 N	UBE2N	-2,167	3,261
O95831	Apoptosis-inducing factor 1, mitochondrial	AIFM1	-1,206	3,166
Q12906	Interleukin enhancer-binding factor 3	ILF3	-1,290	3,285
P61160	Actin-related protein 2	ACTR2	-0,728	3,922

6.2 Functional gene ontology (GO) enrichment analysis

For the functional annotation, Database for Annotation, Visualization, and Integrated Discovery (DAVID) v2024q1 online server was used. To ascertain Kyoto Encyclopaedia of Genes and Genomes (KEGG) pathway-enriched genes and the potential gene ontology (GO) classification, terms approximating to the biological process (BP), cellular component (CC) and molecular function (MF) were used. Genes with a *p*-value ≤0,05 and false-discovery rate (FDR) <0,05 were considered strongly enriched.

Based on gene ontology analysis of high abundance proteins in ART-HLO group (*Data sheet 3, Figure 12A*), we found that most of these proteins enriched for BP were insignificantly involved in the acute phase response, mitochondrial electron transport, cytochrome c to oxygen, ATP synthesis coupled electron transport, acute inflammatory response to antigenic stimulus, ER to Golgi vesicle-mediated transport and the negative regulation of complement system, lectin pathway (*Figure 12A*). These

proteins were also localized in the alpha platelet granule lumen, endoplasmic reticulum, Golgi apparatus, histone deacetylation complex, ER to Golgi transport vesicle and the mitochondrial respiration chain complex IV. In terms of their molecular functions (*Figure 12A*), these proteins were closely related to copper ion binding, endopeptidase inhibitor & cytochrome-c oxidase activity, tumour necrosis factor binding, and interleukin 1 and 8 binding activities, respectively.

According to gene ontology BP analysis (*Data sheet 3*, *Figure 12B*), low abundance proteins were mostly enriched for the heterochromatin organization, cytoplasmic translation, translation, nucleosome assembly, and antimicrobial immune response mediated by antimicrobial peptide and innate immune response in mucosa (*Figure 12B*). These proteins were mainly found in the ribosome, cytosolic ribosome, and nucleosome. Most of these proteins are related to nucleosomal DNA binding, cadherin binding, RNA & DNA binding, protein heteromerization activity and the structural constituent of chromatin.

6.3 Functional enrichment pathway analysis

KEGG pathway-based functional enrichment analysis of the differentially expressed proteins revealed that proteins levels that are lowly abundant were significantly enriched in neutrophil extracellular trap formation and alcoholism pathways (*Data sheet 3, Figure 13*). Pathways such as ATP-dependent chromatin remodelling, ribosome, necroptosis, amino acids, and fatty acid degradations were non-significantly enriched (*Figure 13*).

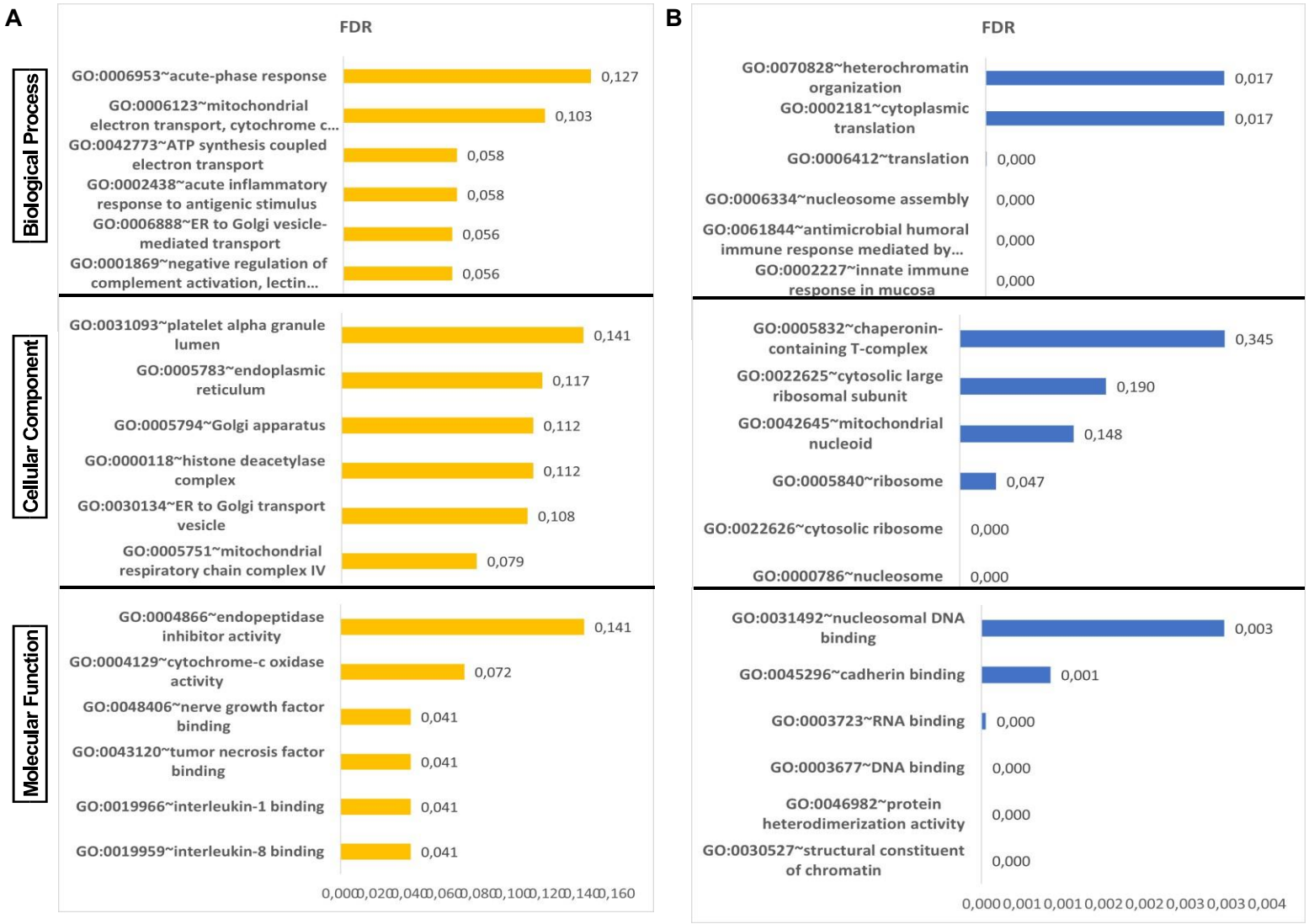
A
B
FDR
Biological Process
GO:0006953~acute-phase response
0,127
GO:0006123~mitochondrial electron transport, cytochrome c...
0,103
GO:0042773~ATP synthesis coupled electron transport
0,058
GO:0002438~acute inflammatory response to antigenic stimulus
0,058
GO:0006888~ER to Golgi vesicle-mediated transport
0,056
GO:0001869~negative regulation of complement activation, lectin...
0,056
Cellular Component
GO:0031093~platelet alpha granule lumen
0,141
GO:0005783~endoplasmic reticulum
0,117
GO:0005794~Golgi apparatus
0,112
GO:0000118~histone deacetylase complex
0,112
GO:0030134~ER to Golgi transport vesicle
0,108
GO:0005751~mitochondrial respiratory chain complex IV
0,079
Molecular Function
GO:0004866~endopeptidase inhibitor activity
0,141
GO:0004129~cytochrome-c oxidase activity
0,072
GO:0048406~nerve growth factor binding
0,041
GO:0043120~tumor necrosis factor binding
0,041
GO:0019966~interleukin-1 binding
0,041
GO:0019959~interleukin-8 binding
0,041
0,000 0,020 0,040 0,060 0,080 0,100 0,120 0,140 0,160
FDR
GO:0070828~heterochromatin organization
0,017
GO:0002181~cytoplasmic translation
0,017
GO:0006412~translation
0,000
GO:0006334~nucleosome assembly
0,000
GO:0061844~antimicrobial humoral immune response mediated by...
0,000
GO:0002227~innate immune response in mucosa
0,000
GO:0005832~chaperonin-containing T-complex
0,345
GO:0022625~cytosolic large ribosomal subunit
0,190
GO:0042645~mitochondrial nucleoid
0,148
GO:0005840~ribosome
0,047
GO:0022626~cytosolic ribosome
0,000
GO:0000786~nucleosome
0,000
GO:0031492~nucleosomal DNA binding
0,003
GO:0045296~cadherin binding
0,001
GO:0003723~RNA binding
0,000
GO:0003677~DNA binding
0,000
GO:0046982~protein heterodimerization activity
0,000
GO:0030527~structural constituent of chromatin
0,000
0,000 0,001 0,001 0,002 0,002 0,003 0,003 0,004

Figure 12. Functional GO enrichment analysis of all differentially expressed proteins.

A combined list of significantly high abundance - and low abundance proteins was used for analysis, and proteins with FDR cut of value <0,05 and p-value ≤0.05 were considered significantly enriched. Enrichment analysis for GO biological process (BP), GO cellular component (CC) and GO molecular function (MF) was performed using DAVID v2024q1. (A) Enriched GO terms for high abundance proteins in ART-HLO (B) Enriched GO terms for low abundance proteins in ART-HLO group. FDR relative to Homo Sapiens proteome is displayed at the x-axis. Enriched terms are displayed on the y axis.

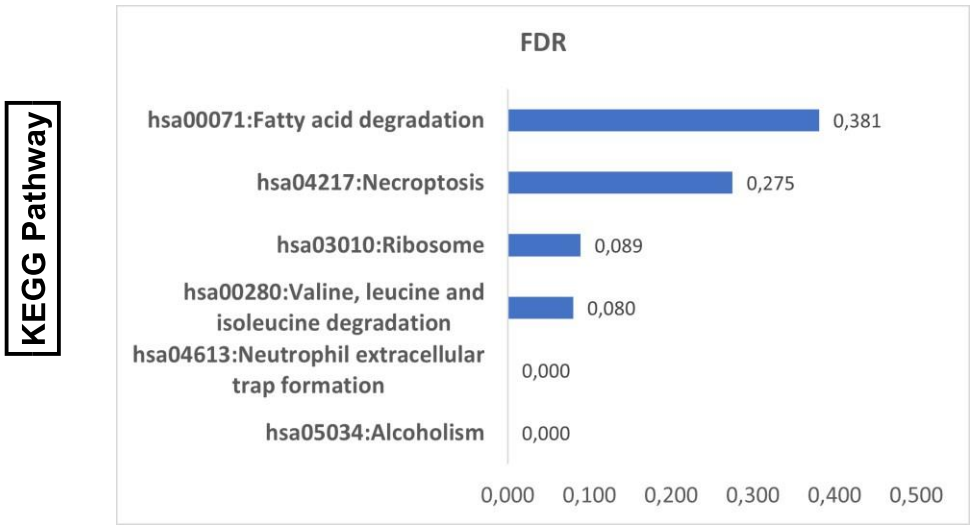

Figure 13. Functional enrichment pathway analysis.

KEGG pathway analysis was performed in DAVID v2024q1, and the generated data was visualized. FDR relative to the Homo Sapiens proteome is displayed at the x-axis. Enriched pathways are displayed on the y-axis. Proteins with FDR cut of value < 0,05 and p value ≤ 0.05 were considered significantly enriched.

6.4 Establishment of protein-protein interaction (PPI) network analysis

To elucidate how ART treatment affects the overall composition of ART-HLO proteomic signature, we performed pathway enrichment analysis of DEPs and putative protein-protein interaction (PPI) network using STRINGDB. PPI network analysis was performed with a minimum required interaction score set to the confidence of 0.4. The

tubular output was generated from STRINGDB tool. A PPI network represented a network with 96 nodes and 269 edges, and a significant PPI enrichment *p*<1.0e-16 (*Figure 14*). The nodes denote the number of proteins whilst edges their interactions.

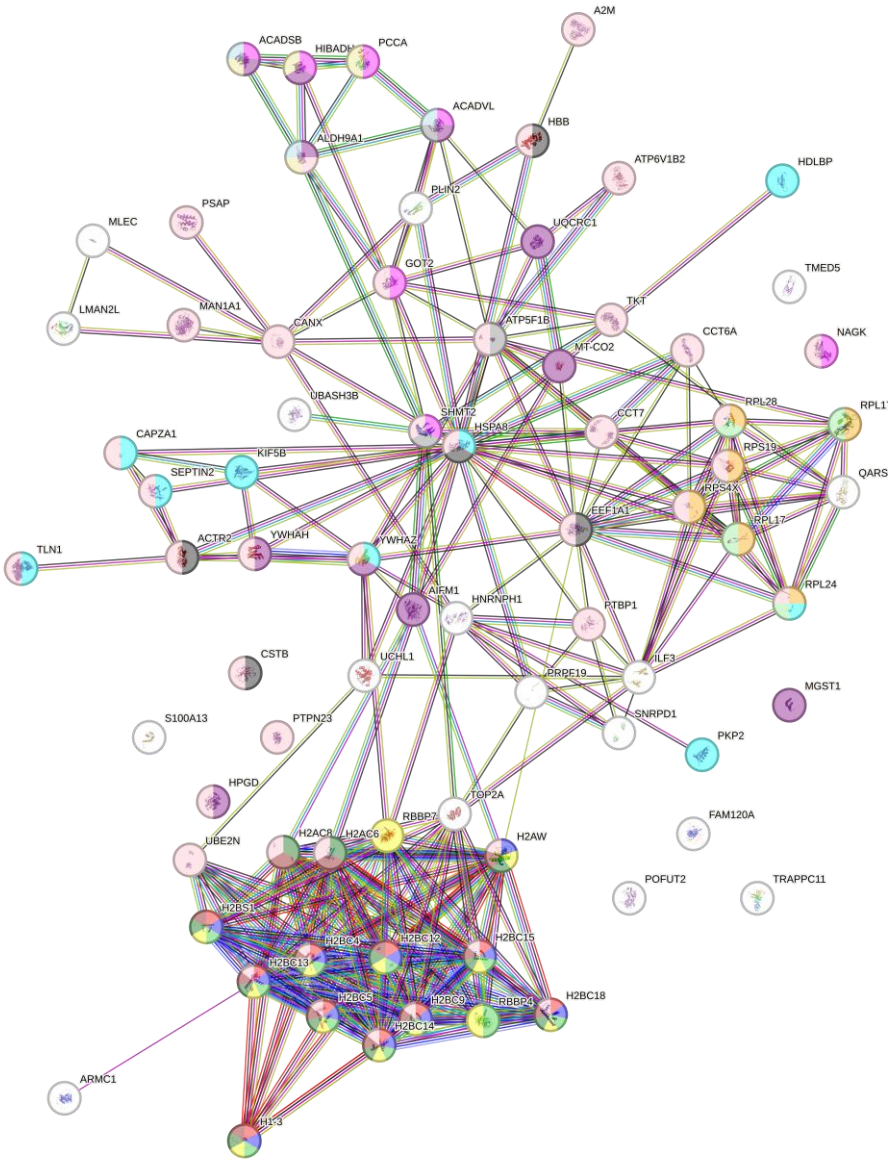

Figure 14. Protein-protein network analysis for ART-HLO v UN-HLO control.

Protein-Protein interaction showing significantly differentially proteins and their respective altered pathways during ART treatment. 96 proteins showing significantly differential expression between ART-HLO sample groups and UN-HLO sample groups were analysed. Proteins are represented as nodes while interactions appear as edges. The quantity of edges relates to the strength of the interaction relationship.

6.5 Distinct clustering of A+TB-HLO compared to UN-HLO.

Among the 2006 identified and quantified proteins from D-CYPHR output file (*Table S1*), Proteins with 80% minimum valid values in at least one group were quantified by LFQ and log-transformed into relative expression between A+TB-HLO and UN-HLO groups resulting in expression profiles of 1820 proteins (*Data sheet 1*). Of those, 79 proteins were significantly differentially expressed (*Figure 15B*). The PCA displayed a distinct clustering between A+TB-HLO and UN-HLO groups (*Figure 15A*). Out of 79 significantly DEPs (*Figure 15B*), 19 proteins reached statistical significance after Benjamin-Hochberg (BH) multiple sample correction testing. 8 of those proteins were significantly having high abundance levels and 11 were significantly having low abundance levels between A+TB-HLO and UNHLO (Data sheet 2, *Figure 15C*).

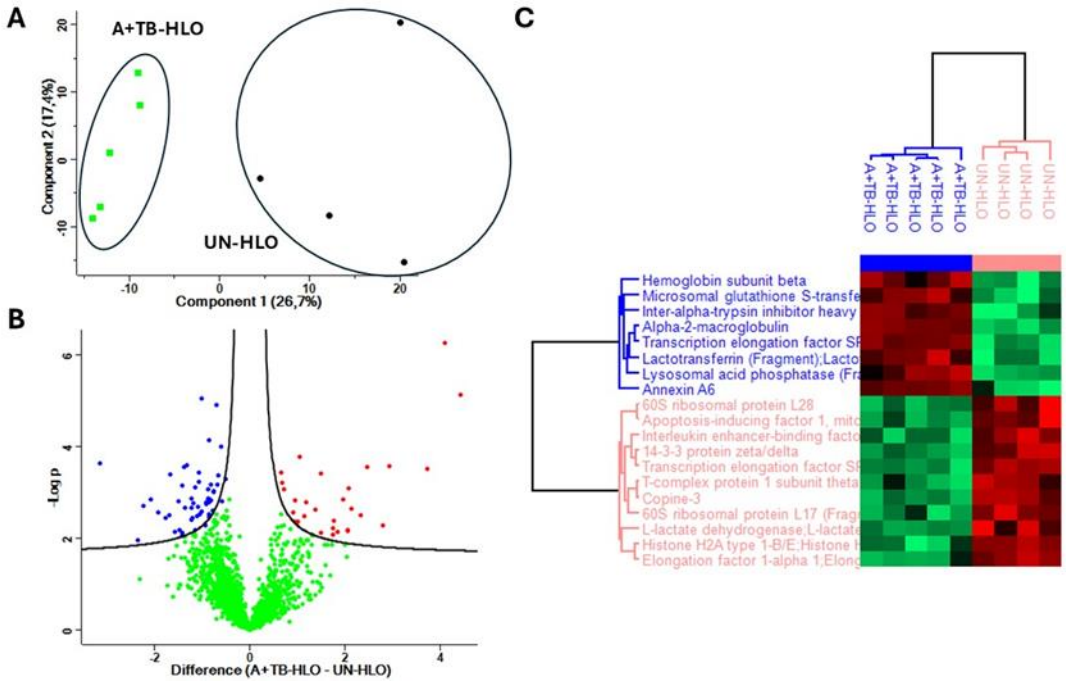

Figure 15. Identification of differentially expressed proteins in A+TB-HLO compared to UN-HLO control.

(A) Principal Component Analysis (PCA) analysis of protein expression UN-HLO and A+TB-HLO. (B) Volcano plots showing significantly high- or low abundance proteins (adjusted p= 0.05) comparing differences in log2 fold changes among x-axis represent protein difference (log2-transformed fold changes) between A+TB-HLO and UN-HLO protein expression. Statistical significance (-log10 p-value) is indicated on the y-axis.

Blue dots represent proteins with negative log2 fold change (higher expression in UNHLO sample groups) and red dots depicts those with positive log2 fold change (higher expression in A+TB-HLO sample groups). Lemon dots represent non-significant proteins as set by an FDR value of 0.05 and S0 value of 0.05 in Perseus software. (C) Protein heatmap based on unsupervised hierarchical clustering of all significantly differentially expressed proteins between A+TB-HLO (n=5) and UN-HLO (n= 3) in Perseus software. The rows are normalized Z-scores (q = 0.05). high abundance proteins are represented in red colour and low abundance proteins are represented in green colour, respectively. Dark-black colour represents missing protein values within the heatmap.

Top high abundance proteins in A+TB were involved in the following functions: (1), innate immunity such as A2M and lactotransferrin (LTF); (2), maintenance of chromatin structure including transcription elongation factor SPT6 (SUPT6H); (3) regulation of oxidative stress such as MGST1; and (4), regulation of molecular and cellular functions in the brain during development and adulthood such as lysosomal acid phosphatase (ACP2) (*Table 7*). Low abundance proteins in ART-HLO were involved in the followed functions: (1), the regulation of mRNA processing and transcription elongation by RNA polymerase such as the SUPT5H; (2), calcium dependent binding including Copine-3 (CPNE3); (3), regulation of cellular and metabolic pathways which include 14-3-3 protein zeta/delta (YWHAZ); (4), regulation of innate immunity such as elongation factor 1-alpha 1 (EEF1A1); and (5), transcription regulation, DNA replication, maintenance of chromosomal and DNA repair include Histone H2A type 1-C (H2AC4) (*Table 7*).

These highly DEPs in A+TB-HLO were further visualized using the unsupervised hierarchical clustering using a heatmap (ANOVA, FDR≤0.05) in Perseus software. Hierarchical clustering data revealed a clear separation between A+TB-HLO and UNHLO samples (*Figure 14C*). Taken together, these data demonstrated that ART-HLOs have a distinct proteomic profile compared to UN-HLOs. The top high abundance proteins in A+TB-HLOs were associated with regulation of immune response, organelle structural maintenance and oxidative stress while downregulated proteins were involved in transcription and regulation of cellular and metabolic signalling pathways.

Table 7. Top high (A) and low (B) abundance proteins in A+TB-HLO vs UN-HLO.

Protein ID	Description	Gene name	FC	-log (p-Value)
(A) Upregulated proteins				
P01023	Alpha-2-macroglobulin	A2M	4,091	6,254
Q7KZ85	Transcription elongation factor SPT6	SUPT6H	4,414	5,136
P02788	Lactotransferrin	LTF	2,930	3,568
P10620	Microsomal glutathione S transferase 1	MGST1	2,455	3,549
P11117	Lysosomal acid phosphatase	ACP2	1,059	3,771
(B) Downregulated proteins				
O00267	Transcription elongation factor SPT5	SUPT5H	-1,024	5,056
O75131	Copine-3	CPNE3	-0,704	4,902
P63104	14-3-3 protein zeta/delta	YWHAZ	-0,864	4,147
P68104	Elongation factor 1-alpha 1	EEF1A1	-0,606	3,987
P04908	Histone H2A type 1-C	H2AC4	-3,144	3,637

6.6 Functional gene ontology (GO) enrichment analysis.

Based on gene ontology analysis of upregulated proteins in A+TB-HLOs (*Data sheet 4*, *Figure 16A*), we found that most of these proteins enriched for BP were involved response to carbon dioxide, embryonic liver development, and negative regulation of complement system, and lectin pathway (*Figure 16A*). These proteins were also localized in extracellular exosomes and blood particles. Additionally, gene ontology MF analysis showed these proteins were involved in tumour necrosis factor binding, brain derived neurotrophic binding, interleukin 8 binding, serine-type endopeptidase inhibitor activity, calcium dependent protein binding, and endopeptidase inhibitor activity (*Figure 16A*).

According to gene ontology BP analysis, low abundance proteins were mostly enriched for negative regulation of cellular proliferation, translation, translational elongation,

protein localization, and heterochromatin organization (*Data sheet 4*, *Figure 16B*). These proteins were localized in the cytosolic ribosome, nucleus, nucleosome, and the extracellular exosome. Furthermore, gene ontology MF analysis showed the proteins were involved in DNA binding, RNA binding, translation elongation factor activity, nucleosomal DNA binding and structural constituent of chromatin (*Figure 16B*).

6.7 Functional pathway enrichment analysis

KEGG pathway-based functional enrichment analysis of the differentially expressed proteins revealed that high abundance proteins were significantly enriched in ribosomal, neutrophil extracellular trap formation, ATP-dependent chromatin remodelling and necroptosis pathways (*Data sheet 4*, *Figure 17*). Low abundance proteins were not enriched in any pathways.

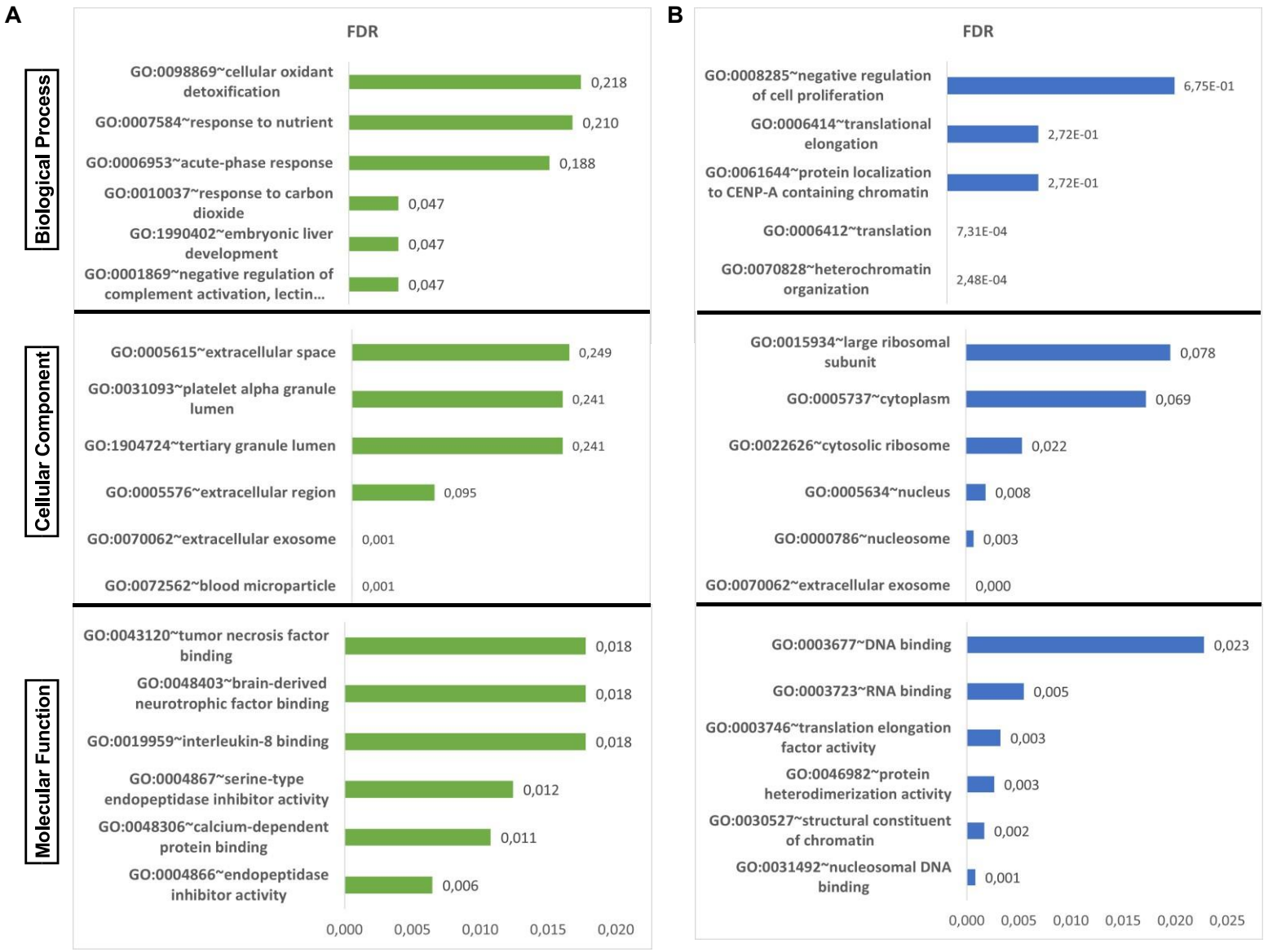
A
B
FDR
Biological Process
GO:0098869~cellular oxidant detoxification
0,218
GO:0007584~response to nutrient
0,210
GO:0006953~acute-phase response
0,188
GO:0010037~response to carbon dioxide
0,047
GO:1990402~embryonic liver development
0,047
GO:0001869~negative regulation of complement activation, lectin...
0,047
GO:0008285~negative regulation of cell proliferation
6,75E-01
GO:0006414~translational elongation
2,72E-01
GO:0061644~protein localization to CENP-A containing chromatin
2,72E-01
GO:0006412~translation
7,31E-04
GO:0070828~heterochromatin organization
2,48E-04
Cellular Component
GO:0005615~extracellular space
0,249
GO:0031093~platelet alpha granule lumen
0,241
GO:1904724~tertiary granule lumen
0,241
GO:0005576~extracellular region
0,095
GO:0070062~extracellular exosome
0,001
GO:0072562~blood microparticle
0,001
GO:0015934~large ribosomal subunit
0,078
GO:0005737~cytoplasm
0,069
GO:0022626~cytosolic ribosome
0,022
GO:0005634~nucleus
0,008
GO:0000786~nucleosome
0,003
GO:0070062~extracellular exosome
0,000
Molecular Function
GO:0043120~tumor necrosis factor binding
0,018
GO:0048403~brain-derived neurotrophic factor binding
0,018
GO:0019959~interleukin-8 binding
0,018
GO:0004867~serine-type endopeptidase inhibitor activity
0,012
GO:0048306~calcium-dependent protein binding
0,011
GO:0004866~endopeptidase inhibitor activity
0,006
0,000
0,005
0,010
0,015
0,020
GO:0003677~DNA binding
0,023
GO:0003723~RNA binding
0,005
GO:0003746~translation elongation factor activity
0,003
GO:0046982~protein heterodimerization activity
0,003
GO:0030527~structural constituent of chromatin
0,002
GO:0031492~nucleosomal DNA binding
0,001
0,000
0,005
0,010
0,015
0,020
0,025

Figure 16. Functional GO enrichment analysis of all differentially expressed proteins.

A combined list of significantly high - and low abundance proteins was used for analysis, and an (adjusted p-value<0.05) was considered statistically significant. Enrichment analysis for (A) GO cellular component and (C) GO molecular function and KEGG pathway analysis was performed using STRINGDB. Fold enrichment relative to the Homo Sapiens proteome is displayed at the x-axis. Bars with colour intensities reflecting statistical significance of enriched processes. Highly enriched processes were denoted by an intense red colour, followed by moderately enriched (pink-purple colour) and less enriched blue colour.

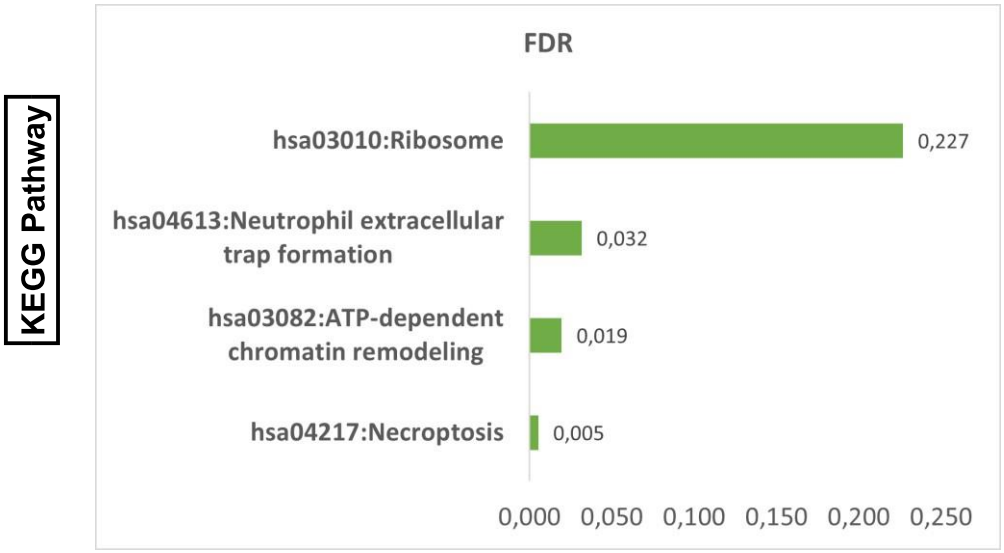

Figure 17. Functional enrichment pathway analysis.

KEGG pathway analysis was performed in DAVID v2024q1, and the generated data was visualized. FDR relative to the Homo Sapiens proteome is displayed at the x-axis. Proteins with FDR cut of value < 0,05 and p value ≤ 0.05 were considered significantly enriched.

6.8 Establishment of protein-protein interaction (PPI) network analysis

To elucidate how A+TB treatment affects the overall composition of HLO proteomic signature, we performed pathway enrichment analysis of DEPs and a putative protein-protein interaction (PPI) network using STRINGDB. PPI network analysis was performed with a minimum required interaction score set to the confidence of 0.4. The

tubular output was generated from STRINGDB tool. A PPI network represents a network with 20 nodes and 29 edges, and a significant PPI enrichment p<3.65e-07 (*Figure 18*).

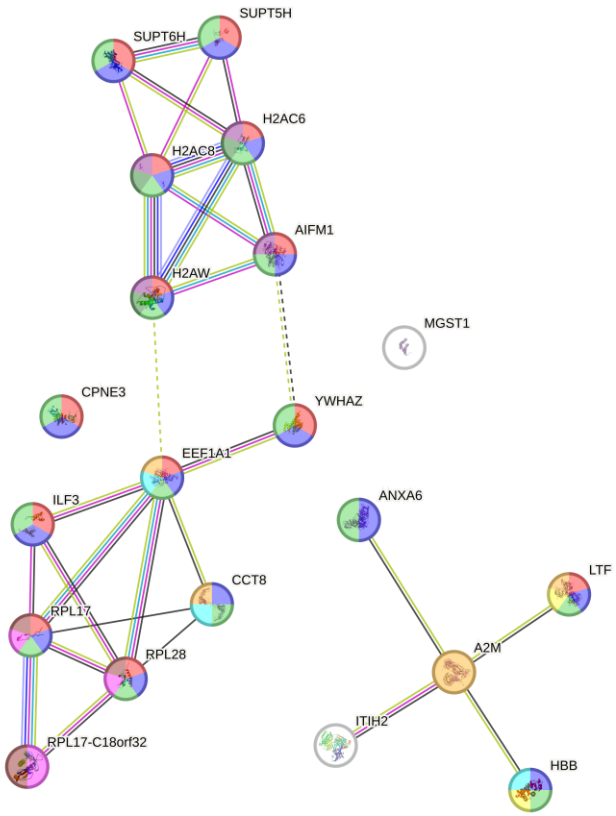

Figure 18. Protein-protein network analysis for A+TB-HLO compared with UNHLOs.

Protein-protein interaction showing significantly differentially proteins and their respective altered pathways during A+TB treatment. Proteins showing significantly differential expression between A+TB-HLO and UN-HLO were analysed. Proteins are represented as nodes while interactions appear as edges. The quantity of edges relates to the strength of the interaction relationship.

6.9 Distinct clustering of TGZ-HLO compared to UN-HLO.

Out of 2006 identified and quantified proteins from D-CYPHR output file (*Table S1*), proteins with 80% minimum valid values in at least one group were quantified by LFQ and log-transformed into relative expression between TGZ-HLO and UN-HLO groups

resulting in expression profiles of 1937 proteins (*Data sheet 1*). Of these, 164 proteins were significantly differentially expressed (*Figure 19B*). PCA plot displayed a distinct clustering between TGZ-HLO and UN-HLO (*Figure 19A*). Out of 164 significantly DEPs, 52 proteins reached statistical significance after Benjamin-Hochberg multiple sample correction testing. Of those, 11 proteins were significantly in high abundance, and 41 proteins were in low abundance between TGZ-HLO and UN-HLO (Data sheet 2, *Figure 19C*).

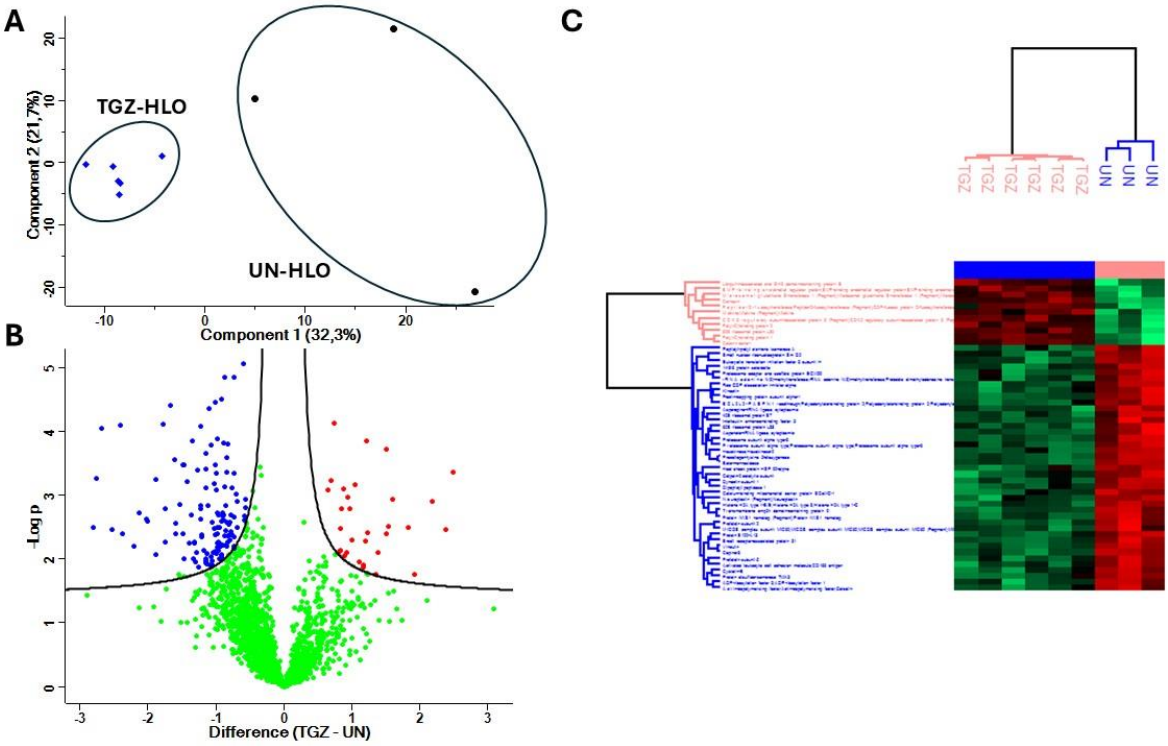

Figure 19. Identification of differentially expressed proteins in TGZ-HLO compared to UN-HLO counterpart control.

(A) Principal component analysis (PCA) analysis of protein expression UN-HLO and TGZ-HLO. (B) Volcano plots showing significantly high- or abundance proteins (adjusted p=0.05) comparing differences in log2 fold changes among x-axis represent protein difference (log2-transformed fold changes) between TGZ-HLO and UN-HLO protein expression. Statistical significance (-log10 p-value) is indicated on the y-axis. Blue dots represent proteins with negative log2 fold change (higher expression in UNHLO sample groups) and red dots depicts those with positive log2 fold change

(higher expression in TGZ-HLO sample groups). Lemon dots represent non-significant proteins as set by an FDR value of 0.05 and S0 value of 0.05 in Perseus software. (C) Protein heatmap based on unsupervised hierarchical clustering of all significantly differentially expressed proteins between TGZ-HLO (n=5) and UN-HLO (n=3) in Perseus software. The rows are normalized Z-scores (q=0.05). high abundance proteins are represented in red colour and low abundance proteins are represented in green colour, respectively. Dark-black colour represents missing protein values within the heatmap.

The top high abundance proteins in TGZ-HLO (*Table 8*) were involved in the following functions: (1), protein synthesis (60S ribosomal protein L36 [RPL36]); (2), regulation of iron and RNA translation (Poly(rC)-binding protein 1 [PCBP1]); (3) regulation of ROS production (MGST1); (4) regulation of vascular inflammation through modulation of leukocytes adhesion and migration (BMP-binding endothelial regulator protein [BMPER]); and, (5) migration of leukocytes, induction of chemokines and suppression of regulatory T cells [Midkine [MDK]). Low abundance proteins include those involved in the following functions: (1), regulation of autophagy and apoptosis (B cell receptor associated protein 31 [BCAP31]); (2), protein synthesis (60S ribosomal protein L38 [RPL38]); (3), export of proteins that lack a signal peptide (Protein S100-A13 [S100A13]); (4) cell cycle regulation, DNA metabolism and mRNA stability (ILF3), and (4), protein trafficking and degradation (TMED9).

These highly DEPs in TGZ-HLO were visualized using unsupervised hierarchical clustering heatmap (ANOVA, FDR ≤ 0.05) in Perseus software. Hierarchical clustering data revealed a clear separation between TGZ-HLO and UN-HLO (*Figure 19C*). Taken together, these data demonstrated a clear distinction between ART-HLO and UN-HLO proteomic profiles. The top high abundance proteins in TGZ-HLO were associated with protein synthesis, regulation of iron, ROS production, modulation of leukocytes and chemokines while low abundance proteins more involved in cellular death pathways, protein transport, cell cycle, and metabolism.

Table 8. Top high (A) and low (B) abundance proteins in TGZ-HLO vs UN-HLO.

Protein ID	Description	Gene name	Fold change	-log (p-Value)
(A) Upregulated proteins				
Q9Y3U8	60S ribosomal protein L36	RPL36	1,224	3,85559
Q15365	Poly(rC)-binding protein 1	PCBP1	1,516	3,7255
P10620	Microsomal glutathione S transferase 1	MGST1	2,496	3,36319
Q8N8U9	BMP-binding endothelial regulator protein	BMPER	1.050	3,17631
P21741	Midkine	MDK		2,94464
(B) Downregulated proteins				
P51572	B-cell receptor-associated protein 31	BCAP31	-1,098	4,36437
P63173	60S ribosomal protein L38	RPL38	-2,754	3,270
Q99584	Protein S100-A13	S100A13	-1,780	4,110
Q12906	Interleukin enhancer-binding factor 3	ILF3	-0,837	3,36177
Q9BVK6	Transmembrane emp24 domain containing protein 9	TMED9	-1,217	4,08457

6.10 Functional gene ontology (GO) enrichment analysis.

Based on gene ontology analysis of upregulated proteins in TGZ-HLO, we found that these proteins were insignificantly enriched for BP, CC, and MF (*Data sheet 5*, *Figure 20A*). Gene ontology BP analysis of low abundance proteins showed enrichment in cellular copper ion homeostasis, proteolysis involved in cellular protein catabolic process and regulation of receptor internalization (*Figure 20B*). These proteins were localized in cytoplasm, ficolin-1-rich granule lumen, cytosol, secretory granule lumen, cytosol, and extracellular exosomes (*Figure 20B*).

6.11 Functional enrichment pathway analysis

KEGG pathway-based functional enrichment analysis of DEPs revealed that high abundance proteins were insignificantly enriched in ferroptosis whilst low abundance proteins were enriched in the necroptosis pathway only (*Data sheet 5*, *Figure 21A & B*). Furthermore, they were insignificantly enriched for shigellosis, neutrophil

extracellular trap formation, alcoholism, and systemic lupus erythematous and ATP-independent chromatin remodelling (*Figure 21B*).

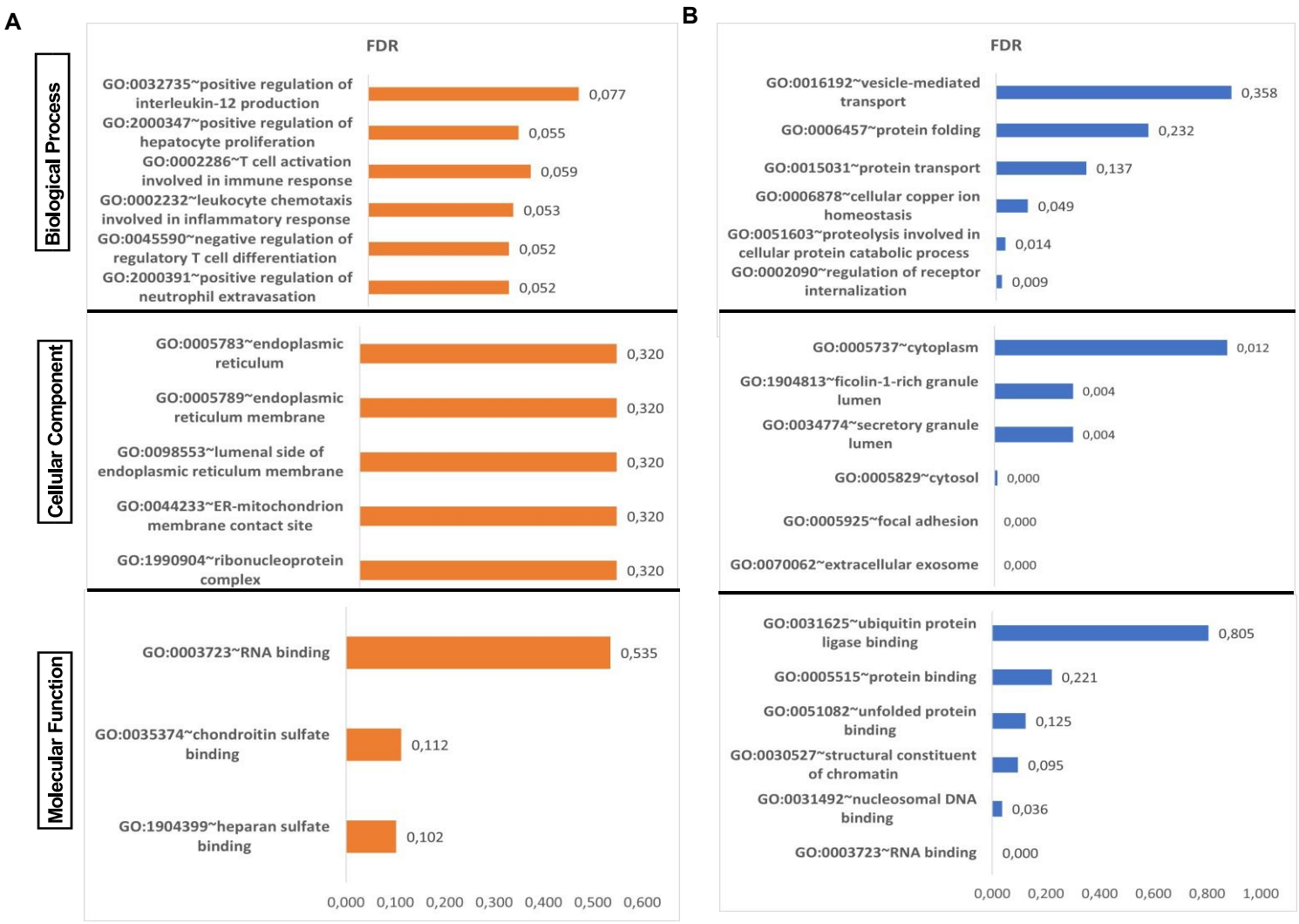
A
B
Biological Process
Cellular Component
Molecular Function
FDR
GO:0032735~positive regulation of interleukin-12 production
0,077
GO:2000347~positive regulation of hepatocyte proliferation
0,055
GO:0002286~T cell activation involved in immune response
0,059
GO:0002232~leukocyte chemotaxis involved in inflammatory response
0,053
GO:0045590~negative regulation of regulatory T cell differentiation
0,052
GO:2000391~positive regulation of neutrophil extravasation
0,052
GO:0005783~endoplasmic reticulum
0,320
GO:0005789~endoplasmic reticulum membrane
0,320
GO:0098553~lumenal side of endoplasmic reticulum membrane
0,320
GO:0044233~ER-mitochondrion membrane contact site
0,320
GO:1990904~ribonucleoprotein complex
0,320
GO:0003723~RNA binding
0,535
GO:0035374~chondroitin sulfate binding
0,112
GO:1904399~heparan sulfate binding
0,102
0,000 0,100 0,200 0,300 0,400 0,500 0,600
FDR
GO:0016192~vesicle-mediated transport
0,358
GO:0006457~protein folding
0,232
GO:0015031~protein transport
0,137
GO:0006878~cellular copper ion homeostasis
0,049
GO:0051603~proteolysis involved in cellular protein catabolic process
0,014
GO:0002090~regulation of receptor internalization
0,009
GO:0005737~cytoplasm
0,012
GO:1904813~ficolin-1-rich granule lumen
0,004
GO:0034774~secretory granule lumen
0,004
GO:0005829~cytosol
0,000
GO:0005925~focal adhesion
0,000
GO:0070062~extracellular exosome
0,000
GO:0031625~ubiquitin protein ligase binding
0,805
GO:0005515~protein binding
0,221
GO:0051082~unfolded protein binding
0,125
GO:0030527~structural constituent of chromatin
0,095
GO:0031492~nucleosomal DNA binding
0,036
GO:0003723~RNA binding
0,000
0,000 0,200 0,400 0,600 0,800 1,000

Figure 20. Functional GO enrichment analysis.

A combined list of significantly high- and low abundance proteins was used for analysis, and an (adjusted p<0.05) was considered statistically significant. Enrichment analysis for (A) GO cellular component and (C) GO molecular function and KEGG pathway analysis was performed using STRINGDB. Fold enrichment relative to the homo sapiens proteome is displayed on the x-axis. Bars with colour intensities reflecting statistical significance of enriched processes. Highly enriched processes were denoted by an intense red colour, followed by moderately enriched (pink-purple colour) and less enriched blue colour.

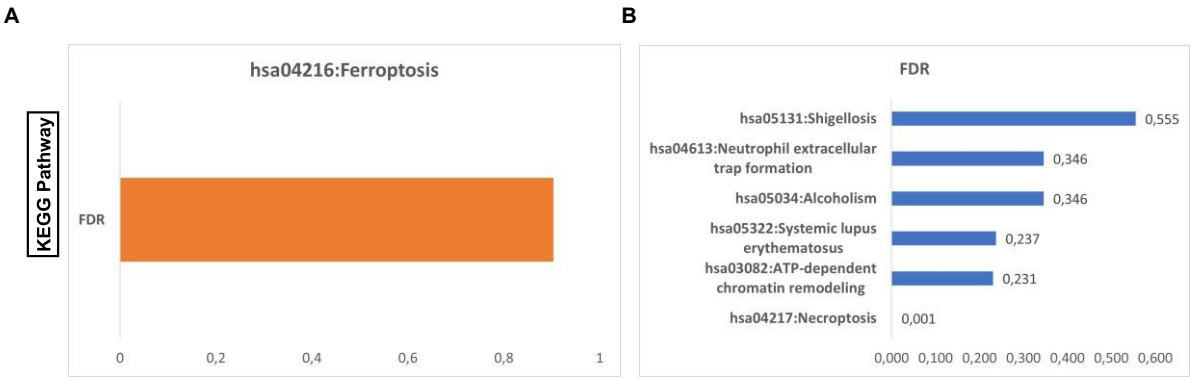

Figure 21. Functional enrichment pathway analysis.

KEGG pathway analysis for (A) high abundance proteins and (B) low abundance proteins in TGZ-HLO compared to UN-HLO was performed in DAVID v2024q1, and the generated data was visualized in a bar graph. FDR relative to homo sapiens proteome is displayed on the x-axis. Proteins with FDR<0,05 and p≤0.05 were considered significantly enriched.

6.12 Establishment of protein-protein interaction network analysis.

To elucidate how TGZ treatment affected the overall composition of HLO proteomic signature, we performed pathway enrichment analysis of DEPs and a putative protein-protein interaction (PPI) network using STRINGDB. PPI network analysis was performed with a minimum required interaction score set to the confidence of 0.4. The tubular output was generated from STRINGDB tool. A PPI network represents a network with 55 nodes and 91 edges, and a significant PPI enrichment *p*< 2.98e-10 (*Figure 22*).

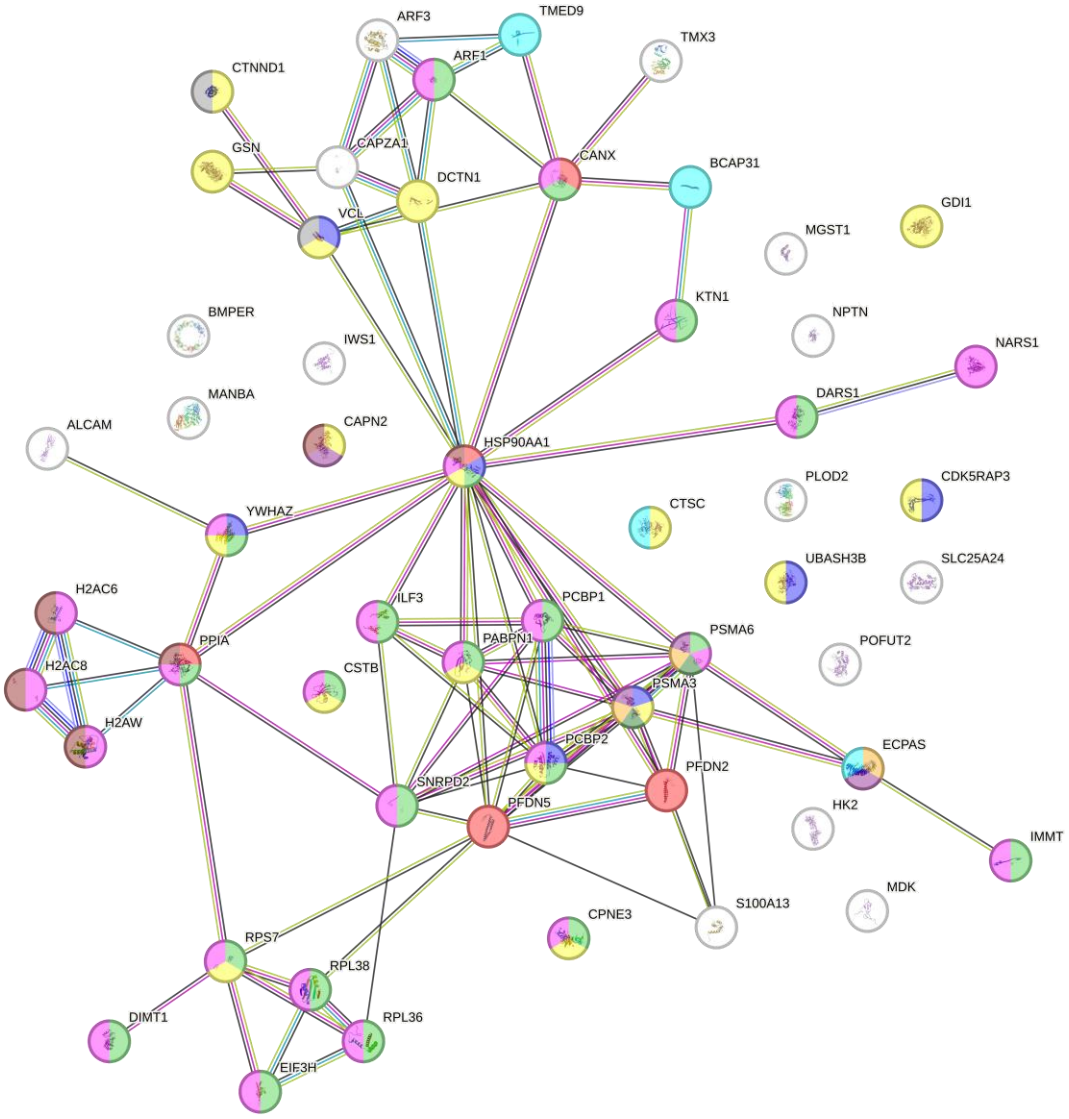

Figure 22. Protein-protein network analysis for TGZ-HLO group and control.

Protein-protein interaction showing significantly differentially proteins and their respective altered pathways during TGZ treatment. Proteins showing significantly differential expression between TGZ-HLO and UN-HLO were analysed. Proteins are represented as nodes while interactions appear as edges. The quantity of edges relates to the strength of the interaction relationship.

Chapter 7: Discussion

Advances in organoids development provide a unique tool to study organ developmental biology cues, disease modelling and drug screening. 3D organoids have successfully been cultured from *LGR5*+ marked intestinal stem cells, which recapitulate cellular heterogeneity and physiological environment of the native tissue. Indications for potential usefulness of this culture system for modelling liver and drug toxicity came from observations that hepatic organoids express major liver drug metabolizing enzymes. Hepatic organoids were successfully used for modelling steatohepatitis [11], rotavirus infection and antiviral drug development [126]. Antiretroviral therapy (EFV, LMV and 3TC), anti-TB regimen (RIF and INH) and antidiabetic drug (TGZ) are gold standard therapy for the people living with HIV/AIDS, coinfection of HIV/AIDS-TB, and diabetes, respectively, despite their known adverse events such as liver injury [127–129]. It is important to understand the molecular factors that drive liver injury to prolong the use of highly effective therapies for HIV, TB, and diabetes.

In the present study, we identified 65 differentially expressed (11 of which were differentially highly abundant and 44 lowly abundant) proteins in whole cell lysates of ART-HLO group compared with UN-HLO using a label free quantitative MS analysis. Analysis showed that 19 proteins were differentially expressed in ART-HLO, 8 of those proteins were significantly differentially highly abundant and 11 were lowly abundant in the A+TB-HLO compared with UN-HLO. Also, analysis showed that out of 52 differentially expressed proteins, 11 proteins levels were significantly highly abundant, and 41 proteins were lowly abundant in TGZ-HLO compared with UN-HLO. The selected proteins that were highly differentially abundant (A2M, MGST1, HBB, RBBP7, LTF, PCBP1, and MDK) or lowly differentially abundant (ILF3, AIMF1, CPNE3, EF1A1, and BCAP31) in each treatment group are discussed below.

A2M, belongs to the α-M family of proteins and is the largest (720 KDa) major protease inhibitor and a tetrameric protein found in the blood [130]. In the present study, A2M protein was differentially highly abundant in ART-HLO, A+TB-HLO and TGZ-HLO groups compared to UN-HLO. In accordance with our data, Atanosova and colleagues also showed that serum levels of A2M were upregulated in patients with chronic HCV infection treated with pegylated interferon alpha [131]. Furthermore, upregulation of

A2M has been suggested as the simplest serum biomarker for liver fibrosis and fibrogenesis in chronic hepatitis C and a marker of endothelial dysfunction [131]. In agreement, another study reported that A2M concentrations in blood were significantly associated with concentrations of neuronal injury markers in cerebrospinal fluid (CSF) [132]. An increase in A2M levels inhibits matrix proteins catabolism and induction of liver fibrosis in inflammatory or injured liver [131]. Additionally, studies have shown that A2M can also exhibit binding and carrier functions for cytokines, including nerve growth factor (NGF), IL-1β, and IL-6, among others [133], leading to induction of several defence reactions like immune response, acute phase reaction and haematopoiesis [133]. Thus, acting as a protein inhibitor [131], carrier and binder [132] could be the mechanisms by which A2M utilize to exert immune functions, acting in inflammatory responses.

Haemoglobin (Hb) is a tetrameric globular protein composed of two α and β polypeptide chains, each containing one heme molecule [134]. Hb primarily functions to transport oxygen from the lung to peripheral tissues [134]. In the present study, HBB protein was differentially highly abundant in the ART-HLO compared to UN-HLO. These findings aligned with those found in a study that sought to investigate whether HBB was expressed in hepatocytes and how it's related to oxidative stress in NASH patients [135]. In that study, microarray analysis revealed high expression levels of HBB in liver biopsies from NASH patients and HepG2 cell line [135]. Shaver and colleagues identified that HBB-induced NLRP3 inflammasome increased the expression of IL-1β in TLR-4 dependent manner in mouse macrophages and caused inflammation in an acute lung injury model [136]. Also, oxidized Hb upregulated inflammatory factors such as IL-1β, IL-6, IL-8, and TNF-α and caused tissue apoptosis in an intraventricular haemorrhage (IVH) model [137]. In contrast, a study by Liu and colleagues demonstrated that hydroperoxide treatment (an inducer of apoptosis) in HepG2 and HEK293 cells increased HBA1 and HBB expression levels but overexpression of HBB reduced oxidative stress [135].

Microsomal glutathione S-transferase 1 (MGST1), a membrane bound transferase, mainly located in the mitochondria, ER plasma and peroxisome, and protects cells against various toxic or electrophilic chemical agents [138]. MGST1 primarily exhibits protective functions using its Glutathione S-transferase and peroxidase activity [139].

MGST protein levels were highly differentially abundant in ART-HLO, A+TB-HLO and TGZ-HLO groups compared UN-HLO. Other studies have demonstrated that MGST1 plays a crucial role in protecting the cells from oxidative stress induced by the cumene hydroperoxide (CuOOH) and oxidized docosahexaenoic acid [139,140]. These findings were further corroborated by a series of studies which showed that treatment of MGST1 transfected cells with CuOOH and the tert-Butyl hydroperoxide (BuOOH) resulted in fewer lipid peroxidation products compared to the antisense control [139]. Interestingly, addition of Vitamin E to the MGST1 transfected cells mediated protection against cytotoxicity induced by the hydroperoxides, although it was ineffective in contributing to the MGST1-mediated suppression of the cytotoxic effects of 4-HNE or cisplatin [139,141].

Retinoblastoma binding protein 4/7 (RBBP4/7) are known as the histone chaperones which belongs to the WD40 family, and they are ubiquitously expressed widely across various cell type [142]. Here, RBB4/7 protein levels were differentially highly abundant in ART-HLO compared to UN-HLO. RBBP4/7 are involved in DNA repair, making them essential players in maintaining genome integrity [143]. Studies have shown that nucleosome remodelling and deacetylation (NuRD) complex controls gene expression and DNA damage repair via modulating nucleosome RNA polymerase accessibility at the binding sites of transcription factors, enhancers, and promoters [142,143]. Evidence has shown that RBBP4/7 interacts with the C-terminal domain of BRCA1 protein and inhibit its transactivation activity [144]. A subsequent study reported that an association between BRCA1 and RBBP4/7 is disrupted in cells treated with DNA-damaging agents [144]. RBBP4/7 in conjunction with BRCA1 play a role in DNA repair and aberrant expression may affect this response; thus, leading to the accumulation of damaged DNA [144]. Therefore, high abundance protein levels of RBB4/7 in our data may be consequent to increased accumulation of damaged DNA in HLOs.

Lactotransferrin (LTF), also known as lactoferrin, plays an important role in innate immune defence [145]. LTF has iron-binding ability, which enables it to transport Fe^{3+} ions [145–147]. By sequestrating Fe^{3+} ions, LTF helps to prevent oxidative stress induced cell damage [146]. In the present study, LFT protein level was differentially highly abundant in A+TB-HLO compared with UN-HLO. Intriguingly, research has shown the protective effects of LTF against hepatic and liver fibrosis via the inhibition

of NF-κβ signalling in a non-alcoholic steatohepatitis rat model [145]. The cytoprotective role of LTF may be associated with the inhibition of ER stress, inflammation, promotion of autophagy of damaged hepatocytes and the induction of hypoxia-inducible factor-1α/VEGF to facilitate liver function recovery [148]. Accordingly, LTF reduced the levels of liver inflammatory biomarkers including, alanine aminotransferase (ALT), aspartate aminotransferase (AST) and hydroxyproline in thioacetamide (TAA)- treated liver tissues, while increasing catalase levels [147]. Additionally, LTF treatment reduced gene expression of inflammatory markers such as IL-1β, Icam-1 and profibrogenic factors including alpha smooth muscle (α-SMA), collagen I, and connective tissue growth factor (CTGF) in TAA-treated liver tissues [147]. Also, LTF reduced TAA induced reactive oxygen species (ROS) production and cell death in FL83B cells and reduced α-SMA, collagen I, and p-Smad2/3 productions in TGF-β1-treated HSC-T6 cells [147]. Altogether, these findings reinforce the anti-inflammatory and the antioxidant functions of LTF and may be indicative of LTF exerting its anti-inflammatory and antioxidant functions against A+TB treatment in our study.

Interleukin enhancer binding factor 3 (ILF3) also known as NF90/NF110 encodes a double-stranded RNA binding protein that complexes with other proteins, and RNAs including mRNAs, small non-coding RNA, and double stranded RNA, to regulate gene expression and stabilize mRNAs [149–151]. Evidence from previous a study reported that overexpression of ILF-3 increased autophagy whereas downregulation led to a marked autophagy inhibition by decreasing beclin-1 (Bec-1) protein during adenosine induced cytotoxicity in HepG2 cells [152]. Furthermore, cytotoxicity was synergized by the overexpression of MEG3 through downregulated ILF-3 to activate PI3K/Akt/mTOR and inactivate the beclin-1 signalling pathway [152]. In the present study, ILF-3 protein was differentially in low abundance in ART-HLO and TGZ-HLO groups compared to UN-HLO group. In contrast to our findings and that of previous studies, other evidence in the literature showed an upregulation of ILF3 and nuclear enriched abundant transcription 1 (NEAT1) proteins in polymorphonuclear cells (PBMCS) of patients suffering from sepsis and as well as lipopolysaccharide (LPS) stimulated RAW265.7 [153]. However, silencing of IL-F3 promoted M2 polarization in RAW264.7 cells [153].

Therefore, more studies exploring the role of ILF-3 in drug induced liver injury are required.

Apoptosis inducing factor, mitochondrion associated 1 (AIFM1) protein levels was differentially in low abundance in the ART-HLO group compared with UN-HLO group. AIFM1 is a mitochondrial flavoprotein with dual roles in redox signalling and programmed cell death [154]. Freyer and colleagues reported that AIFM1 gene expression was reduced in APAP-treated microscale 3D liver bioreactors compared to a control [155]. Studies in patients with diabetic nephropathy showed a decrease in AIF within the renal tubular compartment and lower *AIFM1* renal cortical gene expression significantly correlated with declining glomerular filtration rate [156]. In the same study, overexpression of *AIFM1* rescued glucose-induced disruption of mitochondrial respiration [156]. The proapoptotic functions of AIFM1 are based on the activation of the caspase-independent pathway upon apoptotic inducer, whilst its anti-apoptotic roles are part of the regular mitochondrial metabolism through NADH oxidoreduction [154,156]. ART treatment induces mitochondrial dysfunction, thus, downregulated AIFM1 expression in our data could be a consequence of impaired mitochondrial function.

Copine-3 protein (CPNE3) levels were differentially in low abundance in A+TB-HLO group compared with UN-HLO group. Copine-3 is a calcium-dependent phospholipid binding protein encoded by *CPNE3 gene* and is virtually expressed in various tissues [157]. CPNE3 is involved in several biological processes such as signal transduction and pathogenesis of many cancerous diseases such as leukaemia, breast, prostate, and small cell lung cancers [158]. A recent study showed that high endogenous CPNE3 expression in clinical specimens was related to poor prognosis of advanced hepatocellular carcinoma (HCC) in patients on sorafenib treatment [159]. Silencing of endogenous CPNE3 in HCC cells decreased CPNE3 expression and enhanced the sensitivity of cancer cells to molecular target, sorafenib [159]. A recent study reported that decreased CPNE3 and receptor for activated c kinase 1 (RACK1) expression levels in hypoxia/reoxygenation (I/R)-induced H9c2 cardiomyocytes correlated with those observed in myocardial I/R injury rat model [160]. CPNE3 overexpression inhibited release of proinflammatory cytokines and decreased apoptosis in I/R induced cardiomyocytes [160].

Eukaryotic translation elongation factor 1 alpha 1 (EF1A1) is an elongation protein that catalyses GTP-dependent binding of aminoacyl-tRNA (aa-tRNA) to the A site of the translating ribosomes during protein synthesis. It has been shown to play a role in diverse cellular processes such as actin bundling, regulation of cell morphology and cell death [161]. EF1A1 has been shown to participate in lipotoxicity induced cell death downstream ER stress in HepG2 cells after exposure to high concentrations of palmitate [162]. On the contrary, inhibition of EF1A1 with Didemnin B compound, specific inhibitor of EF1A1 elongation activity, prevented recovery of protein synthesis and increase in GRP78 protein which is normally associated with later stages of the response to ongoing ER stress [162]. A+TB treatment is associated with an induction of increased tissue inflammation and oxidative stress. We observed low levels of EF1A1 protein in A+TB-HLO group. It has been reported that EF1A1 expression varies in cells treated with different concentrations of strong apoptosis inducer (hydrogen peroxide), and peroxiredoxin –1 (Prx-1) inhibitor [163]. EF1A1 provide protection against ER stress-mediated cell death [164]. Therefore, reduced expression of EF1A1 in our study may serve as an indicator of increased oxidative stress.

Poly-C binding protein 1 (PCBP1) is an RNA-binding protein reported to play a crucial role in multiple gene regulatory levels including gene transcription, post-transcription, and translation [165]. Evidence has shown that PCBP1 as a member of PCBP family has the capacity to heavily bind oxidized RNA and, therefore, partake in the cellular response to oxidative conditions and helping to induce apoptosis [166]. Our results showed that PCBP1 were differentially in high abundance in TGZ-HLO compared with UNHLO. A recent study has shown that PCBP1 deficiency suppresses the activation of caspase and hydrogen peroxide-induced apoptosis [166]. On the contrary, overexpression of PCBP1 triggered caspase-3– and caspase-8–mediated apoptosis of tumour cells; thus, making PCBP1 a tumour suppressor [167]. Furthermore, PCBP1 serves as an intracellular immune checkpoint. A recent study reported that upregulated PCBP1 expression in activated T cells prevented the conversion of effector T (T_{eff}) cells into regulatory T (T_{reg}) cells by restricting expression of the T effector cell intrinsic T regulatory commitment programs [168]. This phenomenon was critical for stabilizing T_{eff} cell functions and subverting the immune-suppressive signals [168]. In addition, T

cell–specific deletion of the *Pcbp1* gene favoured T_{reg} cell differentiation and blunted antitumor immunity [168].

Midkine (MDK) is a heparin cytokine or growth factor with a molecular weight of 13 kDa. Accumulating evidence showed that MDK protein expression levels is upregulated in malignancies, inflammatory diseases and the tissue injury [169–171], suggesting its crucial role in inflammatory reactions [170,172]. In the present study, MDK expression level was highly abundant in TGZ-HLO group compared to UN-HLO group. A previous study demonstrated that high glucose concentrations and oxidative stress enhanced. MDK expression in tubular epithelial cells and macrophages [172]. Similarly, evidence from another previous study showed that after 5/6 nephrectomy, MDK expression was increased in tubular epithelial cells and infiltrating macrophages of *MDK*+/+ mouse kidneys [173]. Moreover, MDK protein exposure to cultured primary cultured human lung microvascular endothelial cells increased expression of angiotensin converting enzyme (ACE) and further supplemental MDK protein in MDK deficient mice restored MDK protein levels [173]. In the very same study, showed that oxidative stress might be involved in MDK expression, since expression of NADH/NADPH oxidase–1, –2, and –4 was induced in the lung after 5/6 nephrectomy [173]. Accordingly, an antioxidative reagent tempol reduced MDK expression and plasma angiotensin II levels and consequently ameliorated hypertension [173].

B-cell receptor associated protein 31 (BCAP31) is a ubiquitously expressed and integral protein in the endoplasmic reticulum membrane [174]. BCAP31 C-terminus is in the cytoplasm where it mediates protein transport and regulation of functions [175]. Previous studies have reported that BCAP31 promoted vesicle trafficking of proteins of the class I molecules and tetraspanins; thus, is suggested to be involved in immunity and apoptosis [176,177]. Accumulating evidence has shown that BCAP31 depletion reduced T cell activation via regulating T-cell antigen receptor signalling in mice [177]. Reportedly, BCAP31 induced sterol regulatory element binding protein 1 activation promoted liver steatosis and worsened insulin resistance [178]. Also, BCAP31 increased tunicamycin-induced ER stress reduced the rate of fatty acid oxidation which promoted tunicamycin-induced liver steatosis [179]. On the contrary, a study has shown that patients with BCAP31 and ATP binding cassette subfamily D member 1 (ABCD1) deletions exhibited an increase in serum levels of ALT and AST compared

with healthy controls [176]. Proteomic data in the present study showed that BCAP31 protein level was lowly abundant in A+TB group compared with UN-HLO. A recent study reported that BCAP31-deficiency reduced the antioxidant response and nuclear related factor 2 (Nrf2), enhanced JNK signalling activation, and reduced hepatic inflammation, apoptosis, and amplified APA-induced hepatotoxicity in mice [180], thus suggesting importance of BCAP31 in maintaining physiological functions of the liver.

The functional enrichment and protein-protein interaction (PPI) network analysis in this study found that highly abundant proteins in the ART-HLO group mainly participated in the molecular functions primarily related to nerve growth factor (NGF), TNF, IL-1, and IL-8 binding. In A+TB-HLO, MF and the PPI functional enrichment analysis found that upregulated proteins were related to brain derived neurotrophic factor (BDNF), TNF, IL-8, calcium-dependent protein (CDP) binding, serine-type endopeptidase, and endopeptidase inhibitor activity. Functional enrichment and protein-protein interaction (PPI) network analysis in this study confirmed that lowly abundant proteins in the ART-HLO and A+TB-HLO group were mostly related to molecular functions such as nucleosomal DNA binding, cadherin, RNA and DNA binding, protein heterodimerization, and structural constituent of chromatin.

Pathway-based functional enrichment analysis of the differentially expressed proteins revealed that lowly abundant proteins in ART-HLO group were related to neutrophil extracellular trap formation, necroptosis pathway and alcoholism. and in TGZ-HLO group.

Studies on inflammatory and autoimmune diseases, which are characterized by an abnormal activation of immune cells and increased production of cytokines, have revealed a localized increase in NGF, TNF, IL-1, and IL-8 at the sites of inflammation [181–183]. A study identified NGF as a crucial regulator of stress-induced fibrogenesis signalling pathway as it activates its receptor p75 neutrophil receptor (p75NTR), increasing liver damage in TAA treated murine model [183]. TNF is a central cytokine in the inflammatory reactions, and it drives inflammatory responses by directly inducing inflammatory gene expression and indirectly inducing cell death [184,185].

TNF is a mediator of drug induced liver injury [184]. A recent study demonstrated that inhibition of the TNF receptor 1 (TNFR1) significantly reduced liver steatosis and

triglycerides content and activation of transcription factor SREBP1, and downstream target genes for lipolysis [185]. Furthermore, inhibition of TNFR1 resulted in significant reduction in apoptotic liver injury, NAFLD, ALT levels and fibrosis in the liver tissue of mice fed with high fat diet [185].

IL-1 superfamily members are a cornerstone of variety of inflammatory processes occurring in various organs including the liver [181]. Previous studies have shown that IL-1 family play an important in the induction and progression of fibrosis [181,186]. For example, a study reported that mice deficient in IL-1 receptor exhibited decreased hepatic tissue damage and reduced fibrogenesis, indicating that IL-1 is involved in the progression of liver injury to fibrosis [186]. Similarly, mice either deficient IL1α or IL-1β and fed a high-fat diet exhibited a significant reduction in the progression of steatosis to fibrosis [187].

IL-8 is a potent chemoattractant for neutrophiles and contributes to inflammation [188,189]. A previous study reported that IL-8 serum levels were significantly increased in chronic liver disease (CLD) patients, especially in end-stage cirrhosis [189]. Furthermore, patients with cholestatic diseases exhibited highest IL-8 serum concentrations and IL-8 correlated with liver function, inflammatory cytokines, and non-invasive fibrosis markers [189]. Intrahepatically, IL-8 and CXCR1 expression are strongly up-regulated [189]. Other researchers have indicated that IL8-induced liver injury was associated with upregulation of components of the NADPH oxidase 2 complex, which participate in neutrophil oxidative burst [188]. IL8-driven neutrophil cell infiltration promoted macrophage aggregate formation and upregulated the expression of chemokines and inflammatory cytokines in high-fat diet (HFD) fed mice [188]. Therefore, findings of the present study demonstrate that differentially highly abundant proteins in ART-HLO modulate the induction and binding of NGF, TNF, IL-1 and IL-8 cytokines which are heavily involved in cell immunity against tissue injury.

Pathway analysis showed that highly abundant proteins in A+TB-HLO were mostly involved in neutrophil extracellular formation, ATP-dependent chromatin remodelling, and necroptosis pathway. Neutrophil extracellular traps (NETs) are net-like structures composed of DNA-histone complexes and proteins released by activated neutrophils [190]. In addition to their key role in the innate immune responses, NETs are also involved in autoimmune disease and non-infectious diseases [190]. Large body of

evidence has shown that microbial agents, biochemical stimuli, calcium influx, immune complexes, and contact with platelets (thrombocytes) and/or damage-associated molecular patterns can trigger NETs formation [191]. Intriguingly, an earlier study reported lysosomal instability and concurrent disintegration of the nuclear morphology in neutrophils upon exposure to the nonpolar nanoparticles followed by NADPH oxidase-dependent chromatin externalization [191,192]. Additionally, some authors introduced a model where lysosomal leakage triggers a cascade of events involving ROS production and ending in formation of NETs [191]. Given that ART and A+TB treatment is associated with induction of ROS production and increased oxidative stress, we believe this could be the trigger for NETs formation in ART-HLO and A+TBHLO groups. However, further investigation into molecular mechanism leading to NETs formation in HLO upon ART and/ or A+TB treatment is warranted.

ATP-dependent chromatin remodelling, comprise group of ATP-dependent remodelers which serves to regulate DNA accessibility by repositioning, ejecting, or modifying the nucleosomes following DNA replication and DNA repair [193]. This important class of enzymes ensures proper positioning of nucleosomes to allow DNA-centric processes to occur and represent another level of regulation [193]. Eukaryotic cells contain family of four chromatin remodelers including switch/sucrose non-fermentable (SWI/SNF), Imitation switch (ISWI), chromodomain helicase DNA-binding (CHD), and inositol requiring 80 (INO80) [194]. Evidence from TAA-induced liver injury model showed that BRM-associated SWI/SNF remodelers was predominant during a decline of injury phase and initiation of regeneration phase [195]. Additionally, BRG-1 containing remodelers predominated during the regeneration phase, thus depicting an interplay between chromatin machineries in different phases of the TAA-induced liver injury and regeneration [195]. This warrants further investigations into the chromatin remodelers and interactors during ART and A+TB-induced liver injury.

Necroptosis, a regulated cell death mediated by receptor-interacting proteins kinase 1 and 3 (RIPK1, RIPK3) and mixed lineage kinase domain-like protein (MLKL) [196]. Necroptosis shares same death inducers as apoptosis including TNF, Fas, TNF-related apoptosis inducing ligand (TRAIL), or TLRs [196]. Necroptosis is regarded as a proinflammatory mode of cell death [196]. Evidence from previous studies demonstrated that RIPK1 inhibition with Nec-1 exhibited a protective effect in APAP

induced necrosis and toxicity [197–199]. Additionally, Nec-1 reduced APAP-induced JNK activation, hepatic RIPK3 expression and Glutathione depletion [199]. Another study also reported that Nec-1 reduced APAP-induced ROS burden in hepatocytes [197]. Intriguingly, evidence from a study demonstrated that neither EFV nor isoniazid can induce cell death alone [200]. However, exposure to a combination of EFV and isoniazid resulted in increased oxidative and nitrosative stress, leading to the formation of membrane permeability transition, and ultimately necrotic cell death [201]. To my knowledge, this is the first study to report necroptosis pathway enrichment in relation to A+TB and TGZ treatment.

Chapter 8: General discussion

The liver is quite a complex organ comprised of several cells with different functions. The liver is the only visceral organ capable of regeneration and detoxification of xenobiotic drugs. Preclinical cytotoxicity testing of drugs has been limited by utilization of animal models due to inter-species variability with humans. Previous *in vitro* models using cancer-derived hepatic cell lines were limited by their sub-optimal cytochrome P450 enzymes levels while primary human hepatocytes (PHH) rapidly dedifferentiation in long-term cultures thus losing functionality, respectively. These limitations provided an impetus to develop relevant and feasible *in vitro* models that could mimic physiological functions of the native organ. To this end, the aim of this thesis was to develop and generate a robust and tractable 3D multicellular human liver organoid that comprises hepatocytes, profibrotic hepatic stellate cells and Kupffer cells commonly known as tissue resident macrophages, cells crucial for maintenance of liver homeostasis and regulation of tissue injury. The main goal was to understand intricate interplay of these cells in drug induced liver injury to uncover possible pathways that are perturbed in the tissue.

In chapter 4, initial characterization analysis of stage specific markers by RT-qPCR revealed that HLO's exhibited mature hepatocytes markers including *HNF4α, ALB, CYP3A4*, and *ATA1*, while the functional assay for CYP3A4 activity demonstrated that HLOs were sensitive and capable of metabolizing xenobiotic drugs compared to HepaRG cells. Furthermore, flow cytometry showed that the frequency of hepatocytes, hepatic stellate cells and Kupffer cells was in concordance with the proportions found in native organ. Therefore, we demonstrated that HLO's represented a tractable model of the liver capable of modelling both drug metabolism and inflammation.

Previous *in vitro* liver models comprised mainly of hepatocytes and lacked other essential cell lineages important for regulating tissue injury, more importantly, inflammation. ELISA showed increased levels of pro-inflammatory cytokines (IL-6, IL-1β and IL-4), the pathological mediator TNF-α and anti-inflammatory marker (IL-10) in the drug treated-HLO's compared to untreated control group. Our data is in conformity with previous studies which showed that inflammatory markers such as IL-6 and TNF-α are increased in organoids comprising hepatocytes only [10]. Therefore, the present

study has provided a feasible and reproducible liver organoid model that could be amenable to model acute and chronic inflammatory liver diseases.

In previous studies, hepatic organoids were successfully used to model steatohepatitis, rotavirus infection and antiviral drug development [126]. ART, A+TB and TGZ are the gold standard therapy for people leaving with HIV/AIDS (PLWH), co-infection with HIV/AIDS and TB and diabetic patients, respectively, despite the known adverse events associated with liver injury. It is important to understand the molecular factors that drive liver injury. In this thesis (chapter 6), I used the HLO culture system to model ART, A+TB and TGZ-induced liver injury. The sole aim of this chapter was to uncover whether drug-treatment in HLOs induced distinct proteomes from UN-HLO so that proteins that may be mediating drug induced liver injury could be identified.

A label free quantitative MS analysis approach was employed to identify proteins associated drug induced liver injury and the analysis of drug treated HLOs and UN-HLOs separately gave us novel insights into the response to drug treatments. Successful separation of drug treated HLO and UN-HLO was shown by PCA plot and hierarchical clustering heatmaps and enrichment analysis of proteome data. ART-HLO and A+TB-HLO successfully clustered together indicating unique protein signature compared to UN-HLO, while TGZ-HLO displayed a unique protein signature to ART-HLO, A+TB-HLO and UN-HLO (*Figure 10*).

Inflammation and immune response

Dysregulation of the liver immune microenvironment plays a huge role in the initiation and progression of drug induced liver injury [202]. As is reflected in functional enrichment analysis of highly abundant proteins in ART-HLO compared to UN-HLO, a significant enrichment in nerve growth factor (NGF), tumour necrosis factor (TNF), IL-1 and IL-8 binding activities was observed. Studies on inflammatory diseases characterized by an abnormal activation of immune cells and increased production of cytokines, revealed a localized increase in NGF, TNF, IL-1, and IL-8 cytokines at the sites of inflammation [181–183]. Indeed, A2M, a protein known to be involved in the regulation of tissue damage by inhibiting proteinases released during the injury and inflammation was altered by ART treatment in HLO. Also, HBB protein level was altered

post ART. High abundant protein levels of A2M and HBB in ART-HLO suggest increased tissue damage and inflammation.

Functional enrichment analysis of highly abundant proteins post A+TB treatment in HLOs revealed regulation of immune response processes including negative regulation of complement activation, and the lectin pathway. The complement system plays an essential role in maintaining immune microenvironment within the liver [203]. Non-infectious systemic inflammatory response resulting from activation of the complement system occurs during intoxication with substances or compounds, burns, and local non-hepatic ischemia [204]. Negative regulation of complement activation serves to prevent the rate of complement activation thus protecting host cells and tissues from damage caused by activated complement [205]. Complement activation is detrimental by inducing inflammatory tissue damage, mainly observed in ischemia-reperfusion injury and transplant rejection [204].

Enrichment analysis also showed significant enrichment in TNF binding, brain derived neurotrophic factor binding (BDRFB), and IL-8 binding. Pathway enrichment analysis showed proteins were significantly enrichment in NETs formation, ATP-dependent chromatin remodelling and necroptosis. This data indicated that A+TB induced stress response may interact with immune signaling, even in the absence of microbes, which is in line with earlier reports [10]. Therefore, inflammatory signaling pathways could be targeted with therapeutic agents to minimise tissue induced inflammation during A+TB treatment.

Low abundant proteins were highly enriched for processes including negative regulation of cell proliferation, translational elongation, protein localization to CENP-A containing chromatin. While MF enrichment analysis revealed that low abundant proteins in A+TB-HLO were enriched for DNA & RNA binding, translation elongation factor activity, protein heterodimerization and structural constituent of chromatin.

Redox signaling and oxidative stress

Redox signaling and ROS species play a key role in regulated programmed cell death. It is known that redox signaling regulates cells survival and cell death in response to stress conditions [206]. Excessive ROS causes damage to DNA, lipids and protein structures and produces the 8-OH-deoxyguanosine and lipid peroxides such as

malonic dialdehyde (MDA) [206]. Importantly, MDA do not only exert the oxidation of the biofilm but also converts ROS into active substances and amplifies effect of ROS through chain reaction, causing cell membrane damage, which in turn leads to apoptosis and liver necrosis [207]. In primary rat cortical neuroglial cultures aged 21, ARVs treatment led to the accumulation of ROS and ultimately induction of neuronal damage and death [208].

In this thesis work, ART increased abundance of proteins involved in antioxidant and DNA repair functions such as MGST1 and the RBP4/7. These proteins are particularly important in reducing oxidative stress and maintaining genomic integrity. Research has shown that ROS stimulates nuclear factor-κB (NF-κB) inhibitory protein (IκB) to undergo phosphorylation and ubiquitination for degradation, thus exposing the nuclear localization sequence [209]. Subsequently, activated NF-κB translocate to the nucleus to initiate gene transcription of TNF-α, IL-1β, and other factors, which produces an inflammatory response, causes inflammatory infiltration of hepatocytes, and induces hepatic inflammatory damage [210].

A+TB treatment increased MGST1 and LFT protein levels in HLOs. LFT plays an important role in innate immune defence [145]. LTF has iron-binding ability, by sequestrating Fe^{3+} ions, LTF helps to prevent oxidative stress induced cell damage [146]. Evidence from literature argues that cytoprotective role of LTF may be associated with inhibition of ER stress, inflammation, and the promotion of autophagy of the damaged hepatocytes and induction of hypoxia-inducible factor-1α/VEGF to facilitate liver function recovery [148].

Mitochondrial dysfunction

Dysregulation of mitochondrial function leads to increased ROS, which are capable of inducing toxicity and DNA damage [211]. AIFM1 is a mitochondrial flavoprotein with dual roles in redox signalling and programmed cell death [154]. In this thesis work, ART-HLO exhibited decreased abundance of AIFM1 protein levels compared to UN-HLO. In line with results of the current research work, others reported a reduced gene expression of AIFM1 in APAP-induced microscale 3D liver bioreactors compared to a control [155]. It has been shown that reduced AIFM1 gene expression correlate with reduced glomerular filtration, whereas overexpression of AIFM1 protein rescued

glucose-induced disruption of mitochondrial respiration [156]. Thus, decreased AIFM1 protein level in ART-HLO could be a consequence of impaired mitochondrial function.

Pathway analysis

Differentially low abundance proteins after ART treatment were significantly enriched for neutrophil extracellular traps (NETs) formation and alcoholism pathway. Ample evidence from the literature has implicated various exogeneous and endogenous stimuli such as biochemical stimuli, calcium influx and the DAMPs as a trigger for NETs formation [191]. Additionally, a model was introduced whereby a lysosomal leakage triggers a cascade of events involving ROS production and ending in formation of NETs [191]. Differentially high abundant proteins in A+TB-HLO were enriched in NETs formation, ATP-dependent chromatin remodelling and necroptosis pathways. Finally, low abundant proteins in TGZ-HLO samples were enriched in necroptosis pathway.

Contrasting protein enrichment in NETs formation pathway was observed among ART-HLO and A+TB-HLO. Low abundant proteins were significantly enriched for NETs formation in ART-HLO whereas in A+TB-HLO high abundant proteins were significantly enriched for NETs formation. In contrast to A+TB-HLO, low abundant proteins in TGZ-HLO were significantly enriched for necroptosis pathway. For instance, NETs formation pathway may be targeted with small molecules as therapeutics in ART-HLO and A+TB-HLO groups to alleviate excessive ROS production and augment expression of proteins partaking in antioxidant activities, DNA repair mechanisms and modulation of immune response to prevent DILI. Studies have been successful at inhibiting the necroptosis pathway with Nec-1 molecule in different disease states [199]. Data presented in this work indicated that ART drives excessive ROS production, augments inflammation and immune response that exacerbates tissue injury. Strikingly, proteins involved in protection against oxidative stress and liver injury were increased in ART-HLO, A+TB-HLO and TGZ-HLO while those involved in protection against DNA damage and/repair were decreased in ART-HLO.

Overall, inflammation and oxidative stress were common pathways that were observed to be associated with tissue injury in all the groups. Another interesting observation was NETs formation was common between the ART-HLO and A+TB-HLO groups but absent in the TGZ-HLO group. Crucially, the formation NETs appear to be driven by

different protein signatures in each group. In ART-HLO, NETs formation was associated with low abundant proteins while in A+TB-HLO it was associated with high abundant proteins. Necroptosis was a common pathway that drives tissue injury between A+TB-HLO and TGZ-HLO. However, each treatment group drove tissue injury differently from the other. In A+TB-HLO, necroptosis was induced by high abundant proteins while in TGZ-HLO it was mainly by low abundant proteins. Therefore, therapeutics for targeting pathways associated with DILI in HLO would require to be tailored differently to mitigate drug induced tissue injury.

Chapter 9: Overall conclusion

Limitations & conclusions

The main limitation of the present study is that only one iPSC cell line which reflects genetic make-up of one patient was utilized. Another crucial limitation is that expression of identified DEPs was not validated using tools such as Western blot or RT-qPCR. Moreover, the HLOs were treated with IC_{50} concentrations of ART, A+TB and TGZ for 72 hours instead of using the biologically relevant Cmax values that are found in the blood, CSF, and target organ. Furthermore, HLO's were not infected with HIV/pseudo-HIV or *Mycobacterium tuberculosis* (Mtb) to explore the immunological response of these infections. Regarding protein-protein interaction, the algorithm for protein-protein interactions using molecular complex of detection (MCODE) clustering, which enables us to identify protein complexes functionality and physical connections was not applied.

In conclusion, in the present study, I developed and validated 3D multicellular human liver organoids (HLO) derived from iPSCs as a model for drug induced liver injury. I used proteomic approach with label-free MS analysis as a strategy to discover differentially expressed proteins in ART-HLO, A+TB-HLO, and TGZ-HLO groups compared with UN-HLO. Data revealed that differential expression of proteins were related to the immune system, mitochondrial dysfunction, ATP-dependent chromatin remodelling and necroptosis pathway, which are related to the development of drug induced liver injury.

Accordingly, these findings need to be fully investigated and validated in future studies.

Future works

Future studies are required to utilize two or more iPSCs cell line to get overall picture of the general population not individualized information. Also, HLOs need to be treated with Cmax of the experimental drugs instead of IC50 concentrations. For infections, live pathogen must be utilized. Future studies must explore the development of liver+ gut organoid to understand the intricate complexity of these two organs and how drugs generally get absorbed and metabolized and see the impact of those metabolites on the proteome of both systems.

References

1. Huch M, Gehart H, van Boxtel R, Hamer K, Blokzijl F, Verstegen MMA, et al. Long-Term Culture of Genome-Stable Bipotent Stem Cells from Adult Human Liver. Cell [Internet]. 2015 [cited 2019 Jun 5];160:299–312. Available from: https://www.sciencedirect.com/science/article/pii/S0092867414015669

2. Underhill GH, Khetani SR. Emerging trends in modeling human liver disease in vitro . APL Bioeng [Internet]. 2019 [cited 2020 Jul 10];3:040902. Available from: https://pubmed.ncbi.nlm.nih.gov/31893256/

3. Collins SD, Yuen G, Tu T, Budzinska MA, Spring K, Bryant K, et al. In Vitro Models of the Liver: Disease Modeling, Drug Discovery and Clinical Applications. Hepatocell Carcinoma [Internet]. Codon Publications; 2019 [cited 2020 Jul 10]. p. 47–67. Available from: https://pubmed.ncbi.nlm.nih.gov/31664801/

4. Zeilinger K, Freyer N, Damm G, Seehofer D, Knöspel F. Cell sources for *in vitro* human liver cell culture models. Exp Biol Med [Internet]. 2016 [cited 2019 Jun 5];241:1684–98. Available from: http://journals.sagepub.com/doi/10.1177/1535370216657448

5. Yokoyama Y, Sasaki Y, Terasaki N, Kawataki T, Takekawa K, Iwase Y, et al. Comparison of drug metabolism and its related hepatotoxic effects in HepaRG, cryopreserved human hepatocytes, and HepG2 cell cultures. Biol Pharm Bull. 2018;41:722–32.

6. Godoy P, Hewitt NJ, Albrecht U, Andersen ME, Ansari N, Bhattacharya S, et al. Recent advances in 2D and 3D in vitro systems using primary hepatocytes, alternative hepatocyte sources and non-parenchymal liver cells and their use in

investigating mechanisms of hepatotoxicity, cell signaling and ADME. Arch Toxicol [Internet]. 2013 [cited 2019 Jun 4];87:1315–530. Available from: http://link.springer.com/10.1007/s00204-013-1078-5

7. Pfeiffer E, Kegel V, Zeilinger K, Hengstler JG, Nüssler AK, Seehofer D, et al. Featured Article: Isolation, characterization, and cultivation of human hepatocytes and non-parenchymal liver cells. Exp Biol Med [Internet]. 2015 [cited 2019 Jun 5];240:645–56. Available from: http://journals.sagepub.com/doi/10.1177/1535370214558025

8. Broutier L, Andersson-Rolf A, Hindley CJ, Boj SF, Clevers H, Koo B-K, et al. 1. Broutier, L., Andersson-Rolf, A., Hindley, C. J., Boj, S. F., Clevers, H., Koo, B.K., & Huch, M. (2016). Culture and establishment of self-renewing human and mouse adult liver and pancreas 3D organoids and their genetic manipulation. Nature Protocols,. Nat Protoc [Internet]. 2016 [cited 2019 Jun 5];11:1724–43. Available from: http://www.nature.com/articles/nprot.2016.097

9. Siller R, Greenhough S, Naumovska E, Sullivan GJ. Small-Molecule-Driven Hepatocyte Differentiation of Human Pluripotent Stem Cells. Stem Cell Reports [Internet]. 2015 [cited 2019 Jun 18];4:939–52. Available from: https://www.sciencedirect.com/science/article/pii/S2213671115001010

10. Mun SJ, Ryu JS, Lee MO, Son YS, Oh SJ, Cho HS, et al. Generation of expandable human pluripotent stem cell-derived hepatocyte-like liver organoids. J Hepatol. 2019;71:970–85.

11. Ouchi R, Togo S, Kimura M, Shinozawa T, Koido M, Koike H, et al. Modeling Steatohepatitis in Humans with Pluripotent Stem Cell-Derived Organoids. Cell Metab [Internet]. 2019 [cited 2019 Sep 15];30:374-384.e6. Available from: https://www.sciencedirect.com/science/article/pii/S1550413119302475

12. Kruitwagen HS, Oosterhoff LA, Vernooij IGWH, Schrall IM, van Wolferen ME, Bannink F, et al. Long-Term Adult Feline Liver Organoid Cultures for Disease Modeling of Hepatic Steatosis. Stem Cell Reports [Internet]. 2017 [cited 2019 Jun 19];8:822–30. Available from: https://www.sciencedirect.com/science/article/pii/S2213671117300826

13. Takebe T, Sekine K, Enomura M, Koike H, Kimura M, Ogaeri T, et al. Vascularized and functional human liver from an iPSC-derived organ bud transplant. Nature [Internet]. 2013 [cited 2019 Jun 5];499:481–4. Available from: http://www.nature.com/articles/nature12271

14. Nie Y-Z, Zheng Y-W, Ogawa M, Miyagi E, Taniguchi H. Human liver organoids generated with single donor-derived multiple cells rescue mice from acute liver failure. Stem Cell Res Ther [Internet]. 2018 [cited 2019 Jun 5];9:5. Available from: https://stemcellres.biomedcentral.com/articles/10.1186/s13287-017-0749-1

15. Takebe T, Sekine K, Kimura M, Yoshizawa E, Ayano S, Koido M, et al. Massive and Reproducible Production of Liver Buds Entirely from Human Pluripotent Stem Cells. Cell Rep [Internet]. 2017 [cited 2019 Jun 19];21:2661–70. Available from: https://www.sciencedirect.com/science/article/pii/S221112471731625X

16. Coll M, Perea L, Boon R, Leite SB, Vallverdú J, Mannaerts I, et al. Generation of Hepatic Stellate Cells from Human Pluripotent Stem Cells Enables In Vitro Modeling of Liver Fibrosis. Cell Stem Cell. 2018;23:101-113.e7.

17. Atienzar FA, Blomme EA, Chen M, Hewitt P, Kenna JG, Labbe G, et al. Key Challenges and Opportunities Associated with the Use of In Vitro Models to Detect Human DILI: Integrated Risk Assessment and Mitigation Plans. Biomed Res Int [Internet]. 2016 [cited 2022 Feb 6];2016. Available from: https://pubmed.ncbi.nlm.nih.gov/27689095/

18. Mariotti V, Strazzabosco M, Fabris L, Calvisi DF. Animal models of biliary injury and altered bile acid metabolism. Biochim. Biophys. Acta - Mol. Basis Dis. Elsevier B.V.; 2018. p. 1254–61.

19. Mosedale M, Watkins PB. Drug-induced liver injury: Advances in mechanistic understanding that will inform risk management. Clin Pharmacol Ther. 2017;101:469–80.

20. Olson H, Betton G, Robinson D, Thomas K, Monro A, Kolaja G, et al. Concordance of the Toxicity of Pharmaceuticals in Humans and in Animals. Elsevier [Internet]. 2000 [cited 2020 Jun 9]; Available from: http://www.idealibrary.com

21. Andersen ME, Al-Zoughool M, Croteau M, Westphal M, Krewski D. The future of toxicity testing. J Toxicol Environ Heal - Part B Crit Rev [Internet]. 2010 [cited 2020 Mar 5];13:163–96. Available from: http://www.tandfonline.com/doi/abs/10.1080/10937404.2010.483933

22. Knobeloch D, Ehnert S, Schyschka L, Büchler P, Schoenberg M, Kleeff J, et al. Human hepatocytes: Isolation, culture, and quality procedures. Methods Mol Biol [Internet]. Humana Press; 2012 [cited 2019 Jun 19]. p. 99–120. Available from: http://link.springer.com/10.1007/978-1-61779-367-7_8

23. Schyschka L, Sánchez JJM, Wang Z, Burkhardt B, Müller-Vieira U, Zeilinger K, et al. Hepatic 3D cultures but not 2D cultures preserve specific transporter activity for acetaminophen-induced hepatotoxicity. Arch Toxicol [Internet]. 2013 [cited 2019 Jun 19];87:1581–93. Available from: http://link.springer.com/10.1007/s00204-013-1080-y

24. Nantasanti S, de Bruin A, Rothuizen J, Penning LC, Schotanus BA. Concise Review: Organoids Are a Powerful Tool for the Study of Liver Disease and Personalized Treatment Design in Humans and Animals. Stem Cells Transl Med [Internet]. 2016 [cited 2019 Jun 5];5:325–30. Available from: http://dx.doi.org/

25. Guo L, Dial S, Shi L, Branham W, Liu J, Fang JL, et al. Similarities and differences in the expression of drug-metabolizing enzymes between human hepatic cell lines and primary human hepatocytes. Drug Metab Dispos [Internet]. 2011 [cited 2019 Jun 4];39:528–38. Available from: http://dmd.aspetjournals.org/content/dmd/early/2010/12/13/dmd.110.035873.full .pdf

26. Gripon P, Rumin S, Urban S, Le Seyec J, Glaise D, Cannie I, et al. Infection of a human hepatoma cell line by hepatitis B virus. Proc Natl Acad Sci U S A [Internet]. 2002 [cited 2023 Feb 8];99:15655–60. Available from: www.pnas.orgcgidoi10.1073pnas.232137699

27. Andersson TB, Kanebratt KP, Kenna JG. The HepaRG cell line: a unique *in vitro* tool for understanding drug metabolism and toxicology in human. Expert Opin Drug Metab Toxicol [Internet]. 2012 [cited 2019 Jun 19];8:909–20. Available from: http://www.tandfonline.com/doi/full/10.1517/17425255.2012.685159

28. Guillouzo A, Corlu A, Aninat C, Glaise D, Morel F, Guguen-Guillouzo C. The human hepatoma HepaRG cells: A highly differentiated model for studies of liver metabolism and toxicity of xenobiotics. Chem Biol Interact [Internet]. 2007 [cited 2019 Jun 4];168:66–73. Available from: https://www.sciencedirect.com/science/article/pii/S0009279706003553

29. Koui Y, Kido T, Ito T, Oyama H, Chen SW, Katou Y, et al. An In Vitro Human Liver Model by iPSC-Derived Parenchymal and Non-parenchymal Cells. Stem Cell Reports. 2017;9:490–8.

30. Rashid ST, Corbineau S, Hannan N, Marciniak SJ, Miranda E, Alexander G, et al. Modeling inherited metabolic disorders of the liver using human induced pluripotent stem cells. J Clin Invest [Internet]. 2010 [cited 2019 Jun 4];120:3127–36. Available from: http://www.ncbi.nlm.nih.gov/pubmed/20739751

31. Sampaziotis F, Cardoso de Brito M, Madrigal P, Bertero A, Saeb-Parsy K, Soares FAC, et al. Cholangiocytes derived from human induced pluripotent stem cells for disease modeling and drug validation. Nat Biotechnol [Internet]. 2015 [cited 2019 Jun 19];33:845–52. Available from: http://www.nature.com/articles/nbt.3275

32. Goldring C, Antoine DJ, Bonner F, Crozier J, Denning C, Fontana RJ, et al. Stem cell–derived models to improve mechanistic understanding and prediction of human drug-induced liver injury. Hepatology [Internet]. 2017 [cited 2019 Jun 4];65:710–21. Available from: www.liverpool.ac.uk/drug-safety/

33. Si-Tayeb K, Noto FK, Nagaoka M, Li J, Battle MA, Duris C, et al. Highly efficient generation of human hepatocyte-like cells from induced pluripotent stem cells. Hepatology [Internet]. 2010 [cited 2019 Jun 4];51:297–305. Available from: http://doi.wiley.com/10.1002/hep.23354

34. Schwartz RE, Fleming HE, Khetani SR, Bhatia SN. Pluripotent stem cellderived hepatocyte-like cells. Biotechnol Adv [Internet]. 2014 [cited 2019 Jun 4];32:504–13. Available from: https://www.sciencedirect.com/science/article/pii/S0734975014000056

35. Davidson MD, Ware BR, Khetani SR. Stem cell-derived liver cells for drug testing and disease modeling. Discov Med. 2015;19:349–58.

36. Fu GB, Huang WJ, Zeng M, Zhou X, Wu HP, Liu CC, et al. Expansion and differentiation of human hepatocyte-derived liver progenitor-like cells and their use for the study of hepatotropic pathogens. Cell Res. 2019;29:8–22.

37. Touboul T, Hannan NRF, Corbineau S, Martinez A, Martinet C, Branchereau S, et al. Generation of functional hepatocytes from human embryonic stem cells under chemically defined conditions that recapitulate liver development. Hepatology [Internet]. 2010 [cited 2019 Jun 19];51:1754–65. Available from: http://doi.wiley.com/10.1002/hep.23506

38. Hannan NRF, Segeritz C-P, Touboul T, Vallier L. Production of hepatocytelike cells from human pluripotent stem cells. Nat Protoc [Internet]. 2013 [cited 2019 Jun 4];8:430–7. Available from: http://www.nature.com/articles/nprot.2012.153

39. Song Z, Cai J, Liu Y, Zhao D, Yong J, Duo S, et al. Efficient generation of hepatocyte-like cells from human induced pluripotent stem cells. Cell Res [Internet]. 2009 [cited 2019 Jun 4];19:1233–42. Available from: http://www.nature.com/articles/cr2009107

40. Ang LT, Tan AKY, Autio MI, Goh SH, Choo SH, Lee KL, et al. A Roadmap for Human Liver Differentiation from Pluripotent Stem Cells. Cell Rep [Internet]. 2018 [cited 2019 Jun 19];22:2190–205. Available from: https://linkinghub.elsevier.com/retrieve/pii/S2211124718301517

41. Dianat N, Dubois-Pot-Schneider H, Steichen C, Desterke C, Leclerc P, Raveux A, et al. Generation of functional cholangiocyte-like cells from human pluripotent stem cells and HepaRG cells. Hepatology [Internet]. 2014 [cited 2019 Jun 4];60:700–14. Available from: http://doi.wiley.com/10.1002/hep.27165

42. Ogawa M, Ogawa S, Bear CE, Ahmadi S, Chin S, Li B, et al. Directed differentiation of cholangiocytes from human pluripotent stem cells. Nat Biotechnol [Internet]. 2015 [cited 2019 Jun 4];33:853–61. Available from: http://www.nature.com/articles/nbt.3294

43. Lam DTUH, Dan YY, Chan YS, Ng HH. Emerging liver organoid platforms and technologies. Cell Regen (London, England) [Internet]. 2021 [cited 2022 Feb 10];10. Available from: https://pubmed.ncbi.nlm.nih.gov/34341842/

44. Mederacke I, Hsu CC, Troeger JS, Huebener P, Mu X, Dapito DH, et al. Fate tracing reveals hepatic stellate cells as dominant contributors to liver fibrosis independent of its aetiology. Nat Commun. 2013;4.

45. Poisson J, Lemoinne S, Boulanger C, Durand F, Moreau R, Valla D, et al. Liver sinusoidal endothelial cells: Physiology and role in liver diseases. J. Hepatol. Elsevier B.V.; 2017. p. 212–27.

46. Tasnim F, Xing J, Huang X, Mo S, Wei X, Tan M-H, et al. Generation of mature kupffer cells from human induced plur1. Tasnim, F., Xing, J., Huang, X., Mo, S., Wei, X., Tan, M.-H., & Yu, H. (2019). Generation of mature kupffer cells from human induced pluripotent stem cells. Biomaterials, 192, 377–391. doi:10.10. Biomaterials [Internet]. 2019 [cited 2019 Jun 5];192:377–91. Available from: https://www.sciencedirect.com/science/article/pii/S0142961218307932

47. Wilgenburg B van, Browne C, Vowles J, Cowley SA. Efficient, Long Term Production of Monocyte-Derived Macrophages from Human Pluripotent Stem Cells under Partly-Defined and Fully-Defined Conditions. Covas DT, editor. PLoS One [Internet]. 2013 [cited 2019 Jun 19];8:e71098. Available from: https://dx.plos.org/10.1371/journal.pone.0071098

48. Knoblich JA, Lancaster MA. Organogenesis in a dish: Modeling development and disease using organoid technologies. Science (80-) [Internet]. 2014 [cited 2019 Jun 10];345. Available from: https://science.sciencemag.org/content/345/6194/1247125.short

49. Huch M, Dorrell C, Boj SF, van Es JH, Li VSW, van de Wetering M, et al. In vitro expansion of single Lgr5+ liver stem cells induced by Wnt-driven regeneration. Nature [Internet]. 2013 [cited 2019 Jun 4];494:247–50. Available from: http://www.nature.com/articles/nature11826

50. Garnier D, Li R, Delbos F, Fourrier A, Collet C, Guguen-Guillouzo C, et al. Expansion of human primary hepatocytes in vitro through their amplification as liver progenitors in a 3D organoid system. Sci Rep [Internet]. 2018 [cited 2019 Sep 15];8:8222. Available from: http://www.nature.com/articles/s41598-01826584-1

51. Zhang R-R, Koido M, Tadokoro T, Ouchi R, Matsuno T, Ueno Y, et al. Human iPSC-Derived Posterior Gut Progenitors Are Expandable and Capable of Forming Gut and Liver Organoids. Stem Cell Reports [Internet]. 2018 [cited 2019 Jun 19];10:780–93. Available from: https://www.sciencedirect.com/science/article/pii/S2213671118300328

52. Jong E, Conradie F, Berhanu R, Black A, John M-A, Meintjes G, et al. Consensus statement: Management of drug-induced liver injury in HIV-positive patients treated for TB. South Afr J HIV Med. 2013;14:113–9.

53. Grinsztejn B, Hosseinipour MC, Ribaudo HJ, Swindells S, Eron J, Chen YQ, et al. Effects of early versus delayed initiation of antiretroviral treatment on clinical outcomes of HIV-1 infection: Results from the phase 3 HPTN 052 randomised controlled trial. Lancet Infect Dis. 2014;14:281–90.

54. Esté JA, Telenti A. HIV entry inhibitors. Lancet (London, England) [Internet]. 2007 [cited 2022 Feb 7];370:81–8. Available from: https://pubmed.ncbi.nlm.nih.gov/17617275/

55. Lange JMA, Ananworanich J. The discovery and development of antiretroviral agents. Antivir Ther [Internet]. 2014 [cited 2022 Feb 7];19 Suppl 3:5–14. Available from: https://pubmed.ncbi.nlm.nih.gov/25310317/

56. Das K, Arnold E. HIV-1 reverse transcriptase and antiviral drug resistance. Part 1. Curr Opin Virol [Internet]. 2013 [cited 2022 Feb 7];3:111–8. Available from: https://pubmed.ncbi.nlm.nih.gov/23602471/

57. Meintjes G, Moorhouse MA, Carmona S, Davies N, Dlamini S, Van Vuuren C, et al. Adult antiretroviral therapy guidelines 2017. South Afr J HIV Med. 2017;18.

58. Goldgur Y, Craigie R, Cohen GH, Fujiwara T, Yoshinaga T, Fujishita T, et al. Structure of the HIV-1 integrase catalytic domain complexed with an inhibitor: a platform for antiviral drug design. Proc Natl Acad Sci U S A [Internet]. 1999 [cited

2022 Feb 7];96:13040–3. Available from: https://pubmed.ncbi.nlm.nih.gov/10557269/

59. Brik A, Wong CH. HIV-1 protease: mechanism and drug discovery. Org Biomol Chem [Internet]. 2003 [cited 2022 Feb 7];1:5–14. Available from: https://pubmed.ncbi.nlm.nih.gov/12929379/

60. Wensing AMJ, van Maarseveen NM, Nijhuis M. Fifteen years of HIV Protease Inhibitors: raising the barrier to resistance. Antiviral Res [Internet]. 2010 [cited 2022 Feb 7];85:59–74. Available from: https://pubmed.ncbi.nlm.nih.gov/19853627/

61. Núñez M. Clinical syndromes and consequences of antiretroviral-related hepatotoxicity. Hepatology [Internet]. 2010 [cited 2020 Jan 24];52:1143–55. Available from: http://doi.wiley.com/10.1002/hep.23716

62. Bica I, McGovern B, Dhar R, Stone D, McGowan K, Scheib R, et al. Increasing Mortality Due to End-Stage Liver Disease in Patients with Human Immunodeficiency Virus Infection. Clin Infect Dis [Internet]. 2001 [cited 2020 Jan 24];32:492–7. Available from: https://academic.oup.com/cid/articlelookup/doi/10.1086/318501

63. Bonacini M, Inductivo-Yu I. Highly Active Antiretroviral Therapy-Induced Liver Injury. Curr Drug Saf [Internet]. 2008 [cited 2020 Jan 24];3:4–13. Available from: https://www.ingentaconnect.com/content/ben/cds/2008/00000003/00000001/art00002

64. Sanne I, Mommeja-Marin H, Hinkle J, Bartlett JA, Lederman MM, Maartens G, et al. Severe Hepatotoxicity Associated with Nevirapine Use in HIV-Infected Subjects. J Infect Dis [Internet]. 2005 [cited 2020 Jan 31];191:825–9. Available from: https://academic.oup.com/jid/article-lookup/doi/10.1086/428093

65. Brück S, Witte S, Brust J, Schuster D, Mosthaf E, Procaccianti M, et al. Hepatotoxicity in patients prescribed efavirenz or Nevirapine [Internet]. Eur. J. Med. Res. 2008 [cited 2020 Jun 9]. p. 343–8. Available from: https://pubmed.ncbi.nlm.nih.gov/18700192/

66. Hoffmann CJ, Charalambous S, Thio CL, Martin DJ, Pemba L, Fielding KL, et al. Hepatotoxicity in an African antiretroviral therapy cohort: the effect of tuberculosis and hepatitis B. AIDS [Internet]. 2007 [cited 2020 Jan 31];21:1301– 8. Available from: https://insights.ovid.com/crossref?an=00002030-20070619000009

67. Sonderup MW, Maughan D, Gogela N, Setshedi M, Wainwright H, Meintjes G, et al. Identification of a novel and severe pattern of efavirenz drug-induced liver injury in South Africa. AIDS [Internet]. 2016 [cited 2020 Jan 31];30:1483–5. Available from: http://content.wkhealth.com/linkback/openurl?sid=WKPTLP:landingpage&an=00002030-201606010-00020

68. Ezhilarasan D, Srilekha M, Raghu R. HAART and hepatotoxicity. J Appl Pharm Sci [Internet]. 2017 [cited 2020 Jan 30];7:220–6. Available from: https://www.researchgate.net/publication/316911871

69. Willig JH, Echevarria J, Westfall AO, Iglesias D, Henostroza G, Seas C, et al. Durability of initial antiretroviral therapy in a resource-constrained setting and the potential need for zidovudine weight-based dosing. J Acquir Immune Defic Syndr [Internet]. 2010 [cited 2020 Jun 8];53:215–21. Available from: https://www.researchgate.net/publication/41149093

70. Sulkowski MS. Drug-Induced Liver Injury Associated with Antiretroviral Therapy that Includes HIV-1 Protease Inhibitors. Clin Infect Dis [Internet]. 2004 [cited 2020 Jun 9];38:S90–7. Available from: http://academic.oup.com/cid/article/38/Supplement_2/S90/331430/DrugInduced - Liver-Injury-Associated-with

71. Tseng Y-T, Yang C-J, Chang S-Y, Lin S-W, Tsai M-S, Liu W-C, et al. Incidence and risk factors of skin rashes and hepatotoxicity in HIV-infected patients receiving nevirapine-containing combination antiretroviral therapy in Taiwan. Int J Infect Dis [Internet]. 2014 [cited 2020 May 5];29:12–7. Available from: http://dx.doi.org/10.1016/j.ijid.2014.08.012

72. Coffie PA, Tonwe-Gold B, Tanon AK, Amani-Bosse C, Bédikou G, Abrams EJ, et al. Incidence and risk factors of severe adverse events with nevirapinebased

antiretroviral therapy in HIV-infected women. MTCT-Plus program, Abidjan, Côte d'Ivoire. BMC Infect Dis. 2010;10:p.188.

73. van Griensven J, Zachariah R, Rasschaert F, Mugabo J, Atté EF, Reid T. Stavudine- and nevirapine-related drug toxicity while on generic fixed-dose antiretroviral treatment: incidence, timing and risk factors in a three-year cohort in Kigali, Rwanda. Trans R Soc Trop Med Hyg [Internet]. 2010 [cited 2020 Jun 8];104:148–53. Available from: https://academic.oup.com/trstmh/articleabstract/104/2/148/1923514

74. van Griensven J, De Naeyer L, Uwera J, Asiimwe A, Gazille C, Reid T. Success with antiretroviral treatment for children in Kigali, Rwanda: Experience with health center/nurse-based care. BMC Pediatr. 2008;8.

75. Walker UA. Antiretroviral therapy-induced liver alterations. Curr Opin HIV AIDS [Internet]. 2007 [cited 2020 Jan 24];2:293–8. Available from: https://insights.ovid.com/crossref?an=01222929-200707000-00008

76. Hoofnagle JH, Björnsson ES. Drug-induced liver injury - Types and phenotypes. N Engl J Med. 2019;381:264–73.

77. Leise MD, Poterucha JJ, Talwalkar JA. Drug-induced liver injury. Mayo Clin. Proc. Elsevier Ltd; 2014. p. 95–106.

78. Roth RA, Ganey PE. Intrinsic versus idiosyncratic drug-induced hepatotoxicity - Two villains or one? J Pharmacol Exp Ther [Internet]. 2010 [cited 2020 Feb 21];332:692–7. Available from: http://jpet.aspetjournals.org/content/332/3/692.short

79. Maslak E, Gregorius A, Chlopicki S. Liver sinusoidal endothelial cells (LSECs) function and NAFLD; NO-based therapy targeted to the liver. Pharmacol Reports [Internet]. 2015 [cited 2020 Feb 18];67:689–94. Available from: http://dx.doi.org/10.1016/j.pharep.2015.04.010

80. Gulmez SE, Larrey D, Pageaux GP, Lignot S, Lassalle R, Jové J, et al. Transplantation for acute liver failure in patients exposed to NSAIDs or paracetamol (Acetaminophen): The multinational case-population SALT study.

Drug Saf. 2013;36:135–44.

81. Larson AM, Polson J, Fontana RJ, Davern TJ, Lalani E, Hynan LS, et al. Acetaminophen-induced acute liver failure: Results of a United States multicenter, prospective study. Hepatology [Internet]. 2005 [cited 2020 Feb 21];42:1364–72. Available from: http://doi.wiley.com/10.1002/hep.20948

82. Ganey PE, Luyendyk JP, Maddox JF, Roth RA. Adverse hepatic drug reactions: Inflammatory episodes as consequence and contributor. Chem Biol Interact. 2004;150:35–51.

83. Yaghi C, Honein K, Boujaoude J, Slim R, Moucari R, Sayegh R. Influence of acetaminophen at therapeutic doses on surrogate markers of severity of acute viral hepatitis. Gastroenterol Clin Biol. 2006;30:763–8.

84. Fontana RJ, Seeff LB, Andrade RJ, Björnsson E, Day CP, Serrano J, et al. Standardization of nomenclature and causality assessment in drug-induced liver injury: Summary of a clinical research workshop. Hepatology [Internet]. 2010 [cited 2022 Jun 19];52:730–42. Available from: https://onlinelibrary.wiley.com/doi/full/10.1002/hep.23696

85. Jong E, Conradie F, Berhanu R, Black A, John MA, Meintjes G, et al. Guideline: Consensus statement: Management of drug-induced liver injury in HIV-positive patients treated for TB. South Afr J HIV Med [Internet]. 2013 [cited 2022 Jun 19];14:113–9. Available from: https://journals.co.za/doi/abs/10.10520/EJC142382?casa_token=JyJVjCPMim4AAAAA:G4dHTEVG6Sgr52fcuATadDtOVMZoajIDVFcSRIyECuk6HC5nX5fEH3u0I8dKxraOOUdeU0HZimgRFI

86. Schutz C, Ismail Z, Proxenos CJ, Marais S, Burton R, Kenyon C, et al. Burden of antituberculosis and antiretroviral drug-induced liver injury at a secondary hospital in South Africa. South African Med J [Internet]. 2012 [cited 2022 Jun 19];102:506–11. Available from: https://journals.co.za/doi/abs/10.10520/EJC121284

87. Division of AIDS. DAIDS Adverse Event Grading Tables | DAIDS Regulatory Support Center (RSC) [Internet]. [cited 2022 Jun 19]. Available from:

https://rsc.niaid.nih.gov/clinical-research-sites/daids-adverse-event-gradingtables

88. Aithal GP, Watkins PB, Andrade RJ, Larrey D, Molokhia M, Takikawa H, et al. Case definition and phenotype standardization in drug-induced liver injury. Clin Pharmacol Ther. 2011;89:806–15.

89. Zanger UM, Schwab M. Cytochrome P450 enzymes in drug metabolism: Regulation of gene expression, enzyme activities, and impact of genetic variation. Pharmacol Ther [Internet]. 2013 [cited 2020 Jun 30];138:103–41. Available from: https://www.sciencedirect.com/science/article/pii/S0163725813000065

90. Kwara A, Lartey M, Sagoe KWC, Kenu E, Court MH. CYP2B6, CYP2A6 and UGT2B7 genetic polymorphisms are predictors of efavirenz mid-dose concentration in HIV-infected patients. AIDS [Internet]. 2009 [cited 2020 Jun 30];23:2101–6. Available from: https://www.ncbi.nlm.nih.gov/pmc/articles/PMC2875867/

91. Hofmann MH, Blievernicht JK, Klein K, Saussele T, Schaeffeler E, Schwab M, et al. Aberrant splicing caused by single nucleotide polymorphism c.516G>T [Q172H], a marker of CYP2B6*6, is responsible for decreased expression and activity of CYP2B6 in liver. J Pharmacol Exp Ther [Internet]. 2008 [cited 2020 Jun 30];325:284–92. Available from: https://www.researchgate.net/publication/5677706

92. Sinxadi PZ, Leger PD, McIlleron HM, Smith PJ, Dave JA, Levitt NS, et al. Pharmacogenetics of plasma efavirenz exposure in HIV-infected adults and children in South Africa. Br J Clin Pharmacol [Internet]. 2015 [cited 2020 Jun 30];80:146–56. Available from: http://doi.wiley.com/10.1111/bcp.12590

93. Queiroz MAF, Laurentino RV, da Silva Graça Amoras E, Araújo MSM de, Gomes STM, Lima SS, et al. The CYP2B6 G516T polymorphism influences CD4+ T-cell counts in HIV-positive patients receiving antiretroviral therapy in an ethnically diverse region of the Amazon. Int J Infect Dis. 2017;55:4–10.

94. Leger P, Dillingham R, Beauharnais CA, Kashuba ADM, Rezk NL, Fitzgerald DW, et al. CYP2B6 Variants and Plasma Efavirenz Concentrations during Antiretroviral Therapy in Port-au-Prince, Haiti . J Infect Dis [Internet]. 2009 [cited 2020 Jun 30];200:955–64. Available from: https://academic.oup.com/jid/articleabstract/200/6/955/856000

95. Gounden V, van Niekerk C, Snyman T, George JA. Presence of the CYP2B6 516G> T polymorphism, increased plasma Efavirenz concentrations and early neuropsychiatric side effects in South African HIV-infected patients. AIDS Res Ther. 2010;7.

96. Holzinger ER, Grady B, Ritchie MD, Ribaudo HJ, Acosta EP, Morse GD, et al. Genome-wide association study of plasma efavirenz pharmacokinetics in AIDS Clinical Trials Group protocols implicates several CYP2B6 variants. Pharmacogenet Genomics [Internet]. 2012 [cited 2020 Jun 30];22:858–67. Available from: https://www.ncbi.nlm.nih.gov/pmc/articles/PMC3614365/

97. Lu Y, Cederbaum AI. CYP2E1 and oxidative liver injury by alcohol. Free Radic Biol Med [Internet]. 2008 [cited 2020 Mar 9];44:723–38. Available from: https://www.sciencedirect.com/science/article/pii/S0891584907007770

98. Corsini A, Bortolini M. Drug-induced liver injury: The role of drug metabolism and transport. J. Clin. Pharmacol. 2013. p. 463–74.

99. Keppler D. Multidrug resistance proteins (MRPs, ABCCs): Importance for pathophysiology and drug therapy. Handb. Exp. Pharmacol. 2011. p. 299–323.

100. Li LM, Chen L, Deng GH, Tan WT, Dan YJ, Wang RQ, et al. SLCO1B1*15 haplotype is associated with rifampin-induced liver injury. Mol Med Rep. 2012;6:75–82.

101. Soriano V, Puoti M, Garcia-Gascó P, Rockstroh JK, Benhamou Y, Barreiro P, et al. Antiretroviral drugs and liver injury. AIDS [Internet]. 2008 [cited 2020 Jan 31];22:1–13. Available from: https://insights.ovid.com/crossref?an=00002030200801020-00001

102. Shehu AI, Ma X, Venkataramanan R. Mechanisms of Drug-Induced Hepatotoxicity. Clin. Liver Dis. W.B. Saunders; 2017. p. 35–54.

103. Tujios S FR. Mechanisms of drug-induced liver injury: from bedside to bench. Nat Rev Gastroenterol Hepatol [Internet]. 2011 [cited 2020 Feb 4];8:202. Available from: https://www.nature.com/nrgastro/journal/v8/n4/abs/nrgastro.2011.22.html

104. Blas-García A, Apostolova N, Ballesteros D, Monleón D, Morales JM, Rocha M, et al. Inhibition of mitochondrial function by efavirenz increases lipid content in hepatic cells. Hepatology. 2010;52:115–25.

105. Apostolova N, Gomez-Sucerquia LJ, Moran A, Alvarez A, Blas-Garcia A, Esplugues J V. Enhanced oxidative stress and increased mitochondrial mass during Efavirenz-induced apoptosis in human hepatic cells. Br J Pharmacol. 2010;160:2069–84.

106. Polo M, Alegre F, Funes HA, Blas-Garcia A, Victor VM, Esplugues J V, et al. Mitochondrial (dys)function - a factor underlying the variability of efavirenzinduced hepatotoxicity? Br J Pharmacol [Internet]. 2015 [cited 2020 Feb 6];172:1713–27. Available from: http://doi.wiley.com/10.1111/bph.13018

107. Apostolova N, Gomez-Sucerquia LJ, Alegre F, Funes HA, Victor VM, Barrachina MD, et al. ER stress in human hepatic cells treated with Efavirenz: Mitochondria again. J Hepatol. 2013;59:780–9.

108. Mounzer K, Hsu R, Fusco JS, Brunet L, Henegar CE, Vannappagari V, et al. HLA-B*57:01 screening and hypersensitivity reaction to abacavir between 1999 and 2016 in the OPERA® observational database: A cohort study. AIDS Res Ther [Internet]. 2019 [cited 2020 Jun 27];16:1. Available from: https://aidsrestherapy.biomedcentral.com/articles/10.1186/s12981-019-0217-3

109. Ma JD, Lee KC, Kuo GM. HLA-B*5701 testing to predict abacavir hypersensitivity. PLoS Curr [Internet]. 2010 [cited 2020 Jun 27];2. Available from: /pmc/articles/PMC3000684/?report=abstract

110. Cornejo Castro EM, Carr DF, Jorgensen AL, Alfirevic A, Pirmohamed M. HLA-allelotype associations with nevirapine-induced hypersensitivity reactions and hepatotoxicity: A systematic review of the literature and meta-analysis. Pharmacogenet Genomics [Internet]. 2015 [cited 2020 Feb 6];25:186–98.

Available from: https://journals.lww.com/jpharmacogenetics/fulltext/2015/04000/HLA_allelotype_associations_with.4.aspx

111. Hu K, Xiang Q, Wang Z, Mu GY, Zhang Z, Ma LY, et al. Associations between human leukocyte antigen polymorphisms and hypersensitivity to antiretroviral therapy in patients with human immunodeficiency virus: A meta-analysis. BMC Infect Dis [Internet]. 2019 [cited 2020 Jun 27];19:583. Available from: https://bmcinfectdis.biomedcentral.com/articles/10.1186/s12879-019-4227-5

112. Tangamornsuksan W, Lohitnavy O, Kongkaew C, Chaiyakunapruk N, Reisfeld B, Scholfield CN, et al. Association of HLA-B*5701 genotypes and abacavir-induced hypersensitivity reaction: A sysyematic review and metaanalysis. J Pharm Pharm Sci. 2015;18:68–76.

113. Rowley MW, Patel A, Zhou W, Wong M, Seetharam AB. Immune reconstitution syndrome with initiation of treatment of HBV/HIV co-infection: Activity flare associated with E antigen seroconversion. Ann Hepatol. 2019;18:220–4.

114. Matthews G V., Avihingsanon A, Lewin SR, Amin J, Rerknimitr R, Petcharapirat P, et al. A randomized trial of combination hepatitis B therapy in HIV/HBV coinfected antiretroviral naïve individuals in Thailand. Hepatology. 2008;48:1062–9.

115. Andrade BB, Hullsiek KH, Boulware DR, Rupert A, French MA, Ruxrungtham K, et al. Biomarkers of inflammation and coagulation are associated with mortality and hepatitis flares in persons coinfected with HIV and hepatitis viruses. J Infect Dis [Internet]. 2013 [cited 2020 Feb 7];207:1379–88. Available from: https://academic.oup.com/jid/article-abstract/207/9/1379/928087

116. Yang X, Meng Y, Han Z, Ye F, Wei L, Zong C. Mesenchymal stem cell therapy for liver disease: full of chances and challenges. Cell Biosci 2020 101 [Internet]. 2020 [cited 2022 Feb 10];10:1–18. Available from: https://cellandbioscience.biomedcentral.com/articles/10.1186/s13578-02000480-6

117. Tafazoli S, Mashregi M, O'Brien PJ. Role of hydrazine in isoniazid-induced hepatotoxicity in a hepatocyte inflammation model. Toxicol Appl Pharmacol. 2008;229:94–101.

118. Bumpus NN. Efavirenz and 8-hydroxyefavirenz induce cell death via a JNK- and BimEL-dependent mechanism in primary human hepatocytes. Toxicol Appl Pharmacol. 2011;257:227–34.

119. Spence JR, Mayhew CN, Rankin SA, Kuhar MF, Vallance JE, Tolle K, et al. Directed differentiation of human pluripotent stem cells into intestinal tissue in vitro. Nat 2010 4707332 [Internet]. 2010 [cited 2022 Feb 4];470:105–9. Available from: https://www.nature.com/articles/nature09691

120. Shinozawa T, Kimura M, Cai Y, Saiki N, Yoneyama Y, Ouchi R, et al. HighFidelity Drug-Induced Liver Injury Screen Using Human Pluripotent Stem CellDerived Organoids. Gastroenterology. 2021;160:831–46.

121. Wu F, Wu D, Ren Y, Huang Y, Feng B, Zhao N, et al. Generation of hepatobiliary organoids from human induced pluripotent stem cells. J Hepatol. 2019;70:1145–58.

122. Licá ICL, Frazão GCCG, Nogueira RA, Lira MGS, Dos Santos VAF, Rodrigues JGM, et al. Immunological mechanisms involved in macrophage activation and polarization in schistosomiasis. Parasitology [Internet]. 2023

[cited 2023 Aug 5];150:401–15. Available from: https://doi.org/10.1017/S0031182023000021

123. Schneeberger K, Sánchez-Romero N, Ye S, Van Steenbeek FG, Oosterhoff LA, Palacin IP, et al. Large-Scale Production of LGR5-Positive Bipotential
Human Liver Stem Cells. Hepatology [Internet]. 2020 [cited 2023 Nov 14];72.
Available from: https://aasldpubs.onlinelibrary.wiley.com/doi/10.1002/hep.31037

124. Pingitore P, Sasidharan K, Ekstrand M, Prill S, Lindén D, Romeo S, et al. Human Multilineage 3D Spheroids as a Model of Liver Steatosis and Fibrosis. Int J Mol Sci [Internet]. 2019 [cited 2019 Jun 4];20:1629. Available from: https://www.mdpi.com/1422-0067/20/7/1629

125. Maepa SW, Ndlovu H. Advances in generating liver cells from pluripotent stem cells as a tool for modeling liver diseases. Stem Cells [Internet]. 2020 [cited 2023 Feb 23];38:606–12. Available from: https://academic.oup.com/stmcls/article/38/5/606/6430504

126. Chen S, Li P, Wang Y, Yin Y, de Ruiter PE, Verstegen MMA, et al. Rotavirus infection and cytopathogenesis in human biliary organoids potentially recapitulate biliary atresia development. MBio [Internet]. 2020 [cited 2024 Apr 13];11:1–6. Available from: https://journals.asm.org/doi/10.1128/mbio.01968-20

127. Adikwu E, Oraebosi M, Biradee I. Selenium abrogates tenofovir/lamivudine/efavirenz-induced hepatotoxicity in rats. J Mar Med Soc. 2021;23:47.

128. Ronald LA, FitzGerald JM, Bartlett-Esquilant G, Schwartzman K, Benedetti A, Boivin JF, et al. Treatment with isoniazid or rifampin for latent tuberculosis infection: Population-based study of hepatotoxicity, completion and costs. Eur Respir J [Internet]. 2020 [cited 2024 Apr 13];55. Available from: https://doi.org/10.1183/13993003.02048-2019].

129. Jia R, Oda S, Tsuneyama K, Urano Y, Yokoi T. Establishment of a mouse model of troglitazone-induced liver injury and analysis of its hepatotoxic mechanism. J Appl Toxicol. 2019;39:1541–56.

130. Deckmyn O, Poynard T, Bedossa P, Paradis V, Peta V, Pais R, et al. Clinical Interest of Serum Alpha-2 Macroglobulin, Apolipoprotein A1, and Haptoglobin in Patients with Non-Alcoholic Fatty Liver Disease, with and without Type 2 Diabetes, before or during COVID-19. Biomedicines. 2022;10:1–37.

131. Atanasova E, Martinova F, Jelev D, Antonov K, de Mey C, Mateva L, et al. Alpha-2 Macroglobulin Is The Simplest Serum Biomarker For Liver Fibrosis And Fibrogenesis In Chronic Hepatitis C. J Med Dent Pract [Internet]. 2015 [cited 2024 Apr 13];2:153–64. Available from: https://www.academia.edu/download/70097379/Medinform-11-2015.pdf

132. Varma VR, Varma S, An Y, Hohman TJ, Seddighi S, Casanova R, et al. Alpha-

2 macroglobulin in Alzheimer's disease: A marker of neuronal injury through the RCAN1 pathway. Mol Psychiatry [Internet]. 2017 [cited 2024 Apr 13];22:13–23. Available from: /pmc/articles/PMC5726508/

133. Rehman AA, Ahsan H, Khan FH. Alpha-2-macroglobulin: A physiological guardian. J Cell Physiol [Internet]. 2013 [cited 2024 Apr 13];228:1665–75. Available from: https://onlinelibrary.wiley.com/doi/full/10.1002/jcp.24266

134. Tang Y, Yang S, Yao M, Yang M, Wei L, Chen H, et al. Hemoglobin induces inflammation through NF-kB signaling pathway and causes cell oxidative damage in grass carp (Ctenopharyngodon idella). Front Immunol. 2022;13:1–14.

135. Liu W, Baker SS, Baker RD, Nowak NJ, Zhu L. Upregulation of Hemoglobin Expression by Oxidative Stress in Hepatocytes and Its Implication in Nonalcoholic Steatohepatitis. PLoS One [Internet]. 2011 [cited 2024 Apr 13];6:24363. Available from: www.plosone.org

136. Shaver CM, Landstreet SR, Pugazenthi S, Scott F, Putz N, Ware LB, et al. The NLRP3 inflammasome in macrophages is stimulated by cell-free hemoglobin. Physiol Rep. 2020;8.

137. Gram M, Sveinsdottir S, Cinthio M, Sveinsdottir K, Hansson SR, Mörgelin M, et al. Extracellular hemoglobin - mediator of inflammation and cell death in the choroid plexus following preterm intraventricular hemorrhage. J Neuroinflammation. 2014;11:1–15.

138. Morgenstern R, Zhang J, Johansson K. Microsomal glutathione transferase 1: Mechanism and functional roles. Drug Metab Rev. 2011;43:300–6.

139. Johansson K, Järvliden J, Gogvadze V, Morgenstern R. Multiple roles of microsomal glutathione transferase 1 in cellular protection: A mechanistic study. Free Radic Biol Med [Internet]. 2010 [cited 2024 Apr 14];49:1638–45. Available from: https://www.sciencedirect.com/science/article/pii/S0891584910004818

140. Siritantikorn A, Johansson K, Åhlen K, Rinaldi R, Suthiphongchai T, Wilairat P, et al. Protection of cells from oxidative stress by microsomal glutathione transferase 1. Biochem Biophys Res Commun. 2007;355:592–6.

141. Johansson K, Åhlen K, Rinaldi R, Sahlander K, Siritantikorn A, Morgenstern R. Microsomal glutathione transferase 1 in anticancer drug resistance. Carcinogenesis [Internet]. 2007 [cited 2024 Apr 14];28:465–70. Available from: https://dx.doi.org/10.1093/carcin/bgl148

142. Lai AY, Wade PA. Cancer biology and NuRD: A multifaceted chromatin remodelling complex. Nat Rev Cancer [Internet]. 2011 [cited 2024 Apr 14];11:588–96. Available from: https://www.nature.com/articles/nrc3091

143. Li DQ, Kumar R. Mi-2/NuRD complex making inroads into DNA-damage response pathway. Cell Cycle [Internet]. 2010 [cited 2024 Apr 14];9:2071–9. Available from: https://www.tandfonline.com/action/journalInformation?journalCode=kccy20

144. Yarden RI, Brody LC. BRCA1 interacts with components of the histone deacetylase complex. Proc Natl Acad Sci U S A [Internet]. 1999 [cited 2024 Apr 14];96:4983–8. Available from: https://www.pnas.org/doi/abs/10.1073/pnas.96.9.4983

145. Aoyama Y, Naiki-Ito A, Xiaochen K, Komura M, Kato H, Nagayasu Y, et al. Lactoferrin prevents hepatic injury and fibrosis via the inhibition of NF-κB signaling in a rat non-alcoholic steatohepatitis model. Nutrients. 2022;14.

146. Baldi A, Pinotti L. Lipophilic microconstituents of milk. Adv Exp Med Biol [Internet]. 2008 [cited 2024 Apr 17];606:109–25. Available from: https://link.springer.com/content/pdf/10.1007/978-0-387-74087-4.pdf#page=173

147. Pu TY, Chuang KC, Tung MC, Yen CC, Chen YH, Cidem A, et al. Lactoferrin as a therapeutic agent for attenuating hepatic stellate cell activation in thioacetamide-induced liver fibrosis. Biomed Pharmacother [Internet]. 2024 [cited 2024 Apr 17];174. Available from: http://creativecommons.org/licenses/by-nc/4.0/

148. Guo C, Xue H, Guo T, Zhang W, Xuan WQ, Ren YT, et al. Recombinant human lactoferrin attenuates the progression of hepatosteatosis and hepatocellular death by regulating iron and lipid homeostasis in: Ob / ob mice. Food Funct. 2020;11:7183–96.

149. Castella S, Bernard R, Corno M, Fradin A, Larcher JC. Ilf3 and NF90 functions in RNA biology. Wiley Interdiscip Rev RNA [Internet]. 2015 [cited 2024 Apr 16];6:243–56. Available from: https://onlinelibrary.wiley.com/doi/full/10.1002/wrna.1270

150. Li K, Wu J lin, Qin B, Fan Z, Tang Q, Lu W, et al. ILF3 is a substrate of SPOP for regulating serine biosynthesis in colorectal cancer. Cell Res [Internet]. 2020;30:163–78. Available from: http://dx.doi.org/10.1038/s41422-019-0257-1

151. Shamanna RA, Hoque M, Lewis-Antes A, Azzam EI, Lagunoff D, Pe'ery T, et al. The NF90/NF45 Complex Participates in DNA Break Repair via Nonhomologous End Joining. Mol Cell Biol [Internet]. 2011 [cited 2024 Apr 16];31:4832–43. Available from: https://www.tandfonline.com/doi/abs/10.1128/MCB.05849-11

152. Liu LX, Deng W, Zhou XT, Chen RP, Xiang MQ, Guo YT, et al. The mechanism of adenosine-mediated activation of lncRNA MEG3 and its antitumor effects in human hepatoma cells. Int J Oncol. 2016;48:421–9.

153. Wang W, Xu R, He P, Xiong Y, Zhao H, Fu X, et al. Role of ATF3 triggering M2 macrophage polarization to protect against the inflammatory injury of sepsis through ILF3/NEAT1 axis. Mol Med [Internet]. 2024;30. Available from: https://doi.org/10.1186/s10020-023-00711-9

154. Zong L, Liang Z. Apoptosis-inducing factor: a mitochondrial protein associated with metabolic diseases—a narrative review. Cardiovasc Diagn Ther [Internet]. 2023 [cited 2024 Apr 14];13:609–22. Available from: /pmc/articles/PMC10315422/

155. Freyer N, Greuel S, Knöspel F, Gerstmann F, Storch L, Damm G, et al. Microscale 3D liver bioreactor for in vitro hepatotoxicity testing under perfusion conditions. Bioengineering. 2018;5:1–18.

156. Coughlan MT, Higgins GC, Nguyen TV, Penfold SA, Thallas-Bonke V, Tan SM, et al. Deficiency in apoptosis-inducing factor recapitulates chronic kidney disease via aberrant mitochondrial homeostasis. Diabetes. 2016;65:1085–98.

157. Tang H, Pang P, Qin Z, Zhao Z, Wu Q, Song S, et al. The CPNE Family and Their Role in Cancers. Front Genet. 2021;12:1–7.

158. Lin H, Zhang X, Liao L, Yu T, Li J, Pan H, et al. CPNE3 promotes migration and invasion in non-small cell lung cancer by interacting with RACK1 via FAK signaling activation. J Cancer. 2018;9:4215–22.

159. Chen Z, Jiang Z, Zhang W, He B. Silencing the expression of copine-iii enhances the sensitivity of hepatocellular carcinoma cells to the molecular targeted agent sorafenib. Cancer Manag Res. 2018;10:3057–67.

160. Zhang X, Han X, Zhang Y. CPNE3 interaction with RACK1 protects against myocardial ischemia/reperfusion injury. Exp Ther Med. 2021;23:1–10.

161. Mateyak MK, Kinzy TG. eEF1A: Thinking outside the ribosome. J Biol Chem [Internet]. 2010;285:21209–13. Available from: http://dx.doi.org/10.1074/jbc.R110.113795

162. Stoianov AM, Robson DL, Hetherington AM, Sawyez CG, Borradaile NM. Elongation factor 1A-1 is a mediator of hepatocyte lipotoxicity partly through its canonical function in protein synthesis. PLoS One. 2015;10:1–19.

163. Day AM, Brown JD, Taylor SR, Rand JD, Morgan BA, Veal EA. Inactivation of a Peroxiredoxin by Hydrogen Peroxide Is Critical for Thioredoxin-Mediated Repair of Oxidized Proteins and Cell Survival. Mol Cell [Internet]. 2012;45:398–408. Available from: http://dx.doi.org/10.1016/j.molcel.2011.11.027

164. Abbas W, Kumar A, Herbein G. The eEF1A proteins: At the crossroads of oncogenesis, apoptosis, and viral infections. Front Oncol. 2015;5:1–10.

165. Zhang T, Huang XH, Dong L, Hu D, Ge C, Zhan YQ, et al. PCBP-1 regulates alternative splicing of the CD44 gene and inhibits invasion in human hepatoma cell line HepG2 cells. Mol Cancer. 2010;9:1–10.

166. Ishii T, Igawa T, Hayakawa H, Fujita T, Sekiguchi M, Nakabeppu Y. PCBP1 and PCBP2 both bind heavily oxidized RNA but cause opposing outcomes, suppressing or increasing apoptosis under oxidative conditions. J Biol Chem. 2020;295:12247–61.

167. Zhang W, Shi H, Zhang M, Liu B, Mao S, Li L, et al. Poly C binding protein 1 represses autophagy through downregulation of LC3B to promote tumor cell apoptosis in starvation. Int J Biochem Cell Biol. 2016;73:127–36.

168. Ansa-Addo EA, Huang HC, Riesenberg B, Iamsawat S, Borucki D, Nelson MH, et al. RNA binding protein pcbp1 is an intracellular immune checkpoint for shaping t cell responses in cancer immunity. Sci Adv. 2020;6:1–16.

169. Fan N, Sun H, Wang Y, Zhang L, Xia Z, Peng L, et al. Midkine, a potential link between obesity and insulin resistance. PLoS One. 2014;9:1–10.

170. Masuda T, Maeda K, Sato W, Kosugi T, Sato Y, Kojima H, et al. Growth Factor Midkine Promotes T-Cell Activation through Nuclear Factor of Activated T Cells Signaling and Th1 Cell Differentiation in Lupus Nephritis. Am J Pathol [Internet]. 2017;187:740–51. Available from: http://dx.doi.org/10.1016/j.ajpath.2016.12.006

171. Lackner I, Weber B, Baur M, Haffner-Luntzer M, Eiseler T, Fois G, et al. Midkine is elevated after multiple trauma and acts directly on human cardiomyocytes by altering their functionality and metabolism. Front Immunol. 2019;10:1–13.

172. Kosugi T, Yuzawa Y, Sato W, Arata-Kawai H, Suzuki N, Kato N, et al. Midkine is involved in tubulointerstitial inflammation associated with diabetic nephropathy. Lab Investig [Internet]. 2007;87:903–13. Available from: http://dx.doi.org/10.1038/labinvest.3700599

173. Hobo A, Yuzawa Y, Kosugi T, Kato N, Asai N, Sato W, et al. The growth factor midkine regulates the renin-angiotensin system in mice. J Clin Invest. 2009;119:1616–25.

174. Liang H, Dong J, Cheng Z, Li Q, Feng D, Ling B. B-cell receptor-associated protein 31 promotes migration and invasion in ovarian cancer cells. Exp Ther Med. 2021;22:1–12.

175. D □, Inés Fernández-Ulibarri □ V, Vilella M, Lázaro-Diéguez F, Sarri E, Martínez SE, et al. Diacylglycerol Is Required for the Formation of COPI Vesicles in the Golgi-to-ER Transport Pathway. Mol Biol Cell. 2007;18:3250–63.

176. Stojanovic M, Germain M, Nguyen M, Shore GC. BAP31 and its caspase cleavage product regulate cell surface expression of tetraspanins and integrinmediated cell survival. J Biol Chem [Internet]. 2005;280:30018–24. Available from: http://dx.doi.org/10.1074/jbc.M501306200

177. Niu K, Xu J, Cao Y, Hou Y, Shan M, Wang Y, et al. BAP31 is involved in T cell activation through TCR signal pathways. Sci Rep. 2017;7:1–12.

178. Xu JL, Li LY, Wang YQ, Li YQ, Shan M, Sun SZ, et al. Hepatocyte-specific deletion of BAP31 promotes SREBP1C activation, promotes hepatic lipid accumulation, and worsens IR in mice. J Lipid Res [Internet]. 2018 [cited 2024 Apr 16];59:35–47. Available from: http://www.jlr.org

179. Wu Z, Yang F, Jiang S, Sun X, Xu J. Induction of liver steatosis in BAP31deficient mice burdened with tunicamycin-induced endoplasmic reticulum stress. Int J Mol Sci. 2018;19:1–16.

180. Zhao J, Lv X, Huo Y, Hu X, Li X, Sun S, et al. Hepatocyte-specific deficiency of bap31 amplified acetaminophen-induced hepatotoxicity via attenuating nrf2 signaling activation in mice. Int J Mol Sci. 2021;22.

181. Ćurčić IB, Kizivat T, Petrović A, Smolić R, Tabll A, Wu GY, et al. Therapeutic Perspectives of IL1 Family Members in Liver Diseases: An Update. J Clin Transl Hepatol [Internet]. 2022;10:1186–93. Available from: https://www.doi.org/10.14218/JCTH.2021.00501

182. Minnone G, De Benedetti F, Bracci-Laudiero L. NGF and its receptors in the regulation of inflammatory response. Int J Mol Sci. 2017;18.

183. Ciudad M, Ouandji S, Lamarthée B, Cladière C, Ghesquière T, Nivet M, et al. Regulatory T-cell dysfunctions are associated with increase in tumor necrosis factor α in autoimmune hemolytic anemia and participate in Th17 polarization. Haematologica. 2024;109:444–57.

184. Kalliolias GD, Ivashkiv LB. TNF biology, pathogenic mechanisms and emerging therapeutic strategies. Nat Rev Rheumatol [Internet]. 2016;12:49–62. Available from: https://doi.org/10.1038/nrrheum.2015.169

185. Wandrer F, Liebig S, Marhenke S, Vogel A, John K, Manns MP, et al. TNFReceptor-1 inhibition reduces liver steatosis, hepatocellular injury and fibrosis in NAFLD mice. Cell Death Dis. 2020;11:1–9.

186. Gieling RG, Wallace K, Han YP. Interleukin-1 participates in the progression from liver injury to fibrosis. Am J Physiol - Gastrointest Liver Physiol. 2009;296.

187. Kamari Y, Shaish A, Vax E, Shemesh S, Kandel-Kfir M, Arbel Y, et al. Lack of interleukin-1α or interleukin-1β inhibits transformation of steatosis to steatohepatitis and liver fibrosis in hypercholesterolemic mice. J Hepatol [Internet]. 2011;55:1086–94. Available from: http://dx.doi.org/10.1016/j.jhep.2011.01.048

188. Cho YE, Kim Y, Kim SJ, Lee H, Hwang S. Overexpression of Interleukin-8 Promotes the Progression of Fatty Liver to Nonalcoholic Steatohepatitis in Mice. Int J Mol Sci. 2023;24.

189. Zimmermann HW, Seidler S, Gassler N, Nattermann J, Luedde T, Trautwein C, et al. Interleukin-8 is activated in patients with chronic liver diseases and associated with hepatic macrophage accumulation in human liver fibrosis. PLoS One. 2011;6.

190. Boeltz S, Amini P, Anders HJ, Andrade F, Bilyy R, Chatfield S, et al. To NET or not to NET:current opinions and state of the science regarding the formation of neutrophil extracellular traps. Cell Death Differ. 2019;26:395–408.

191. Muñoz LE, Bilyy R, Biermann MHC, Kienhöfer D, Maueröder C, Hahn J, et al. Nanoparticles size-dependently initiate self-limiting NETosis-driven inflammation. Proc Natl Acad Sci U S A [Internet]. 2016 [cited 2024 Apr 19];113:E5856–65. Available from: https://www.pnas.org/doi/abs/10.1073/pnas.1602230113

192. Biermann MHC, Podolska MJ, Knopf J, Reinwald C, Weidner D, Maueröder C, et al. Oxidative burst-dependent NETosis is implicated in the resolution of necrosis-associated sterile inflammation. Front Immunol. 2016;7:1–13.

193. Reyes AA, Marcum RD, He Y. Structure and Function of Chromatin Remodelers. J Mol Biol [Internet]. 2021;433:166929. Available from: https://doi.org/10.1016/j.jmb.2021.166929

194. Clapier CR, Iwasa J, Cairns BR, Peterson CL. Mechanisms of action and regulation of ATP-dependent chromatin-remodelling complexes. Nat Rev Mol Cell Biol [Internet]. 2017 [cited 2024 Apr 19];18:407–22. Available from: https://www.nature.com/articles/nrm.2017.26

195. Sinha S, Verma S, Chaturvedi MM. Differential Expression of SWI/SNF Chromatin Remodeler Subunits Brahma and Brahma-Related Gene during DrugInduced Liver Injury and Regeneration in Mouse Model. DNA Cell Biol. 2016;35:373–84.

196. Molnár T, Mázló A, Tslaf V, Szöllősi AG, Emri G, Koncz G. Current translational potential and underlying molecular mechanisms of necroptosis. Cell Death Dis. 2019;10.

197. Takemoto K, Hatano E, Iwaisako K, Takeiri M, Noma N, Ohmae S, et al. Necrostatin-1 protects against reactive oxygen species (ROS)-induced hepatotoxicity in acetaminophen-induced acute liver failure. FEBS Open Bio [Internet]. 2014;4:777–87. Available from: http://dx.doi.org/10.1016/j.fob.2014.08.007

198. Dara L, Johnson H, Suda J, Win S, Gaarde W, Han D, et al. Receptor interacting protein kinase 1 mediates murine acetaminophen toxicity independent of the necrosome and not through necroptosis. Hepatology. 2015;62:1847–57.

199. Zhang YF, He W, Zhang C, Liu XJ, Lu Y, Wang H, et al. Role of receptor interacting protein (RIP)1 on apoptosis-inducing factor-mediated necroptosis during acetaminophen-evoked acute liver failure in mice. Toxicol Lett [Internet]. 2014;225:445–53. Available from: http://dx.doi.org/10.1016/j.toxlet.2014.01.005

200. Racanelli V, Rehermann B. The liver as an immunological organ. Hepatology. 2006;43.

201. Lee KK, Fujimoto K, Zhang C, Schwall CT, Alder NN, Pinkert CA, et al. Isoniazid-induced cell death is precipitated by underlying mitochondrial complex i dysfunction in mouse hepatocytes. Free Radic Biol Med [Internet]. 2013;65:584–94. Available from: http://dx.doi.org/10.1016/j.freeradbiomed.2013.07.038.

202. Segovia-Zafra A, Di Zeo-Sánchez DE, López-Gómez C, Pérez-Valdés Z, Garcia-Fuentes E, Andrade RJ, Lucena MI, Villanueva-Paz M. Preclinical models of idiosyncratic drug-induced liver injury (iDILI): Moving towards prediction. Acta Pharmaceutica Sinica B. 2021 Dec 1;11(12):3685-726.

203. Guo Z, Fan X, Nagy LE, Tomlinson S, Yuan G. New insights into the role of complement system in liver diseases. Frontiers in Immunology. 2023 Sep 8;14:1284944.

204. Thorgersen EB, Barratt-Due A, Haugaa H, Harboe M, Pischke SE, Nilsson PH, Mollnes TE. The role of complement in liver injury, regeneration, and transplantation. Hepatology. 2019 Aug;70(2):725-36.

205. Teirilä L, Heikkinen-Eloranta J, Kotimaa J, Meri S, Lokki AI. Regulation of the complement system and immunological tolerance in pregnancy. In Seminars in immunology 2019 Oct 1 (Vol. 45, p. 101337). Academic Press.

206. Juan CA, Pérez de la Lastra JM, Plou FJ, Pérez-Lebeña E. The chemistry of reactive oxygen species (ROS) revisited: outlining their role in biological macromolecules (DNA, lipids and proteins) and induced pathologies. International journal of molecular sciences. 2021 Apr 28;22(9):4642.

207. Tugasworo D, Prasetyo A, Kurnianto A, Retnaningsih R, Andhitara Y, Ardhini R, Budiman J. Malondialdehyde (MDA) and 8-hydroxy-2′-deoxyguanosine (8-OHdG) in ischemic stroke: a systematic review. The Egyptian Journal of Neurology, Psychiatry and Neurosurgery. 2023 Jun 30;59(1):87.

208. Akay C, Cooper M, Odeleye A, Jensen BK, White MG, Vassoler F, Gannon PJ, Mankowski J, Dorsey JL, Buch AM, Cross SA. Antiretroviral drugs induce oxidative

stress and neuronal damage in the central nervous system. Journal of neurovirology. 2014 Feb;20:39-53.

209. Singh S, Singh TG. Role of nuclear factor kappa B (NF-κB) signalling in neurodegenerative diseases: an mechanistic approach. Current Neuropharmacology. 2020 Sep 1;18(10):918-35.

210. Luedde T, Schwabe RF. NF-κB in the liver—linking injury, fibrosis and hepatocellular carcinoma. Nature reviews Gastroenterology & hepatology. 2011 Feb;8(2):108-18.

211. Zhuang X, Li L, Liu T, Zhang R, Yang P, Wang X, Dai L. Mechanisms of isoniazid and rifampicin-induced liver injury and the effects of natural medicinal ingredients: A review. Frontiers in Pharmacology. 2022 Oct 10;13:1037814.

Appendix

Table S1: Liquid Chromatography Mass Spectrometry (LC-MS) identified proteins in multicellular 3D human liver organoids (HLO).

Table S1_Identified and quantified prot

Data sheet 1: List of differentially expressed proteins among treatment groups.

Data sheet 1_Differentially expr

Data sheet 2: ANOVA significant proteins post B-H multiple sampling correction test.

Data sheet 2_ANOVA significan

Data sheet 3: Functional GO enrichment and pathway analysis in ART-HLO.

Data sheet 3_Functional GO en

Data sheet 4: Functional GO enrichment and pathway analysis in A+TB-HLO.

Data sheet
4_Functional GO en

Data sheet 5: Functional GO enrichment and pathway analysis in TGZ-HLO.

Data sheet
5_Functional Go en